TUNNELING IN STRONGLY CORRELATED MATERIALS

BY MARIANNA MALTSEVA

A dissertation submitted to the

Graduate School—New Brunswick

Rutgers, The State University of New Jersey

in partial fulfillment of the requirements

for the degree of

Doctor of Philosophy

Graduate Program in Physics and Astronomy

Written under the direction of

Piers Coleman

and approved by

New Brunswick, New Jersey

October, 2009

ABSTRACT OF THE DISSERTATION

Tunneling in strongly correlated materials

by Marianna Maltseva

Dissertation Director: Piers Coleman

Tunneling studies of strongly correlated materials provide information about the nature of electronic correlations, which is vital for investigation of emergent materials at the microscopic level. In particular, scanning tunneling spectroscopy/microscopy (STS/STM) studies have made major contributions to understanding cuprate superconductors (66), yet there is a sense that huge STM data arrays contain much more precious information to be extracted and analyzed. One of the most pressing questions in the field is how to improve the data analysis, so as to extract more information from STM data. A dominant trend in STM data analysis has been to interpret the data within a particular microscopic model, while using only basic data analysis tools. To decrease the reliance of the STM data interpretation on particular microscopic models, further advances in data analysis methods are necessary.

In Chapter 2 of this Thesis, we discuss how one can extract information about the phase of the order parameter from STM data. We show that symmetrized and anti-symmetrized correlators of local density of states give rise to observable coherence factor effects. In Chapter 3, we apply this framework to analyze the recent scanning tunneling experiments on an underdoped cuprate superconductor $Ca_{2-x}Na_xCuO_2Cl_2$ by T. Hanaguri et al. (60). In Chapter 4, we propose a model for nodal quasiparticle scattering in a disordered vortex lattice.

Recently, scanning tunneling studies of a Kondo lattice material URu_2Si_2 became possible (117). If it proves possible to apply scanning tunneling spectroscopy to Kondo lattice materials, then remarkable new opportunities in the ongoing investigation may emerge.

In Chapter 5, we examine the effect of co-tunneling to develop a theory of tunneling into a Kondo lattice. We find that the interference between the direct tunneling and the co-tunneling

channels leads to a novel asymmetric lineshape, which has two peaks and a gap. The presence of the peaks suggests that the interference is more dramatic in the case of Kondo lattice than in the single impurity case, because of the coherence. These features should be observed in future tunneling experiments on Kondo lattice materials.

Acknowledgements

It has been a great honor and pleasure to research strongly correlated materials at Rutgers. I would like to thank all the members of the Department of Physics and Astronomy for creating an especially friendly and inspiring research environment.

I would like to thank my advisor Piers Coleman for his guidance of my research, for his generous help and encouragement. I would like to thank Lev Ioffe, Haruo Kojima, Willem Kloet and Abhay Pasupathy for serving as members of my Ph. D. committee. I would like to thank Ron Ransome for his support as a graduate director. I would like to thank Jolie Cizewski, Noemie Koller and Torgny Gustafsson for being so generous with their time and advice.

I am indebted to our collaborators, Hidenori Takagi, Tetsuo Hanaguri and Yuhki Kohsaka, for kindly sharing the experimental data and for many illuminating discussions.

I am most grateful to the current and past members of the Rutgers condensed matter group, for being so generous with their time and support, and for providing many helpful discussions (in alphabetical order): Elihu Abrahams, Adriano Amaricci, Eva Andrei, Natan Andrei, Kasturi Basu, Ilya Berdnikov, Girsh Blumberg, Claudia Bungaro, Alberto Camjayi, Premi Chandra, Sungpo Chao, Sang-Wook Cheong, Marcello Civelli, Sinisa Coh, Valentino Cooper, Oswaldo Dieguez, Maxim Dzero, Carl-Johan Eklund, Craig Fennie, Lara Faoro, Rebecca Flint, Matthew Foster, Misha Gershenson, Rafael Greenblatt, Masud Haque, John Hopkinson, Don Hamann, Kristjan Haule, Lev Ioffe, Deepak Iyer, Andres Jerez, Karen Johnston, Jaewook Joo, Valery Kiryukhin, Gabriel Kotliar, David Langreth, Joel Lebowitz, Lorenzo de Leo, Guohong Li, Senia Katalinic, Eran Lebanon, Elena Loginova, Adina Luican, Andrei Malashevich, Pankaj Mehta, Marcus Mueller, Serge Nakhmanson, Andriy Nevidomskyy, Haile Owusu, Lucia Palova, Sergey Pankov, Hyowon Park, Indranil Paul, Maria E. Pezzoli, Vitaly Podzorov, Karin Rabe, Jerome Rech, Anindya Roy, Nayana Shah, Alexey Soluyanov, Ping Sun, Antonina Toropova, Levan Tskipuri, Ruslan Usmanov, David Vanderbilt, Kshitij Wagh, Xinjie Wang, Cedric Weber, Weida Wu, Xifan Wu, Chuck Yee, Emil Yuzbashyan, Alexey Zayak, Chenglin Zhang, and many others.

I would like to thank physicists outside Rutgers, for generously sharing their ideas and for providing many useful discussions (in alphabetical order): Megan Aronson, Sasha Balatsky, Leon Balents, Cristian Batista, Erez Berg, Greg Boyd, Collin Broholm, Paul Canfield, Cigdem

Capan, Sudip Chakravarty, Andrey Chubukov, J. C. Seamus Davis, Zachary Fisk, Ian Fisher, Eduardo Fradkin, Marcel Franz, Pouyan Ghaemi, Elena Hassinger, Peter Hirschfeld, Jennifer Hoffman, Eric Hudson, Steven Kivelson, Wingho Ko, Patrick Lee, Igor Mazin, Kyle McElroy, Ashot Melikyan, Andrew Millis, Vivek Mishra, Dirk Morr, Michael Norman, N. Phuan Ong, Shuheng Pan, Catherine Pepin, Tami Pereg-Barnea, Philip Phillips, David Pines, Ying Ran, Mohit Randeria, Achim Rosch, Subir Sachdev, Saeed Saremi, Douglas Scalapino, Joerg Schmalian, Andrew Schmidt, Suchitra Sebastian, Todadri Senthil, Qimiao Si, Joerg Sichelschmidt, Frank Steglich, Louis Taillefer, Zlatko Tesanovic, Oscar Vafek, Ilya Vekhter, Ashvin Vishwanath, Matthias Vojta, Thomas Vojta, Fa Wang, Cenke Xu, Ali Yazdani, Jian-Xin Zhu, and many others.

Outside of the condensed matter group, I would like to thank all my fellow graduate students and friends for their generous support (in alphabetical order): Evgeny Andriyash, Eleonora Dell'Aquila, Sujay Ashok, Dmitri Belov, Benjamin Doyon, Rouven Essig, Ross Fadely, Gareth Hughes, Sam Klevtsov, Dmitri Melnikov, Naseem Rangwala, Ricardo Sanchez, Neelima Sehgal, Gonzalo Torroba, and many others.

I would like to acknowledge the support of the National Science Foundation grant DMR-0605935.

Finally, I would like to thank all my family members for their support and love, and for being an inspiration.

Dedication

To my family

Table of Contents

List of Tables

List of Figures

Chapter 1
Introduction

1.1 Tunneling as a probe of highly correlated electron states.

Nature continues to amaze us, as new materials with emergent macroscopic properties are discovered. The origins of these new emergent properties often lie in the particular microscopic electronic correlations. Successful investigation of the electronic correlations in the emergent materials often requires sensitive experimental probes. In particular, since its invention in late 1950s, the ever-evolving technique of tunneling spectroscopy has propelled our understanding of electronic correlations in solids, as origins of the emergent macroscopic properties of the materials.

In this Introduction, we review applications of tunneling spectroscopy to studies of strongly correlated electron systems, from its early application as a probe of BCS superconductors to its modern applications to studies of copper oxide superconductors and Kondo lattice systems.

1.2 Tunneling experiments on BCS superconductors

In this section we discuss the birth of tunneling spectroscopy and the key role it played in verifying the microscopic BCS theory of superconductivity.

1.2.1 BCS superconductors

Superconductivity was discovered in 1911, as Heike Kamerlingh Onnes (1) observed loss of resistivity in mercury at a critical temperature $T_c = 4.2$ K, as shown in Figure 1.1(a). Soon the same phenomenon was detected in several other elemental metals, such as aluminum and tin, with superconducting transition temperatures T_c ranging up to 7.2 K in lead. In 1933 Walther Meissner and Robert Ochsenfeld (2) cooled tin and lead samples in an external magnetic field to find that below the superconducting transition temperature T_c, the samples cancelled all magnetic field inside, effectively becoming perfect diamagnets, as illustrated in Figure 1.1(b). Below the superconducting transition temperature T_c, superconductors are characterized by the

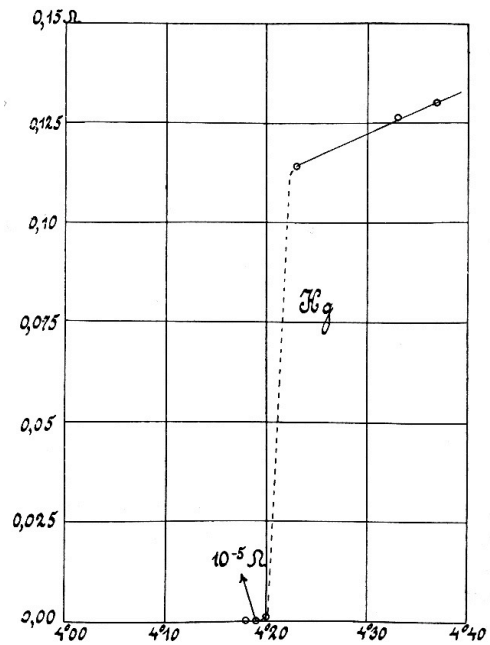

(a)

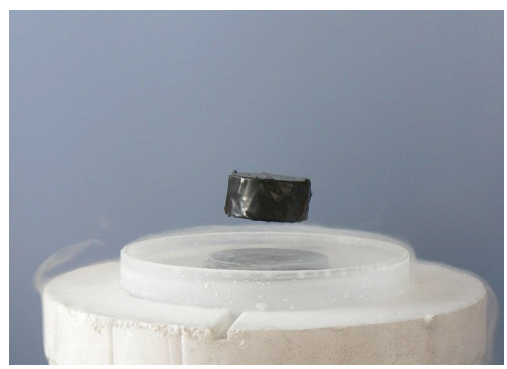

(b)

Figure 1.1: Basic properties of superconductors. Figure (a) displays resistivity loss at $T_c = 4.2$ K observed in mercury by K. Onnes in 1911 (1). Figure (b) displays the Meissner effect demonstration. Here a magnet is levitating above a high-temperature superconductor, cooled with liquid nitrogen. Persistent electric current flows on the surface of the superconductor, acting to exclude the magnetic field of the magnet. This current effectively forms an electromagnet that repels the magnet. Source: wikipedia.

following two macroscopic properties:

- loss of electrical resistance,
- the Meissner-Ochsenfeld effect (2), active expulsion of a magnetic flux from the sample as it is cooled thorough T_c.

The phenomenon of superconductivity would take 46 years since its discovery to be understood at the microscopic level, when John Bardeen, Leon Cooper and Robert Schrieffer advanced BCS theory (11) in 1957.

BCS theory did not appear in a vacuum. It was preceded by two decades of active phenomenological development of the theory of superconductivity (77). In 1935 Fritz and Heinz London (3) proposed that the electrodynamic properties of a superconductor could be described by the following "acceleration" equation:

$$\mathbf{J}_s = -\frac{n_s e^2}{m}\mathbf{A},$$

where $\mathbf{J}_s$ is the current density, $\mathbf{A}$ is the vector potential of the electromagnetic field, n_s the density of superconducting electrons with charge e and mass m. Londons' equation accounts for the Meissner effect. In 1935 Fritz London (4) proposed that the perfect diamagnetism was a consequence of a rigidity of the many-body wavefunction. He even suggested that this rigidity might derive from a gap in the excitation spectrum (10).

In 1950 Vitaly Ginzburg and Lev Landau (7) introduced $\Psi = |\Psi|e^{i\phi}$, a phenomenological order parameter to describe superconducting electrons, as an order parameter of the superconducting transition. London's rigidity hypothesis could now be linked to a "phase rigidity" of the order parameter, the microscopic nature of Ψ was still unclear.

A non-local modification of the London theory was later introduced by Pippard (5; 6), who suggested that the superconducting wavefunction had a characteristic lengthscale, the "coherence" length ξ_0, given by:

$$\xi_0 = a\frac{\hbar v_F}{kT_c}, \tag{1.1}$$

where a is an empirical constant. In 1955 Bardeen (9) showed that Pippard's version of the electrodynamics naturally followed from an energy gap model, so that the origin of the phase rigidity of the order parameter was the superconducting gap.

Finally, in 1957 BCS theory established the microscopic origin of the gap, $\Delta \sim \Psi$, as the order parameter. According to BCS theory, superconductivity is associated with condensation of electrons in Cooper pairs and is characterized by the formation of a complex order parameter

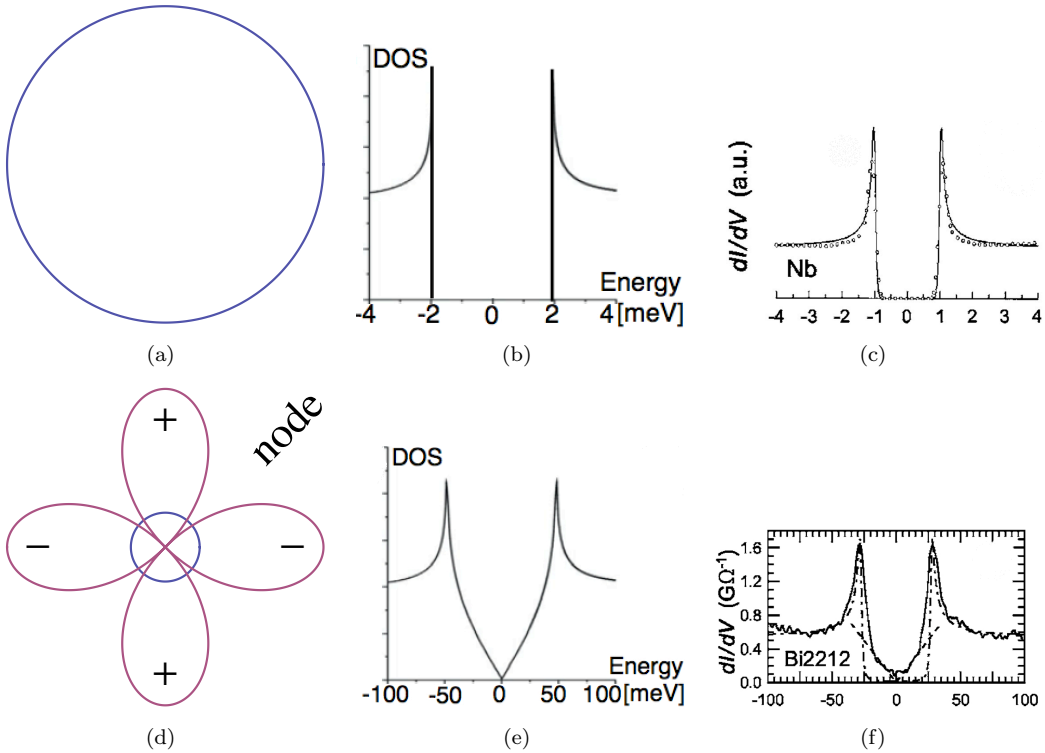

Figure 1.2: Comparison of s- and d-wave BCS superconductivity. (a)-(c): Isotropic s-wave superconductor. (a): Isotropic s-wave wavefunction of a Cooper pair, which leads to a fully gapped Fermi surface. (b): Tunneling density of states $\rho(V)$ in an s-wave BCS superconductor. (c): Spectrum of $dI/dV(V)$, experimental data obtained with STM in an s-wave BCS superconductor Nb (circles), BCS fit with $\Delta = 1.0$ meV, after (28; 66). (d)-(f): A superconductor with $d_{x^2-y^2}$ order parameter symmetry. (d): A $d_{x^2-y^2}$ wavefunction of a Cooper pair (shown in red) leads to a partially gapped Fermi surface (shown in blue). The gap vanishes in the nodal directions. (e): Tunneling density of states $\rho(V)$ in $d_x^2 - y^2$ superconductor. (f): An experimental STM spectrum of $dI/dV(V)$ obtained in an optimally doped high-temperature copper oxide superconductor Bi-2212 ($T_c = 92$ K) at 4.8 K (solid line), BCS s-wave fit with $\Delta = 27.5$ meV (dot-dashed line), and d-wave BCS fit (dashed line), after (26; 66).

with sample-wide phase coherence, $\Delta = \langle \psi_{\mathbf{k}\uparrow} \psi_{-\mathbf{k}\downarrow} \rangle$, where $\psi^\dagger_{\mathbf{k}\uparrow}$ is the creation operator for a single electron with momentum $\mathbf{k}$ and spin $\uparrow$. The condensation of electrons in Cooper pairs leads to a gap at the Fermi surface in the single particle excitation spectrum. The attractive interaction necessary for Cooper pairing is provided by the coupling to the crystal lattice through the phonon exchange mechanism.

BCS theory predicts that in an isotropic, s-wave superconductor, the electronic density of states has a gap at the Fermi energy. Just above the gap, the electronic density of states exhibits a square root singularity, a dramatic upturn due to electronic states piled up just above the

gap, predicted by the microscopic BCS theory, shown in Figure 1.2(b):

$$\rho_{BCS}(E) = \{ \begin{array}{c} \rho_F \frac{E}{\sqrt{E^2-\Delta^2}}, \ |E| > \Delta, \\ 0, \ |E| < \Delta, \end{array} \tag{1.2}$$

where ρ_F is the density of states of the metal in the normal state at the Fermi energy.

The microscopic BCS theory has predicted certain phenomena, such as coherence factor effects (13; 14; 15), which could not have been envisioned in the absence of the microscopic theory. Coherence factor effects include anomalous temperature dependencies of the quasiparticle scattering rates, observed with various experimental techniques, such as nuclear magnetic resonance (13), acoustic attenuation (14) and infrared absorption (15).

Nowadays, high-temperature superconductivity presents some of the greatest mysteries in condensed matter physics. In particular, the microscopic origin of the "pairing mechanism" in high temperature copper oxide superconductors and the nature of their unusual normal state remain unknown (32).

A parallel can be drawn between the 1950s and the present day. By all counts, research in high-temperature superconductivity is in an intermediate stage. While much experimental data have been collected already, and the phenomenological understanding is partially developed, a microscopic theory for the mechanism of high temperature superconductivity and the nature of the unusual normal state from which it is formed is absent.

The goal of this Thesis is largely phenomenological: namely, to provide interpretation of experiments, using theory in a phenomenological capacity, to spur the development of a microscopic theory of high-temperature superconductivity. Understanding of the high-temperature superconductivity at the microscopic level will provide insights into methods to search for higher temperature superconductors.

1.2.2 Tunneling in BCS superconductors

Some of the most direct microscopic confirmations of BCS theory derives from tunneling. In particular, quasiparticle tunneling in a superconductor-insulator-normal metal (SIN) junction, pioneered by Ivar Giaever (17), was used to determine the gap and the detailed form of the tunneling density of states.

Tunneling is a purely quantum-mechanical process in which a particle can pass from one clasically allowed region to another, through classically forbidden regions where the potential energy exceeds the kinetic energy of the particle, as schematically shown in Figure 1.3. Using semi-classical WKB approximation, one can show that the tunneling probability decreases

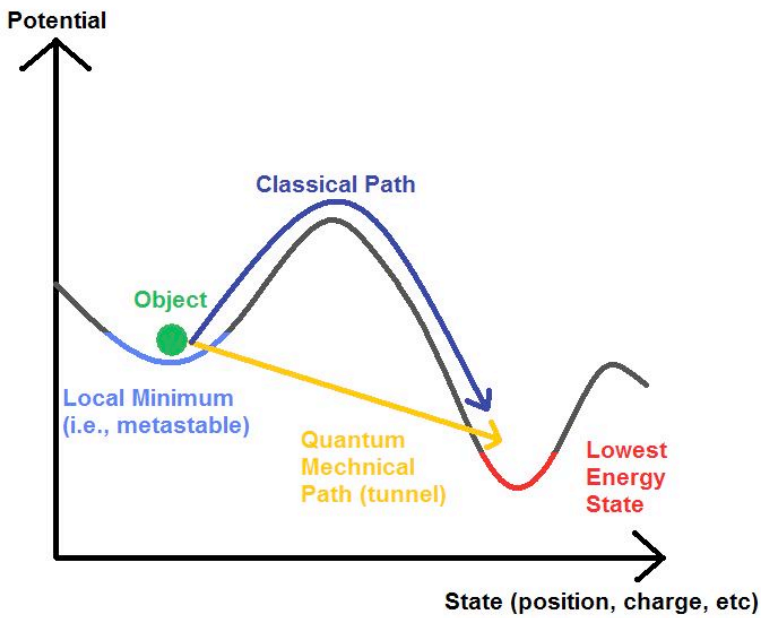

Figure 1.3: Cartoon diagram of quantum tunneling. Source: wikipedia.

exponentially as a function of the barrier width d:

$$|T|^2 \propto e^{-2\kappa d},$$

where $\kappa = \sqrt{\frac{2m(\mathcal{V}-E)}{\hbar^2}}$, $\mathcal{V}$ is the barrier height, E is the energy of the particle, m is the mass of the particle.

Early studies of tunneling of electrons between metals through thin oxide layers have culminated in the invention of the Esaki diode (16), the experimental demonstration of tunneling in superconductors by Ivar Giaever (17), and the discovery of the Josephson effect (18). In 1960 Ivar Giaever (17) invented a method to directly obtain the value of the superconducting gap and verify the specific form of the electronic density of states $\rho_{BCS}(V)$ (1.2) predicted by BCS theory. He performed a tunneling measurement on a contact which consisted of a superconductor separated from a normal metal by a thin insulating layer, as shown in Figure 1.4(a). Giaever surmised that provided there were a gap in the electronic density of states of a superconductor, the tunneling current would not flow between the metals, until the bias voltage applied between the metals reached the value of the superconducting gap. Indeed, as shown by John Bardeen (19), at small bias voltages, the differential tunneling conductance provides a measure of the tunneling density of states:

$$dI/dV(V) \propto \rho_{BCS}(V).$$

The shape of the $dI/dV(V)$ curve obtained by Giaever has reproduced the prediction of BCS

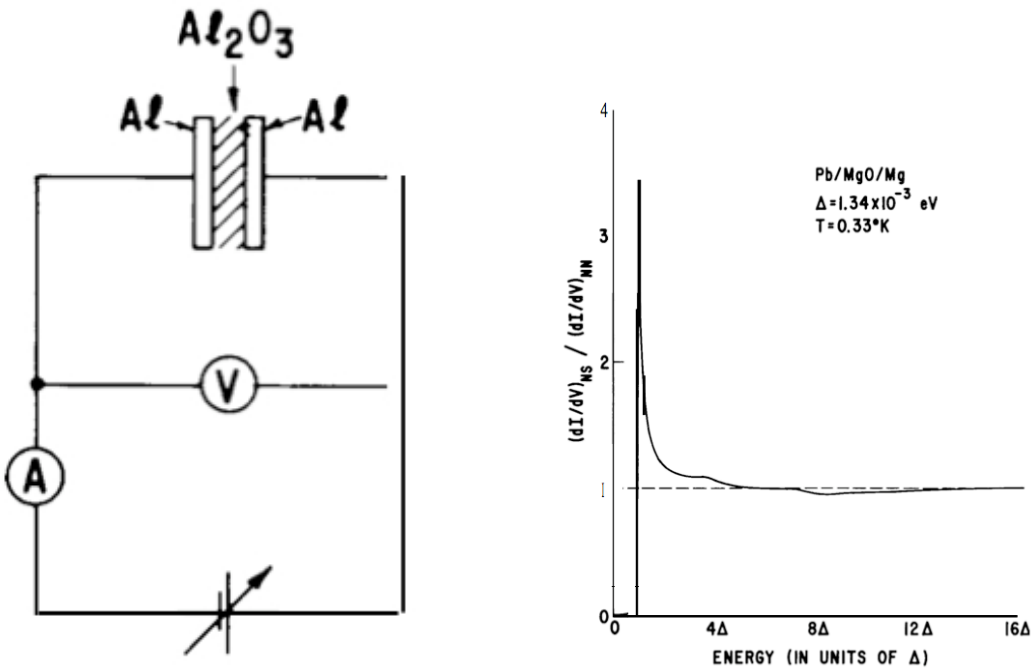

(a) (b)

Figure 1.4: Tunneling experiment by I. Giaever. (a): A schematic circuit diagram. Measured are the current-voltage characteristics of a capacitor-like arrangement formed by two aluminum films and an oxide. When the oxide thickness is less than 50 Å, an appreciable dc current flows through the oxide. (b): Differential tunneling conductance $dI/dV(V)$, which reproduced the BCS density of states. From I. Giaever's Nobel lecture, 1973.

theory (1.2) with a remarkable precision (compare Figures 1.4(b), 1.2(b)).

Following Giaever's experiments, John Bardeen (19) introduced a simple theory of tunneling. Using time-dependent perturbation theory, he showed that in a SIN junction the tunneling current is given by

$$I = \frac{4\pi e}{\hbar}|M|^2 \rho_S(E_S)\rho_N(E_S)$$

Here ρ_S, $\rho_N(E_S)$ are the densities of states of the superconductor and the normal metal taken at the Fermi energy, and M is the tunneling matrix element. The tunneling current decreases exponentially as a function of barrier width d:

$$I \propto e^{-2\kappa d},$$

where $\kappa = \sqrt{\frac{2m(\mathcal{V}-E)}{\hbar^2}}$. This rapid fall-off of the tunneling probability leads to a remarkable energy resolution. At small bias voltages of order the superconducting gap, $V \sim \Delta$, the barrier height $\mathcal{V}$ far exceeds the energy of the particle, $\mathcal{V} \gg E \sim \Delta$, so that the dependence of κ on the bias voltage is weak. Thus, tunneling is a weak-coupling probe which can probe inherent excitations of the material in a well-defined energy range.

1.3 Scanning Tunneling Spectroscopy

A new era in tunneling spectroscopy began in 1981, when Gerd Binnig and Heinrich Rohrer (21) invented a scanning tunneling microscope (STM), which allowed spatially resolved tunneling with sub-angstrom precision.

A scanning tunneling microscope involves a sharp metallic tip, which is brought to the sample surface within angstroms and is moved along the surface with piezoelectric transducers, as shown in Figure 1.5. A bias voltage, applied between the tip and the sample, induces a tunneling current.

According to a simplified tunneling theory (19; 20; 22), scanning tunneling spectroscopy probes the differential tunneling conductance at a location $\mathbf{r}$ and voltage V, which is proportional to the tunneling density of states:

$$\frac{dI}{dV}(\mathbf{r}, V) \propto |M(\mathbf{r}, V)|^2 \rho(\mathbf{r}, V),$$

where $M(\mathbf{r}, V)$ is the tunneling matrix element. In the WKB approach the tunneling matrix element is given by $|M(\mathbf{r})|^2 = e^{-2\gamma(\mathbf{r})}$ with $\gamma(\mathbf{r}) = \int_0^{d(\mathbf{r})} dx \sqrt{\frac{2m\phi(x)}{\hbar^2}}$, where $d(\mathbf{r})$ is the barrier width (tip-sample separation), $\phi(\mathbf{r})$ is the barrier height, which is a mixture of the work functions of the tip and the sample, m is the electron mass (66; 69). Thus, the tunneling conductance is a

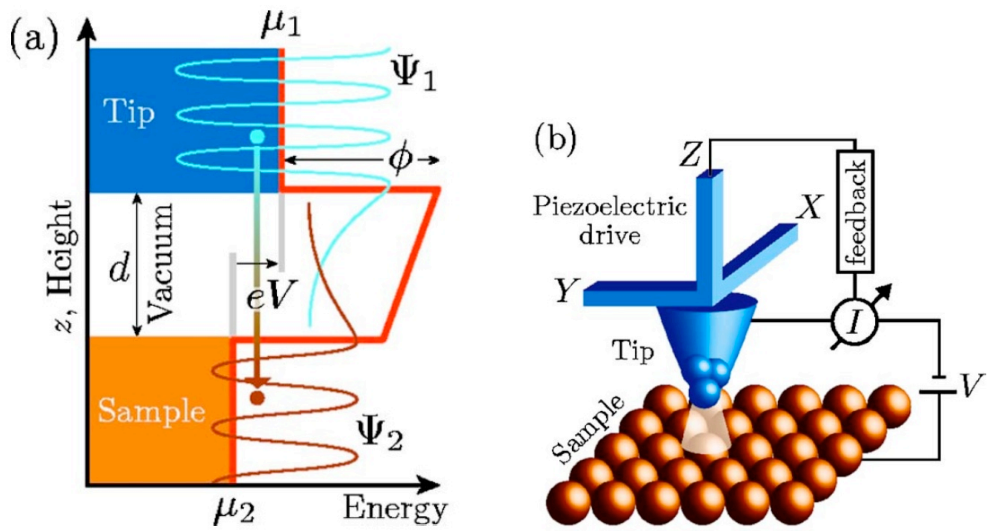

(a) (b)

Figure 1.5: Scanning tunneling microscope. (a): Tunneling process between the tip and the sample across a vacuum barrier of width d and height ϕ (for simplicity, the tip and the sample are assumed to have the same workfunction ϕ). The electron wave functions Ψ decay exponentially into vacuum with a small overlap, allowing electrons to tunnel from one electrode to the other. With a positive bias voltage V applied to the sample, electrons tunnel preferentially from the tip into unoccupied sample states. (b): Schematic view of the scanning tunneling microscope. After Ø. Fischer et al. (66).

measure of the thermally smeared local density of states (LDOS) of the sample at the position of the tip.

A most remarkable feature of STM is its unique resolution, achieved thanks to the exponential dependence of the tunneling current on the tip-sample separation d:

$$I \propto e^{-2\kappa d},\ \kappa = \sqrt{\frac{2m\overline{\phi}}{\hbar^2}} = .5\sqrt{\overline{\phi}(eV)}\text{Å}^{-1},$$

where $\overline{\phi}$ is an average value of the barrier height. For a typical $\overline{\phi} \sim 5$ eV, an angstrom increase in the tip-sample separation corresponds to an order of magnitude drop in the current. Lateral resolution is achieved using a sharp tip, which has well-localized atomic orbitals.

1.4 STM in copper oxide superconductors

A challenge to measure up to the potential of the new instrument soon presented itself, when Karl Mueller and Johannes Bednorz discovered high-temperature copper oxide (cuprate) superconductors in 1986. Especially surprising was the fact that the superconductivity was observed in ceramic materials, known as good insulators, never yet to be considered as possible hosts of superconductivity. In their stoichiometric form, the parents of copper oxide superconductors are

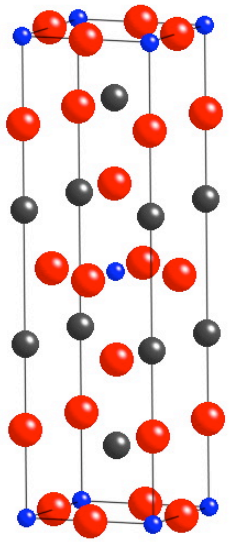

Figure 1.6: Structure of lanthanum copper oxide La_2CuO_4. The colors are as follows: O red, Cu blue, La black.

antiferromagnetic Mott insulators with strong interactions between the localized electrons in 3d shells. When doped with electrons or holes, these materials become superconductors. From the start, it was clear that the superconductivity in cuprates was unconventional, and that STM would play a major part in its investigation as one of the most direct probes of the electronic structure. The discovery generated a flurry of research activity, and initiated a renaissance in tunneling spectroscopy.

Now, more than twenty years after the discovery, remarkable progress has been made in understanding the cuprate superconductivity. For example, we know that the cuprate superconductivity is associated with condensation of Cooper pairs of electrons, as confirmed with flux quantization (23) and Josephson effect measurements (25). The spin state of pairs is known to be a singlet with an anisotropic orbital wavefunction with $d_{x^2-y^2}$ symmetry, as shown by flux quantization measurements in a tri-crystal YBCO junction (24). The superconducting coherence length ξ_0, which is a measure of the size of a Cooper pair, is of order 10-30 Å. Yet some key questions remain open, notably those concerning the pairing mechanism and the nature of the pseudogapped normal state, which we discuss in detail in the introduction to Chapter 2.

Cuprate superconductors have a layered structure of copper oxygen CuO_2 planes interchanged with planes of various oxides and rare earths. Figure 1.6 shows the structure of lanthanum copper oxide La_2CuO_4. The superconductivity is thought to be associated primarily with the copper oxygen planes.

In most copper oxide superconductors, STM and angular resolved photoemission (ARPES)

have found a large and doping-dependent gap, which fails to scale with T_c (66; 71; 42). The lack of univeral scaling suggests that the superconducting transition temperature T_c is not the only energy scale relevant to the superconductivity in cuprates, and that unlike in conventional BCS superconductors, the emergence of Cooper pairs does not simultaneously entail the formation of a macroscopic superconducting condensate with sample-wide phase coherence.

In copper oxide superconductors, a Cooper pair of two electrons has an orbital wavefunction with $d_{x^2-y^2}$ symmetry, so that the superconducting order parameter is given by:

$$\Delta(\mathbf{k}) = \frac{\Delta_0}{2}(cos\ k_x - cos\ k_y).$$

As a result of the $d_{x^2-y^2}$ symmetry, the gap vanishes along the directions of $k_x = \pm k_y$, where the Cooper pair wavefunction changes sign, as shown in Fig 1.2(d). Tunneling density of states $\rho(V)$ has contributions from quasiparticles with all the possible momenta. In the nodal directions, there are gapless low-energy quasiparticles. These gapless quasiparticles cause the tunneling density of states $\rho(V)$ to remain finite at finite bias voltages, as shown in Figure 1.2(e). Because the gap switches sign between different parts of the Brillouin zone, as shown in Figure 1.2(d), d-wave superconductivity is extremely fragile to disorder. Variations in the gap induced by disorder allow to probe the underlying nodal excitations with STM.

In cuprates, the superconducting transition temperature T_c changes as the carrier concentration x, e.g. the number of holes, is changed, as shown in Figure 1.7. As a function of doping, the superconducting transition temperature T_c follows a dome. Above the dome, in spite of the loss of the superconductivity, the single particle excitation spectrum retains a partial gap near the Fermi energy (31), known as the "pseudogap" (32). The key issues of the origin of the pseudogap and its relationship with the superconductivity currently remain under active investigation (36; 34).

As we discuss in more detail in the introduction to Chapter 2, STM studies have made major contributions to understanding cuprate superconductors, yet there is a sense that huge STM data arrays contain much more information to be extracted and analyzed. One of the most pressing questions in the field is how to improve the data analysis, so as to extract more information from STM data. A dominant trend in STM data analysis has been to interpret the data within a particular microscopic model, while using only basic data analysis tools. To decrease the reliance of the STM data interpretation on particular microscopic models, further advances in data analysis methods are necessary. In the context of current studies of cuprates, the key questions are:

- Is it possible to extract model-independent information from STM?

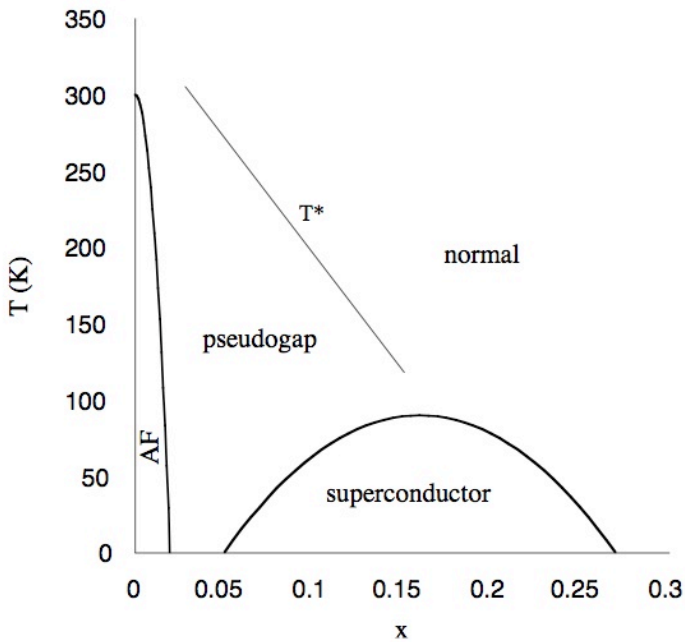

Figure 1.7: Schematic phase diagram of hole-doped copper oxide superconductors (temperature T vs. doping x). The parent compounds are antiferromagnetic Mott insulators. Hole doping transforms the materials into high-temperature superconductors. T^* denotes a temperature scale where the pseudogap forms.

- Is it possible to extract phase information from STM?

In Chapter 2 of this Thesis, we discuss how one can extract information about the phase of the order parameter from STM data. We show that symmetrized and anti-symmetrized correlators of local density of states give rise to observable coherence factor effects. In Chapter 3, we apply this framework to analyze the recent scanning tunneling experiments on an underdoped cuprate superconductor $Ca_{2-x}Na_xCuO_2Cl_2$ by T. Hanaguri et al. (60). In Chapter 4, we propose a model for nodal quasiparticle scattering in a disordered vortex lattice.

1.5 Tunneling in Kondo lattice systems

Nowadays, some of the most exciting new applications of scanning tunneling spectroscopy involve studies of Kondo lattice materials.

When a magnetic impurity is immersed in a sea of conduction electrons, it participates in virtual charge fluctuations, in which an electron briefly tunnels into the impurity or out of the impurity into the conduction sea (50; 52). The effect of these virtual charge fluctuations on the effective low-energy physics is to induce an antiferromagnetic interaction between the magnetic impurity and the conduction electrons. If the net coupling J between the magnetic impurity and

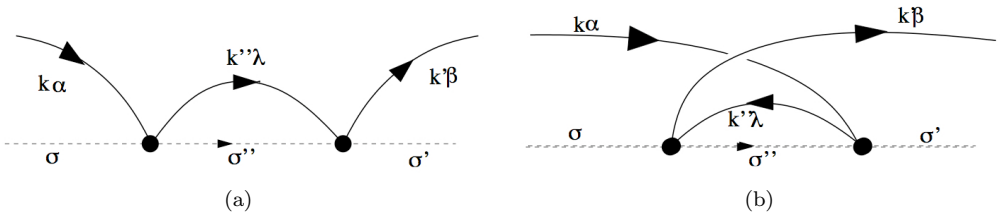

Figure 1.8: A diagrammatic representation of the spin-flip scattering in which a down-spin conduction electron (thick line) is scattered by the impurity (dotted line) into an intermediate spin-up state, after (52).

the conduction electrons is antiferromagnetic, the interaction scales to strong coupling at low temperatures of order T_K, the Kondo temperature, forming a Kondo resonance. The process driving this renormalization is spin-flip scattering, diagrammatically illustrated in Figure 1.8. The Kondo resonance scatters conduction electrons, enhancing the electrical resistivity at low temperatures, as shown in Figure 1.9(a). This phenomenon is known as the Kondo effect (47).

Immersed in a metal, a magnetic impurity produces Friedel oscillations in the spin density. As a result, in an alloy containing magnetic impurities in every unit cell, magnetic impurities are coupled with the so-called RKKY interaction (29):

$$H_{RKKY} = J_{RKKY}(\mathbf{x} - \mathbf{x}')\mathbf{S}(\mathbf{x}) \cdot \mathbf{S}(\mathbf{x}'),$$

where $J_{RKKY}(\mathbf{x} - \mathbf{x}') \equiv -J^2\chi(\mathbf{x} - \mathbf{x}')$ is the RKKY coupling, J is the Kondo coupling, $\mathbf{x}$, $\mathbf{x}'$ denote impurity positions. The characteristic scale of the RKKY interaction is given by $E_{RKKY} \sim J^2\rho$. If the Kondo temperature exceeds the RKKY interaction, $T_K \gg E_{RKKY}$, a dense Kondo ground state is formed (30), in which the impurity resonances scatter electrons in a coherent fashion and do not enhance the electrical resistivity, as shown in Figures 1.9(b), 1.10. Instead, the resonances work together to form strongly correlated metals with heavy quasiparticles. Such metals are known as Kondo lattice materials, examples of which include $CeCu_6$, $CeCoIn_5$, $YbRh_2Si_2$ and URu_2Si_2.

The Kondo effect involves the emergence of a composite heavy fermion formed by binding electrons on logarithmically large energy scales out to the band-width. These new electronic states are injected into the conduction electron sea near the Fermi energy. For a single impurity, this leads to a single isolated resonance. In a lattice, the presence of a new multiplet of fermionic states at each site leads to the formation of a coherent heavy electron band with an expanded Fermi surface, as illustrated in Figure 1.10.

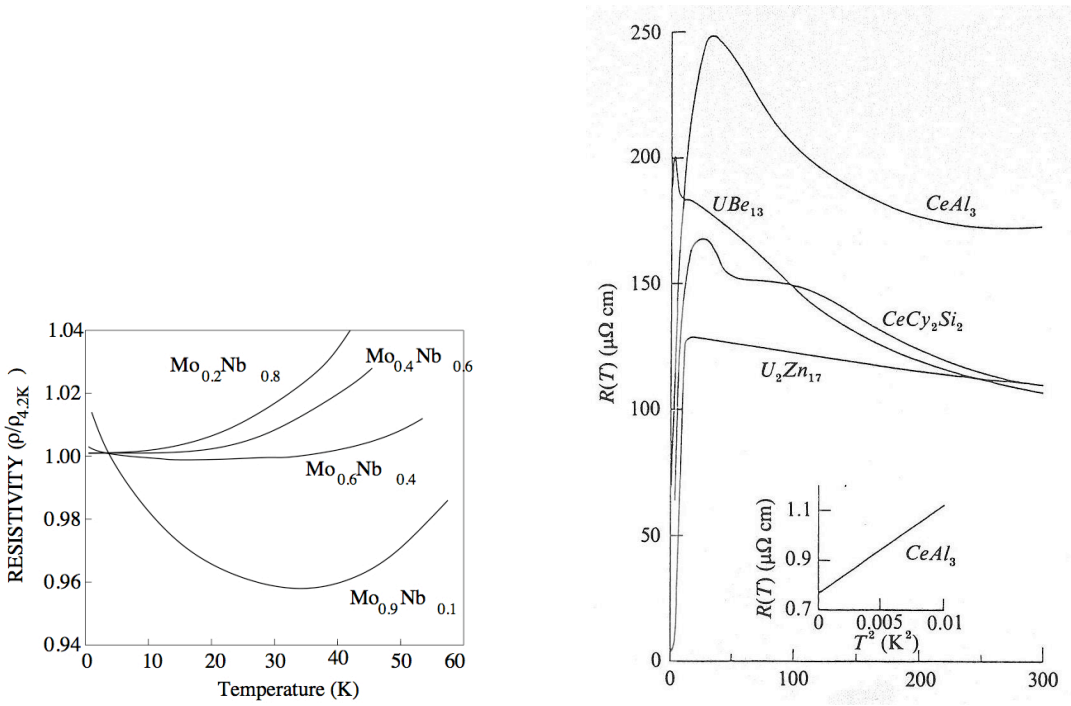

(a) (b)

Figure 1.9: Comparison of single impurity Kondo effect (a) and Kondo effect in a lattice environment (b). (a): Single impurity Kondo effect. Shown is the development of the resistivity minimuma for Fe in a series of $Mo - Nb$ alloys, after Sarachick et al., 1964 (49; 50). (b): Kondo effect in a lattice environment. Shown is the resistivity vs. temperature in select heavy fermion metals, after Fisk et al., 1986 (51). The origin of the resistivity maximum is the onset of coherence at T_K. At low temperatures, the resistivity reverts to a typical Fermi liquid behavior $\rho \propto T^2$, as shown in the inset.

1.5.1 STM studies of the single impurity Kondo problem

Tunneling studies of materials with magnetic impurities date back to early 1960's, when zero-bias voltage anomalies were observed in semiconductor p-n junctions and in tunnel junctions of normal metals separated by thin oxide films (111; 112). The explanation of the anomalies advanced by Appelbaum (121) and Anderson (122) invoked the Kondo effect, involving localized paramagnetic states in the oxide, due to transition metal impurities or interstital atoms of the transition metal near the metal-oxide interface.

In 1998 direct observation of the Kondo phenomenon with STM was achieved (55; 56). Madhavan et al. (55) studied individual cobalt (Co) atoms deposited in a gold host, at $T = 4$ K, well below $T_K = 19$ K. At impurity sites, the shape of the resonance was found to be asymmetric Fano-like, reflecting quantum interference between tunneling directly into the Kondo impurity state screened by the conduction electrons and tunneling into conduction electron states. Similar effects were later observed in quantum dots (57).

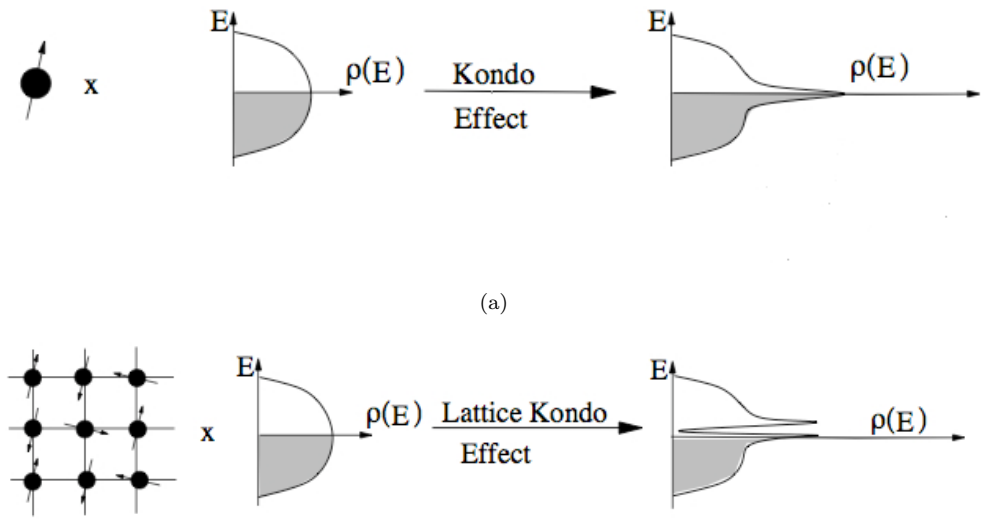

Figure 1.10: Comparison of single impurity Kondo effect and Kondo effect in a lattice environment, after P. Coleman, 2002 (52). (a): Single impurity Kondo effect builds a single fermionic level into the conduction sea, which gives rise to a resonance in the conduction electron density of states. (b): Lattice Kondo effect builds a fermionic resonance into the conduction sea in each unit cell. The elastic scattering off this lattice of resonances leads to formation of a heavy electron band, of width T_K.

1.5.2 Scanning tunneling spectroscopy as a probe of Kondo lattice materials

Kondo lattice materials contain localized electrons in 4f- or 5f-shells interacting with conduction electrons. At room temperatures, the f-electrons form local moments which lead to Curie susceptibility. As the material is cooled, the local moments get screened by the conduction electrons, and the local spins hybridized with the conduction electrons form heavy quasiparticles, which develop masses hundreds and even thousands times the bare electron mass (50; 52; 54). In the heavy electron state, elastic scattering at different sites of the Kondo lattice is coherent, so that the electrical resistance of the material drops (53). The advent of coherence is characterized by the formation of a large Fermi surface, which now includes both spins and conduction electrons, confirmed by de Haas - van Alphen measurements (54). Major open questions in the physics of Kondo lattice materials involve microscopic origins of the superconductivity and of the non-Fermi liquid behavior in the vicinity of quantum critical points (52). Superconductivity in Kondo lattice materials is most likely driven by the antiferromagnetic coupling (132).

To date, most of the experimental techniques applied to Kondo lattice materials have been bulk probes. Aside from point contact spectroscopy and de Haas - van Alphen studies, few

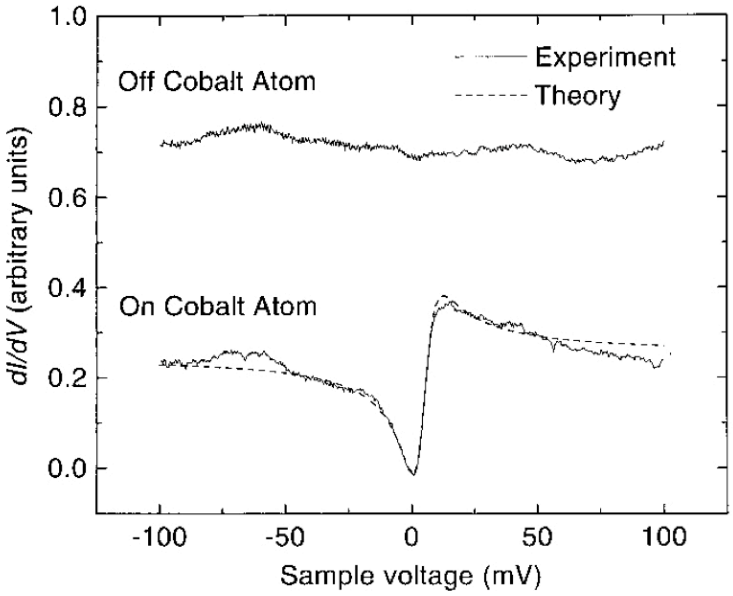

Figure 1.11: Observation of Fano resonance in STM experiments on Co:Au by Madhavan et al., 1998 (55). A pair of $dI/dV(V)$ spectra taken from the STM tip held over a single Co atom and over the nearby bare Au surface (a constant slope has been subtracted from both curves, and they have been shifted vertically). The feature identified as a Kondo resonance appears over the Co atom. Dashed curve shows a fit to the data with a modified Fano theory.

experimental techniques have probed Kondo lattice materials at the microscopic level.

Recently, scanning tunneling studies of a Kondo lattice material URu_2Si_2 became possible (117). If it proves possible to apply scanning tunneling spectroscopy to Kondo lattice materials, then remarkable new opportunities in the ongoing investigation may emerge.

Tunneling into a lattice of spins calls for a special discussion. Whilst STM is probing low-energy excitations, a spin represents a high-energy state. Yet it does participate in tunneling, via a virtual co-tunneling mechanism (123). In a virtual co-tunneling mechanism, a low-energy electron from the tip tunnels into a conduction electron state in the metal, which participates in spin-flip scattering off a magnetic impurity. During the spin-flip scattering off the magnetic impurity, the conduction electron tunnels into a high-energy f-electron state of the impurity, while the f-electron tunnels out of the impurity into the conduction sea. Thus, in a Kondo lattice, a tip electron has two tunneling routes: direct tunneling route into the conduction band, and the co-tunneling route, which involves a magnetic impurity of the Kondo lattice, as shown in Figure 1.12. The coexistence of the two tunneling routes in Kondo lattices causes interference effects, observed in the tunneling current $I(eV)$:

$$\frac{dI}{dV}(eV) \propto |\Psi_1(E) + \Psi_2(E)|^2|_{E=eV},$$

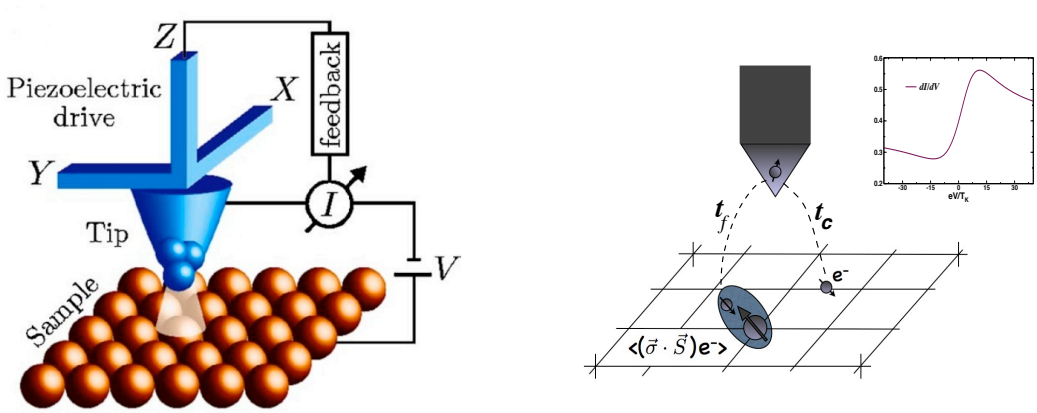

(a) (b)

Figure 1.12: Comparison of (a): Tunneling in cuprates, where a single tunneling route is available, and (b): Tunneling in Kondo lattices, where direct tunneling into the conduction band coexists with co-tunneling. (b): Tunneling of an electron from a tip into a heavy-fermion material involves two types of processes. The first one corresponds to the tunneling with an amplitude t_c into conduction sites. The second one consists of tunneling with an amplitude t_f into the composite states between the conduction electrons and local magnetic f-moments. These composite states represent the fabric of the coherent heavy-fermion state of the Kondo lattice formed below coherence temperature T_K. The inset shows the typical differential conductance curve as a function of voltage at temperatures well below T_K.

where $\Psi_1(E)$ is the amplitude for direct tunneling into the conduction band, and $\Psi_2(E) = [\text{spin-flip}] \times \Psi_1(E)$ is the co-tunneling amplitude. A comparison of tunneling in cuprates, where a single tunneling route into the electronic band is available, and tunneling in Kondo lattices, where direct tunneling into the conduction band coexists with co-tunneling, is given in Figure 1.12.

In Chapter 5, we examine the effect of co-tunneling to develop a theory of tunneling into a Kondo lattice. We find that the interference between the direct tunneling and the co-tunneling channels leads to a novel asymmetric lineshape, which has two peaks and a gap. The presence of the peaks suggests that the interference is more dramatic in the case of Kondo lattice than in the single impurity case, because of the coherence. These features should be observed in future tunneling experiments on Kondo lattice materials.

Chapter 2
Coherence factors in STM measurement

2.1 Introduction

In the superconducting state, strongly correlated materials, such as copper oxide superconductors, tend to retain a partially gapped Fermi surface, with nodes, which form to help escape strong Coulomb interaction. In the case of underdoped cuprates, even the normal state retains a gap in the single-particle excitation spectrum, the so-called "pseudogap" (see Figure 1.7). Originally observed in nuclear magnetic resonance studies (33) as a rapid suppression of low-frequency spectral weight setting in at $T^* \gg T_c$, far above the superconducting transition temperature T_c, the pseudogap manifests itself in both charge and spin dynamics (32; 36).

No consensus has been reached on the origin of the pseudogap and its relation to the superconductivity. There are two broad classes of theories for the origin of the pseudogap:

- "alternative order" theories (37; 38; 39; 40; 41), suggesting that the pseudogap is associated with another type of order, different from Cooper pairing, and
- "superconductivity precursor" theories (35; 36).

Examples of the "alternative orders" proposed in the pseudogap region include charge density wave, spin density wave, d-density wave (39), circulating currents (40), staggered fluctuating currents (37) and stripes. The "superconductivity precursor" theories argue that in the pseudogap state, the material is a phase-fluctuating superconductor, which superconducts at short length scales, but fails to superconduct at long length scales because of lack of phase coherence (35; 36). It has been suggested that Cooper pairs form at $T^* \gg T_c$, a temperature scale related to the pseudogap, and condense at the superconducting transition temperature T_c (42; 43; 44). Recent STM experiments support the phase-fluctuating superconductor scenario (42).

2.2 STM as a probe of nodal quasiparticles

A number of studies have employed STM to help sort out the pseudogap origin controversy. In particular, Fourier Transform Scanning Tunneling Spectroscopy (FT-STS) has been used to

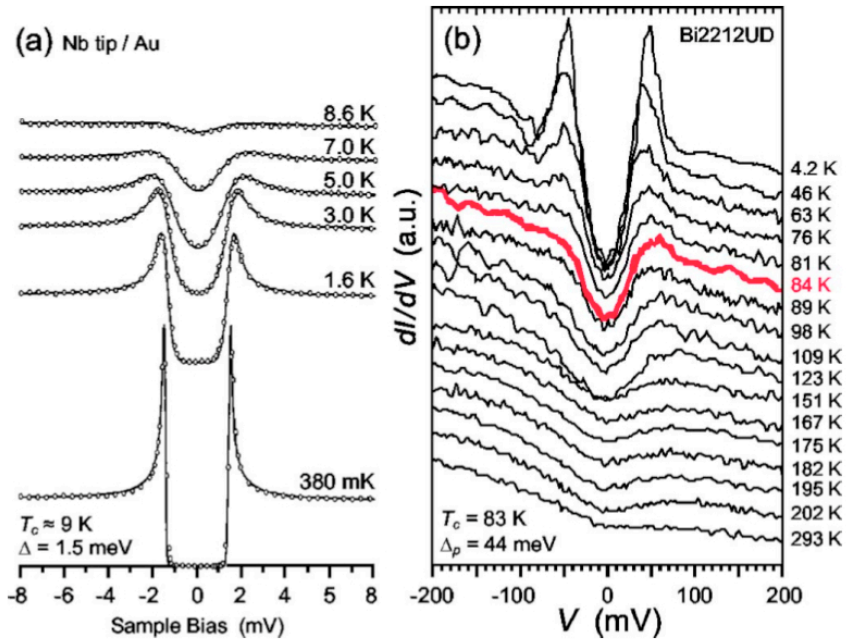

Figure 2.1: T dependences of the DOS measured by STM. (a): Junction between a gold sample and a niobium tip with $T_c \approx 9$ K, $\Delta_p = 1.5$ meV. Adapted from Pan et al. (28). (b): Junction between an iridium tip and underdoped Bi2212 with $T_c \approx 83$ K, $\Delta_p = 44$ meV, and T^* near room temperature. Adapted from Renner et al. (27), after Ø. Fischer et al. (66).

search for possible alternative orders. In such experiments, the STM tip is scanned over a large field of view of order 600 Å× 600 Å, collecting the map of $dI/dV(\mathbf{r}, V)$, which is then Fourier transformed and examined for possible patterns. In cuprates, the resulting $dI/dV(\mathbf{q}, V)$ maps are dominated by a small set of q-vectors.

Modulations of local density of states (LDOS) were first reported by C. Howald et al. (68) in a magnetic field. Using FT-STM, J.E. Hoffman et al. (70) have found zero-field LDOS modulations, which dispersed with bias voltage. A further study by K. McElroy et al. (71) has identified eight dispersive peaks in $dI/dV(\mathbf{q}, V)$ maps, which dominated the patterns in momentum space, as shown in Figure 2.2(a). Q.-H. Wang and D.-H. Lee (73) have proposed that the origin of the dispersive LDOS modulations was quasiparticle interference.

A well-known phenomenon in metals, quasiparticle interference (QPI), involves scattering of low-frequency excitations off certain perturbations, such as disorder and crystal defects. When a wave with momentum $\mathbf{k}_i$ scatters into a wave with momentum $\mathbf{k}_f$, a modulation of $\mathbf{q} = \mathbf{k}_f - \mathbf{k}_i$ is observed in the interference landscape. Indeed, in conventional metals and semiconductors, QPI has been widely used to determine the surface band structures (81; 82; 83).

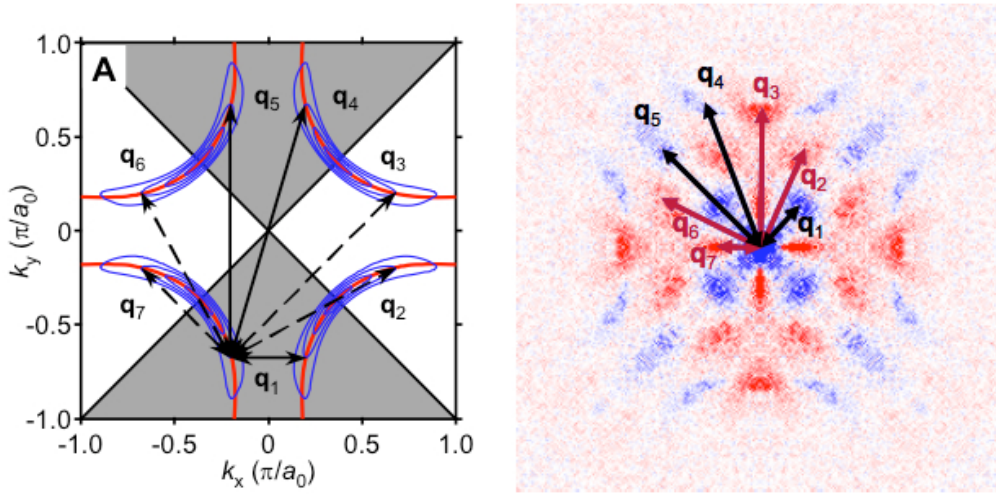

(a) (b)

Figure 2.2: Quasiparticle interference (QPI) patterns in a high-Tc cuprate analyzed in terms of "octet" model. (a): QPI patterns observed in $Ca_{2-x}Na_xCuO_2Cl_2$ (60). (b): Schematic representation of **k**-space electronic states in a high-Tc cuprate. Normal-state Fermi surface (red curves) and contours of constant energy for Bogoliubov quasiparticles (blue curves) in the 1st Brillouin zone. White and shaded areas represent **k**-space regions with opposite signs of d-wave superconducting gap. Arrows denote scattering **q**-vectors responsible for QPI patterns.

In an STM experiment the differential tunneling conductance is obtained, which is proportional to local density of states (22):

$$\frac{dI}{dV}(\mathbf{r}, eV) \propto \rho(\mathbf{r}, eV).$$

Quenched disorder produces fluctuations in the local density of states $\rho(\mathbf{r}, eV)$:

$$\delta\rho(\mathbf{r}, eV) = \rho(\mathbf{r}, eV) - \overline{\rho(\mathbf{r}, eV)}.$$

The quantity of greatest interest is the fluctuation in the Fourier transformed local density of states in response to the impurity potential, $\delta\rho(\mathbf{q}, eV)$. According to the quasiparticle interference interpretation of the experiment, these fluctuctuations are proportional to the scattering rates of the low-energy (Bogoliubov) quasiparticles:

$$\delta\rho(\mathbf{q}, eV) \propto \Sigma_{\mathbf{k}} w_{\mathbf{k}\to\mathbf{k}+\mathbf{q}}(eV).$$

In cuprates, low-energy quasiparticles have a dispersion

$$E(\mathbf{k}) = \sqrt{\varepsilon(\mathbf{k})^2 + \Delta(\mathbf{k})^2},$$

where $\varepsilon(\mathbf{k})$ and $\Delta(\mathbf{k})$ are dispersion relations of normal-state band and superconducting gap, respectively (78; 79). In high-Tc cuprates, the superconducting gap has $d_{x^2-y^2}$-wave symmetry

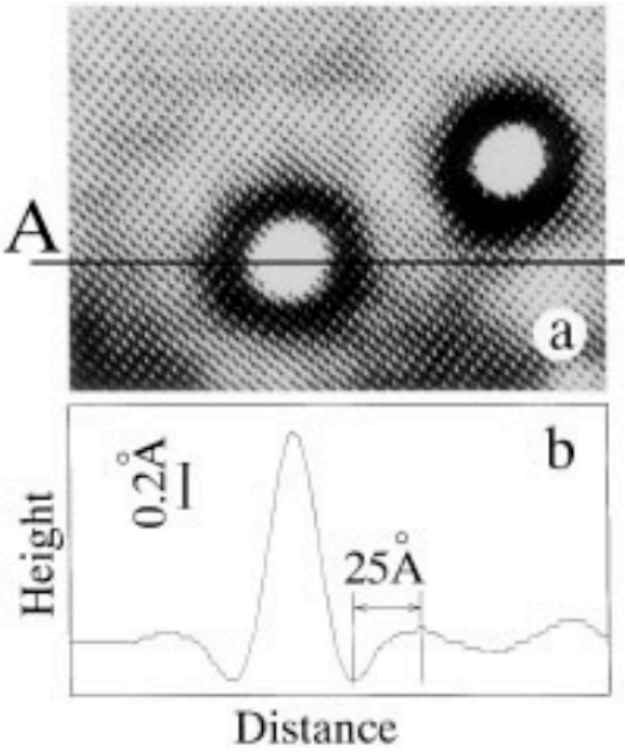

Figure 2.3: Fridel oscillations around incorporated Si_{Ga} dopants in $GaAs$ observed with STM. (a): STM image of the (110)-cleaved, 2×10^{18} cm^{-3} Si-doped GaAs surface. Scan size 220 Å× 150 Å. The relative tip height is given by a grey scale, from 0 to 1.3 Å. Set-point current is 40 pA, sample voltage -2.5 V. Two dopant-induced features are displayed. Each feature consists of a bright spot in the middle, surrounded by a black ring and another white ring. The outermost ring is more pronounced in (b). (b): Cross section through the middle of the left feature along line A. The atomic lattice is filtered out. Clearly the two maxima of the outermost ring and the minima of the dark ring can be seen. After M.C.M.M. van der Wielen et al. (67).

(84) and vanishes along the $(\pm\pi, \pm\pi)$ directions (diagonals of the unit cell). The dispersion $E(\mathbf{k})$ gives rise to four "banana-shaped" contours of constant energy, as shown in Figure 2.2(a).

As we have mentioned above, QPI patterns in high-Tc cuprates are dominated by a small set of peaks, which have been analyzed with the so-called "octet" model (71; 73). The "octet" model suggests that the positions of the peaks in quasiparticle interference patterns $dI/dV(\mathbf{q}, V)$ are given by the q-vectors connecting points on the constant-energy contours with the largest density of states. According to the "octet" model, the amplitudes of the standing waves become large if the momentum transfer $\mathbf{q}$ connects the ends of the "bananas", where the joint DOS is the largest. This determines the locations of seven distinct scattering vectors ($\mathbf{q}_i$ $(i = 1 - 7)$ in q space. The quasiparticle states located at the ends of the bananas lie on the normal state Fermi surface (red curves in Figure 2.2(a)), where $\varepsilon(\mathbf{k}) = 0$, and the energy $E(\mathbf{k}) = |\Delta(\mathbf{k})|$ at these points corresponds to the magnitude of superconducting gap.

The "octet" model is based on Fermi's golden rule (69). For elastic scattering in a metal, the scattering amplitude is given by

$$w(i \to f) \propto \frac{2\pi}{\hbar} n_i(\mathbf{k}_i, E) n_f(\mathbf{k}_f, E) |V(\mathbf{q})|^2,$$

where $V(\mathbf{q})$ is the scattering potential, $\mathbf{q} = \mathbf{k}_f - \mathbf{k}_i$ is the momentum transfer, $n_i(\mathbf{k}_i, E)$ and $n_f(\mathbf{k}_f, E)$ are the occupation numbers for the initial and the final states,

$$n(\mathbf{k}, E) \propto \frac{1}{|\nabla_{\mathbf{k}}(E)|}.$$

The scattering amplitude is maximal, when the joint density of states,

$$JDOS(\mathbf{k}_i, \mathbf{k}_f) \equiv n_i(\mathbf{k}_i, E) n_f(\mathbf{k}_f, E),$$

is maximal, which happens, when the gradients $|\nabla_{\mathbf{k}}(E)|$ for $\mathbf{k} = \mathbf{k}_i, \mathbf{k}_f$ are minimized. According to the "octet" model, these points are located at the ends of the "banana"-shaped contours.

2.3 Coherence factor effects in superconductors

Fundamental studies of unconventional superconductors are currently hindered by the scarcity of direct methods to determine the structure of the superconducting order parameter. Apart from Josephson junction experiments, few spectroscopic probes provide the valuable information about the phase of the order parameter. In this Chapter, we discuss how phase sensitive coherence effects can be studied using scanning tunneling spectroscopy/microscopy (STS/STM).

The key idea is that the evolution of the phase of the order parameter in momentum space can be determined from the Fourier transformed fluctuations in the tunneling density of states.

The sensitivity of these fluctuations to the scattering rates of superconducting quasiparticles manifests itself through coherence factor effects. Quasiparticles in a superconductor are a coherent superposition of excitations of electrons and holes. Coherence factors characterize how the scattering rate of a superconducting quasiparticle off a given scatterer differs from the scattering rate of a bare electron off the same scatterer (77). Coherence factors are determined by combinations of the Bogoliubov coefficients $u_{\mathbf{k}}$ and $v_{\mathbf{k}}$, which give proportions of the particle and hole components that constitute a superconducting quasiparticle,

$$c_{\mathbf{k}\uparrow} = u_{\mathbf{k}} a_{\mathbf{k}\uparrow} + v_{\mathbf{k}} a^{\dagger}_{-\mathbf{k}\downarrow}, \tag{2.1}$$

$$c_{\mathbf{k}\downarrow} = -v_{\mathbf{k}} a^{\dagger}_{\mathbf{k}\downarrow} + u_{\mathbf{k}} a_{-\mathbf{k}\uparrow}. \tag{2.2}$$

The momentum-dependent order parameter $\Delta_{\mathbf{k}} = |\Delta_{\mathbf{k}}| e^{i\phi(\mathbf{k})}$ has the same sign as the Bogoliubov coefficient $v_{\mathbf{k}}$, so that studies of scattering rates of quasiparticles with different momenta can delineate how the phase of the order parameter $\phi(\mathbf{k})$ changes in momentum space.

In isotropic s-wave superconductors, coherence factor effects were originally observed as anomalies in temperature dependencies of various measurable quantities, which involve scattering rates of superconducting quasiparticles. For example, in s-wave superconductors, nuclear spin relaxation rate (13) and infrared absorption rate (15), quantities associated with interaction of the quasiparticles with an electromagnetic field, exhibit an enhancement just below the superconducting transition temperature T_c, known as the Hebel-Slichter peak. By contrast, ultrasonic attenuation rate, associated with scattering of superconducting quasiparticles off a scalar potential, is depressed just below the superconducting transition temperature T_c (14), relative to that of a normal metal.

In d-wave superconductors, coherence factor effects are typically suppressed by a strong anisotropy of the superconducting gap $\Delta(\mathbf{k})$ (80). However, scanning tunneling spectroscpy does provide an opportunity to observe coherence factor effects in a d-wave superconductor, as we discuss next.

In studies of unconventional superconductors with spatially varying order parameter, scanning tunneling spectroscopy provides a spectroscopic probe with a real space resolution at the atomic level. In the past, observation of phase sensitive coherence effects with STM has been thwarted by the problem of controlling the scatterers (69). An ingenious solution of this problem has been found in the application of a magnetic field, which introduces vortices as controllable scatterers in a given system (60).

In this Chapter, we develop a framework for observation of coherence factor effects with Fourier Transform Scanning Tunneling Spectroscopy (FT-STS).

2.4 LDOS correlators R^{even} and R^{odd} have well-defined coherence factors

We describe the electron field inside a superconductor by a Balian-Werthammer spinor (74)

$$\Psi(\mathbf{r},\tau) = \begin{pmatrix} \psi_\uparrow(\mathbf{r},\tau) \\ \psi_\downarrow(\mathbf{r},\tau) \\ \psi_\downarrow^\dagger(\mathbf{r},\tau) \\ -\psi_\uparrow^\dagger(\mathbf{r},\tau) \end{pmatrix},$$

where $\mathbf{r}$ denotes real space coordinates and τ is imaginary time. The Nambu Green's function is defined as the ordered average

$$\hat{G}_{\alpha\beta}(\mathbf{r}',\mathbf{r};\tau) = -\langle T_\tau \Psi_\alpha(\mathbf{r}',\tau)\Psi_\beta^\dagger(\mathbf{r},0)\rangle. \tag{2.3}$$

Tunneling measurements determine local density of states, which is given by

$$\rho(\mathbf{r},\omega) = \frac{1}{\pi}\, Im\ \mathrm{Tr}\ \frac{1+\tau_3}{2}\left[G(\mathbf{r},\mathbf{r};\omega - i\delta)\right], \tag{2.4}$$

where $G(\mathbf{r}',\mathbf{r};z)$ is the analytic continuation $G(\mathbf{r}',\mathbf{r};i\omega_n) \to G(\mathbf{r}',\mathbf{r};z)$ of the Matsubara Green's function

$$G(\mathbf{r}',\mathbf{r};i\omega_n) = \int_0^\beta G(\mathbf{r}',\mathbf{r};\tau)e^{i\omega_n\tau}d\tau, \tag{2.5}$$

with $\omega_n = (2n+1)\pi T$. The appearance of the combination $\frac{1+\tau_3}{2}$ in (2.4) projects out the normal component of the Nambu Green's function

$$Tr\ \frac{1+\tau_3}{2}\ G(\mathbf{r}',\mathbf{r};\tau) = -\sum_\sigma \langle T_\tau \psi_\sigma(\mathbf{r}',\tau)\psi_\sigma^\dagger(\mathbf{r},0)\rangle. \tag{2.6}$$

The mixture of the unit and the τ_3 matrices in this expression prevents the local density of states from developing a well-defined coherence factor. We now show that the components of the local density of states that have been symmetrized or antisymmetrized in the bias voltage have a well-defined coherence factor. The key result here is that

$$\rho(\mathbf{r},\omega) \pm \rho(\mathbf{r},-\omega) = \frac{1}{\pi}\, Im\ \mathrm{Tr}\ \left[\left\{\begin{matrix} 1 \\ \tau_3 \end{matrix}\right\} G(\mathbf{r},\mathbf{r};\omega - i\delta)\right]. \tag{2.7}$$

In particular, this implies that the antisymmetrized density of states has the same coherence factor as the charge density operator τ_3.

To show these results, we introduce the "conjugation matrix" $C = \sigma_2\tau_2$, whose action on the Nambu spinor is to conjugate the fields,

$$C\Psi = (\Psi^\dagger)^T \equiv \Psi^*, \tag{2.8}$$

effectively taking the Hermitian conjugate of each component of the Nambu spinor. This also implies that $\Psi^\dagger C = \Psi^T$. Here τ_i are Pauli matrices acting in particle-hole space, for example,

$$\tau_{\mathbf{3}} = \begin{pmatrix} \underline{1} & 0 \\ 0 & -\underline{1} \end{pmatrix},$$

and σ_i are Pauli matrices acting in spin space,

$$\sigma_{\mathbf{i}} = \begin{pmatrix} \underline{\sigma_i} & 0 \\ 0 & \underline{\sigma_i} \end{pmatrix}.$$

Using (2.8), it follows that

$$\begin{aligned} [CG(\mathbf{r}',\mathbf{r};\tau)C]_{\alpha\beta} &= -\langle T_\tau C\Psi(\mathbf{r}',\tau)\Psi^\dagger(\mathbf{r},0)C\rangle_{\alpha\beta} \\ &= -\langle T_\tau \Psi^*_\alpha(\mathbf{r}',\tau)\Psi^T_\beta(\mathbf{r},0)\rangle \\ &= \langle T_\tau \Psi_\beta(\mathbf{r},0)\Psi^\dagger_\alpha(\mathbf{r}',\tau)\rangle \\ &= -G_{\beta\alpha}(\mathbf{r},\mathbf{r}',-\tau), \end{aligned} \tag{2.9}$$

or, in the matrix notation,

$$CG(\mathbf{r},\mathbf{r}';\tau)C = -G^T(\mathbf{r}',\mathbf{r};-\tau), \tag{2.10}$$

which in turn implies for the Matsubara Green's function (2.5)

$$CG(\mathbf{r},\mathbf{r}';i\omega_n)C = -G^T(\mathbf{r}',\mathbf{r};-i\omega_n). \tag{2.11}$$

For the advanced Green's function, which is related to the Matsubara Green's function via analytic continuation, $G(\mathbf{r},\mathbf{r}',i\omega_n) \to G(\mathbf{r},\mathbf{r}',z)$, we obtain

$$CG(\mathbf{r},\mathbf{r}';\omega - i\delta)C = -G^T(\mathbf{r}',\mathbf{r};-\omega + i\delta). \tag{2.12}$$

Using this result and the commutation relations of Pauli matrices, we obtain

$$\begin{aligned} \rho(\mathbf{r},-\omega) = -\frac{1}{\pi}\, Im\ \mathrm{Tr}\ \frac{1+\tau_3}{2}\ G(\mathbf{r},\mathbf{r};-\omega+i\delta) = \\ = \frac{1}{\pi}\, Im\ \mathrm{Tr}\ \frac{1+\tau_3}{2}\ C\ G^T(\mathbf{r},\mathbf{r};\omega-i\delta)\ C = \\ = \frac{1}{\pi}\, Im\ \mathrm{Tr}\ \frac{1-\tau_3}{2}\ G(\mathbf{r},\mathbf{r};\omega-i\delta). \end{aligned} \tag{2.13}$$

Finally, we obtain

$$\begin{aligned} \rho(\mathbf{r},\omega) \pm \rho(\mathbf{r},-\omega) = \frac{1}{\pi}\, Im\ \mathrm{Tr}\ \left[\frac{1+\tau_3}{2}\ G(\mathbf{r},\mathbf{r};\omega-i\delta) \pm \frac{1-\tau_3}{2}\ G(\mathbf{r},\mathbf{r};\omega-i\delta)\right] = \\ = \frac{1}{\pi}\, Im\ \mathrm{Tr}\ \left[\left\{\begin{matrix} 1 \\ \tau_3 \end{matrix}\right\} G(\mathbf{r},\mathbf{r};\omega-i\delta)\right]. \end{aligned} \tag{2.14}$$

2.5 Coherence factors in a BCS superconductor, T-matrix approximation

Next, applying this result to a BCS superconductor, we show that in the t-matrix approximation, coherence factors that arise in the conductance ratio $Z(\mathbf{q}, V)$ are given by a product of the coherence factors associated with the charge operator and the scattering potential.

T-matrix approximation (75; 76) allows to compute the Green's function in the presence of multiple scattering off impurities. In terms of the bare Green's function $G(\mathbf{k}, \omega)$ and the impurity t-matrix $\hat{t}(\mathbf{k}, \mathbf{k}')$, the full Green's function is given by

$$\tilde{G}(\mathbf{k}, \mathbf{k}', \omega) = G(\mathbf{k}, \omega) + G(\mathbf{k}, \omega)\hat{t}(\mathbf{k}, \mathbf{k}')G(\mathbf{k}', \omega) = G(\mathbf{k}, \omega) + \delta G(\mathbf{k}, \mathbf{k}', \omega). \tag{2.15}$$

Using this expression, we obtain for the Fourier transformed odd fluctuations in the tunneling density of states

$$\begin{aligned} \delta\rho^{odd}(\mathbf{q}, \omega) &= \frac{1}{2\pi}\mathrm{Im}\int_{\mathbf{k}} \mathrm{Tr}\Big[\tau_3 \delta G_{\mathbf{k}_+, \mathbf{k}_-}(\omega - i\delta)\Big] = \\ &= \frac{1}{2\pi}\mathrm{Im}\int_{\mathbf{k}} \mathrm{Tr}\Big[\tau_3 G_{\mathbf{k}_-}(\omega - i\delta)\hat{t}(\mathbf{q}, \mathbf{k})G_{\mathbf{k}_+}(\omega - i\delta)\Big]. \end{aligned} \tag{2.16}$$

The Fourier transformed even fluctuations in the tunneling density of states

$$\begin{aligned} \delta\rho^{even}(\mathbf{q}, \omega) &= \frac{1}{2\pi}\mathrm{Im}\int_{\mathbf{k}} \mathrm{Tr}\Big[\delta G_{\mathbf{k}_+, \mathbf{k}_-}(\omega - i\delta)\Big] = \\ &= \frac{1}{2\pi}\mathrm{Im}\int_{\mathbf{k}} \mathrm{Tr}\Big[G_{\mathbf{k}_-}(\omega - i\delta)\hat{t}(\mathbf{q}, \mathbf{k})G_{\mathbf{k}_+}(\omega - i\delta)\Big]. \end{aligned} \tag{2.17}$$

For scattering off a single impurity with a scattering potential $\hat{U}(\mathbf{k}, \mathbf{k}')$, the t-matrix $\hat{t}(\mathbf{k}, \mathbf{k}')$ denotes the infinite sum

$$\begin{aligned} \hat{t}(\mathbf{k}, \mathbf{k}') &= \hat{U}(\mathbf{k}, \mathbf{k}') + \sum_{\mathbf{k}''} \hat{U}(\mathbf{k}, \mathbf{k}'')G(\mathbf{k}'', \omega)\hat{U}(\mathbf{k}'', \mathbf{k}') + ... = \\ &= \hat{U}(\mathbf{k}, \mathbf{k}') + \sum_{\mathbf{k}''} \hat{U}(\mathbf{k}, \mathbf{k}'')G(\mathbf{k}'', \omega)\hat{t}(\mathbf{k}'', \mathbf{k}'). \end{aligned} \tag{2.18}$$

Working in the Born approximation, which is equivalent to taking only the first term in the series (2.18), we derive the expressions for the coherence factors associated with some common scattering processes that arise in the even and odd density-density correlators $R^{even}(\mathbf{q}, V)$ and $R^{odd}(\mathbf{q}, V)$ in a BCS superconductor (see Table 2.1). We use the following expression for the BCS Green's function for an electron with normal state dispersion $\epsilon_{\mathbf{k}}$ and gap function $\Delta_{\mathbf{k}}$:

$$G_{\mathbf{k}}(\omega) = [\omega - \epsilon_{\mathbf{k}}\tau_3 - \Delta_{\mathbf{k}}\tau_1]^{-1}, \tag{2.19}$$

$\hat{t}(\mathbf{q}, \mathbf{k})$ is the scattering t-matrix of the impurity potential, and $\mathbf{k}_\pm = \mathbf{k} \pm \mathbf{q}/2$. If the scattering potential has the t-matrix given by $\hat{t}(\mathbf{q}, \mathbf{k}) = T_3(\mathbf{q})\ \tau_3$, corresponding to a weak scalar (charge)

scatterer, the change in the odd part of the Fourier transformed tunneling density of states becomes $\delta\rho^{odd}_{scalar}(\mathbf{q},\omega) = T_3(\mathbf{q})\ \Lambda^{odd}_{scalar}(\mathbf{q},\omega)$ with

$$\Lambda^{odd}_{scalar}(\mathbf{q},\omega) = \frac{1}{2\pi}\mathrm{Im}\int_k \left[\frac{z^2+\epsilon_{\mathbf{k}_+}\epsilon_{\mathbf{k}_-}-\Delta_{\mathbf{k}_+}\Delta_{\mathbf{k}_-}}{(z^2-E^2_{\mathbf{k}_+})(z^2-E^2_{\mathbf{k}_-})}\right]_{z=\omega-i\delta}, \tag{2.20}$$

where $E_{\mathbf{k}} = [\epsilon^2_{\mathbf{k}}+\Delta^2_{\mathbf{k}}]^{\frac{1}{2}}$ is the quasiparticle energy. Expressed in terms of the Bogoliubov coefficients $u_{\mathbf{k}}$ and $v_{\mathbf{k}}$, given by

$$u^2_k(v^2_k) = \frac{1}{2}(1\pm\epsilon_k/E_k)$$

, the expression under the integral in (2.20) is proportional to $(u_+u_- - v_+v_-)^2$.

Fluctuations in the even part of the Fourier transformed tunneling density of states due to scattering off a scalar impurity are substantially smaller, $R^{even}_{scalar}(\mathbf{q},\omega) \ll R^{odd}_{scalar}(\mathbf{q},\omega)$, where $R^{even(odd)}_{scalar}(\mathbf{q},\omega)$ is defined by (2.32), $\delta\rho^{even}_{scalar}(\mathbf{q},\omega) = T_3(\mathbf{q})\ \Lambda^{even}_{scalar}(\mathbf{q},\omega)$ with

$$\Lambda^{even}_{scalar}(\mathbf{q},\omega) = \frac{1}{2\pi}\mathrm{Im}\int_k \left[\frac{z(\epsilon_{\mathbf{k}_+}+\epsilon_{\mathbf{k}_-})}{(z^2-E^2_{\mathbf{k}_+})(z^2-E^2_{\mathbf{k}_-})}\right]_{z=\omega-i\delta}. \tag{2.21}$$

Expressed in terms of the Bogoliubov coefficients $u_{\mathbf{k}}$ and $v_{\mathbf{k}}$, the expression under the integral in (2.21) is proportional to $(u_+u_- + v_+v_-)(u_+u_- - v_+v_-)$, and is, therefore, small for the nodal quasiparticles involved, $|\Lambda^{even}_{scalar}(\mathbf{q},\omega)| \ll |\Lambda^{odd}_{scalar}(\mathbf{q},\omega)|$. Thus, scattering off a weak scalar impurity contributes predominantly to odd-parity fluctuations in the density of states, $R^{odd}(\mathbf{q},V)$.

In a second example, consider scattering off a pair-breaking "Andreev" scatterer with the t-matrix given by $\hat{t}(\mathbf{q},\mathbf{k}) = T_1(\mathbf{q},\mathbf{k})\ \tau_1$. Here the change in the even and odd parts of the Fourier transformed tunneling density of states are $\delta\rho^{even(odd)}_A(\mathbf{q},\omega) = \Lambda^{even(odd)}_A(\mathbf{q},\omega)$ with

$$\Lambda^{even}_A(\mathbf{q},\omega) = \frac{1}{2\pi}\mathrm{Im}\int_k T_1(\mathbf{q},\mathbf{k})\ \left[\frac{z(\Delta_{\mathbf{k}_+}+\Delta_{\mathbf{k}_-})}{(z^2-E^2_{\mathbf{k}_+})(z^2-E^2_{\mathbf{k}_-})}\right]_{z=\omega-i\delta}, \tag{2.22}$$

$$\Lambda^{odd}_A(\mathbf{q},\omega) = \frac{1}{2\pi}\mathrm{Im}\int_k T_1(\mathbf{q},\mathbf{k})\ \left[\frac{\epsilon_{\mathbf{k}_+}\Delta_{\mathbf{k}_-}+\epsilon_{\mathbf{k}_-}\Delta_{\mathbf{k}_+}}{(z^2-E^2_{\mathbf{k}_+})(z^2-E^2_{\mathbf{k}_-})}\right]_{z=\omega-i\delta}. \tag{2.23}$$

In terms of $u_{\mathbf{k}}$ and $v_{\mathbf{k}}$, the expressions in square brackets in $\Lambda^{even}_A(\mathbf{q},\omega)$ and $\Lambda^{odd}_A(\mathbf{q},\omega)$ are proportional to $(u_+u_-+v_+v_-)(u_+v_-+v_+u_-)$ and $(u_+u_--v_+v_-)(u_+v_-+v_+u_-)$, respectively. For the nodal quasiparticles involved, the latter expression is substantially smaller than the former, $|\Lambda^{odd}_A(\mathbf{q},\omega)| \ll| \Lambda^{even}_A(\mathbf{q},\omega)|$. Thus, scattering off an Andreev scatterer gives rise to mainly even parity fluctuations in the density of states, $R^{even}(\mathbf{q},V)$.

We summarize the coherence factors arising in $R^{even}(\mathbf{q},V)$ and $R^{odd}(\mathbf{q},V)$ for some common scatterers in Table 2.1. The dominant contribution for a particular type of scatterer is given in bold.

From Table 2.1, we see that the odd correlator $R^{odd}(\mathbf{q}, V)$ is determined by a product of coherence factors associated with the charge operator and the scattering potential, while the even correlator $R^{even}(\mathbf{q}, V)$ is determined by a product of the coherence factors associated with the unit operator and the scattering potential.

2.6 Conductance ratio - measure of LDOS

An STM experiment measures the differential tunneling conductance $\frac{dI}{dV}(\mathbf{r}, V)$ at a location $\mathbf{r}$ and voltage V (66). In a simplified model of the tunneling,

$$\frac{dI}{dV}(\mathbf{r}, V) \propto \int_{-eV}^{0} d\omega[-f'(\omega - eV)] \int d\mathbf{r}_1 d\mathbf{r}_2 M(\mathbf{r}_1, \mathbf{r}) M^*(\mathbf{r}_2, \mathbf{r}) A(\mathbf{r}_2, \mathbf{r}_1, \omega), \tag{2.24}$$

where $A(\mathbf{r}_2, \mathbf{r}_1, \omega) = \frac{1}{\pi} Im\ G(\mathbf{r}_2, \mathbf{r}_1, \omega - i\delta)$ is the single electron spectral function and $f(\omega)$ is the Fermi function. Here $\mathbf{r}_1$, $\mathbf{r}_2$ and $\mathbf{r}$ are the two-dimensional coordinates of the incoming and outgoing electrons, and the position of the tip, respectively. $M(\mathbf{r}_1, \mathbf{r})$ is the spatially dependent tunneling matrix element, which includes contributions of the sample wave function around the tip.

Assuming that the tunneling matrix element is local, we write $M(\mathbf{r}_1, \mathbf{r}) = M(\mathbf{r})\delta^{(2)}(\mathbf{r}_1 - \mathbf{r})$, where $M(\mathbf{r})$ is a smooth function of position $\mathbf{r}$. In the low-temperature limit, when $T \to 0$, the derivative of the Fermi function is replaced by a delta-function, $-f'(\omega - eV) = \delta(\omega - eV)$. With these simplifications, we obtain

$$\frac{dI}{dV}(r, V) \propto |M(\mathbf{r})|^2 \rho(\mathbf{r}, V), \tag{2.25}$$

where $\rho(\mathbf{r}, V) = A(\mathbf{r}, \mathbf{r}, V)$ is the single-particle density of states. In the WKB approach the tunneling matrix element is given by $|M(\mathbf{r})|^2 = e^{-2\gamma(\mathbf{r})}$ with $\gamma(\mathbf{r}) = \int_0^{s(\mathbf{r})} dx \sqrt{\frac{2m\phi(\mathbf{r})}{\hbar^2}} = \frac{s(\mathbf{r})}{\hbar}\sqrt{2m\phi(\mathbf{r})}$, where $s(\mathbf{r})$ is the barrier width (tip-sample separation), $\phi(\mathbf{r})$ is the barrier height, which is a mixture of the work functions of the tip and the sample, m is the electron mass (66; 69). Thus, the tunneling conductance is a measure of the thermally smeared local density of states (LDOS) of the sample at the position of the tip.

Table 2.1: Coherence factors C(q) in $R^{even(odd)}(\mathbf{q}, V)$ for some common scatterers.

T-matrix	Scatterer	C(q) in $R^{even}(\mathbf{q}, V)$	C(q) in $R^{odd}(\mathbf{q}, V)$	Enhanced q_i
$\tau_{\mathbf{3}}$	Weak Scalar	$(uu' + vv')(uu' - vv')$	$(\mathbf{uu'} - \mathbf{vv'})^{\mathbf{2}}$	2,3,6,7
$\sigma \cdot \mathbf{m}$	Weak Mag.	0	0	None
i sgn ω $\hat{\mathbf{1}}$	Resonant	$(\mathbf{uu'} + \mathbf{vv'})^{\mathbf{2}}$	$(uu' + vv')(uu' - vv')$	1,4,5
$\tau_{\mathbf{1}}$	Andreev	$(\mathbf{uu'} + \mathbf{vv'})(\mathbf{uv'} + \mathbf{vu'})$	$(uu' - vv')(uv' + vu')$	1,4,5

To filter out the spatial variations in the tunneling matrix elements $M(\mathbf{r})$, originating from local variations in the barrier height ϕ and the tip-sample separation s, the conductance ratio is taken:

$$Z(r,V) = \frac{\frac{dI}{dV}(r,+V)}{\frac{dI}{dV}(r,-V)} = \frac{\rho(r,+V)}{\rho(r,-V)} = \frac{\rho_0(+V)+\delta\rho(r,+V)}{\rho_0(-V)+\delta\rho(r,-V)}. \tag{2.26}$$

For small fluctuations of the local density of states, $\delta\rho(r,\pm V) \ll \rho_0(\pm V)$, $Z(r,V)$ is given by a linear combination of positive and negative energy components of the tunneling density of states,

$$Z(r,V) \simeq Z_0(V)\ \Big[1+\frac{\delta\rho(r,+V)}{\rho_0(+V)} - \frac{\delta\rho(r,-V)}{\rho_0(-V)}\Big] \tag{2.27}$$

with $Z_0(V) \equiv \frac{\rho_0(+V)}{\rho_0(-V)}$. The Fourier transform of this quantity contains a single delta function term at $\mathbf{q}=0$ plus a diffuse background,

$$Z(\mathbf{q},V) = Z_0(V)(2\pi)^2\delta^2(\mathbf{q}) + Z_0(V)\ \Big[\frac{\delta\rho(\mathbf{q},+V)}{\rho_0(+V)} - \frac{\delta\rho(\mathbf{q},-V)}{\rho_0(-V)}\Big]. \tag{2.28}$$

Interference patterns produced by quasiparticle scattering off impurities are observed in the diffuse background described by the second term.

Clearly, linear response theory is only valid when the fluctuations in the local density of states are small compared with its average value, $\overline{\delta\rho(r,\pm V)^2} \ll \rho_0(\pm V)^2$. In the clean limit, this condition is satisfied at finite and sufficiently large bias voltages $|V|>0$. At zero bias voltage $V\to 0$, however, the fluctuations in the local density of states become larger than the vanishing density of states in the clean limit, $|\delta\rho(r,\pm V)| > \rho_0(\pm V)$, and linear response theory can no longer be applied.

At finite bias voltages, $|V|>0$, fluctuations in the conductance ratio $Z(\mathbf{q},V)$ are given by a sum of two terms, even and odd in the bias voltage:

$$Z(\mathbf{q},V)|_{\mathbf{q}\neq 0} = Z_0(V)\ \Big[\delta\rho^{even}(\mathbf{q},V)(\frac{1}{\rho_0(+V)} - \frac{1}{\rho_0(-V)}) + \delta\rho^{odd}(\mathbf{q},V)(\frac{1}{\rho_0(+V)} + \frac{1}{\rho_0(-V)})\Big], \tag{2.29}$$

where $\delta\rho^{even(odd)}(\mathbf{q},V) \equiv (\delta\rho(\mathbf{q},+V) \pm \delta\rho(\mathbf{q},-V))/2$.

Depending on the particle-hole symmetry properties of the sample-averaged tunneling density of states $\rho_0(V)$, one of these terms can dominate. For example, if, at the bias voltages used, the sample-averaged tunneling density of states $\rho_0(V)$ is approximately particle-hole symmetric, $\rho_0(-V) \approx \rho_0(+V) = \rho_0(V)$, then $Z(\mathbf{q},V)$ is dominated by the part of LDOS fluctuations that is odd in the bias voltage V,

$$Z(\mathbf{q},V)|_{\mathbf{q}\neq 0} \simeq Z_0(V)\ \frac{2}{\rho_0(V)}\delta\rho^{odd}(\mathbf{q},V). \tag{2.30}$$

In general, when we average over the impurity positions, the Fourier transformed fluctuations in the tunneling density of states, $\delta\rho(\mathbf{q},V)$, vanish. However, the variance in the density of states

fluctuations is non-zero and is given by the correlator

$$R(\mathbf{q}, V) \quad = \quad \overline{\delta\rho(\mathbf{q}, V)\delta\rho^*(-\mathbf{q}, V)}. \tag{2.31}$$

Defining

$$R^{even(odd)}(\mathbf{q}, V) \quad = \quad \overline{\delta\rho^{even(odd)}(\mathbf{q}, V)\delta\rho^{*even(odd)}(-\mathbf{q}, V)}, \tag{2.32}$$

we obtain that for $\mathbf{q} \neq 0$

$$|Z(\mathbf{q}, V)|^2 = \frac{4|Z_0(V)|^2}{\rho_0^2(V)} R^{odd}(\mathbf{q}, V). \tag{2.33}$$

2.7 Observation of coherence factor effects in QPI: coherence factors and the octet model

In high-Tc cuprates the quasiparticle interference (QPI) patterns, observed in the Fourier transformed tunneling conductance $dI(q, V)/dV \propto \rho(q, V)$, are dominated by a small set of wavevectors q_{1-7}, connecting the ends of the banana-shaped constant energy contours (70; 68; 73). This observation has been explained by the so-called "octet" model, which suggests that the interference patterns are produced by elastic scattering off random disorder between the regions of the Brillouin zone with the largest density of states, so that the scattering between the ends of the banana-shaped constant energy contours, where the joint density of states is sharply peaked, gives the dominant contribution to the quasiparticle interference patterns.

In essence, the octet model assumes that the fluctuations in the Fourier transformed tunneling density of states are given by the following convolution:

$$\delta\rho(\mathbf{q}, V) \propto \int_{\mathbf{k}} \rho(\mathbf{k}_+, \omega)\rho(\mathbf{k}_-, \omega).$$

While this assumption allows for a qualitative description, it is technically incorrect (98; 96), for the correct expression for change in the density of states involves the imaginary part of a product of Green's functions, rather than a product of the imaginary parts of the Green's function, as written above. In this section, we show that the fluctuations in the conductance ratio at wavevector $\mathbf{q}$, given by $Z(\mathbf{q}, V)$, are, nevertheless, related to the joint density of states via a Kramers-Kronig transformation, so that the spectra of the conductance ratio $Z(\mathbf{q}, V)$ can still be analyzed using the octet model.

As we have discussed, fluctuations in the density of states $\delta\rho(\mathbf{q}, V)$ are determined by scattering off impurity potentials and have the basic form (2.16). This quantity involves the imaginary part of a product of two Green's functions, and as it stands, it is not proportional to the joint

density of states. However, we can relate the two quantities by a Kramers-Kronig transformation, as we now show.

We write the Green's function as

$$G_{\mathbf{k}}(E-i\delta) = \int \frac{d\omega}{\pi} \frac{1}{E-\omega-i\delta} G''_{\mathbf{k}}(\omega - i\delta), \tag{2.34}$$

where $G''_{\mathbf{k}}(\omega - i\delta) = \frac{1}{2i}(G_{\mathbf{k}}(\omega - i\delta) - G_{\mathbf{k}}(\omega + i\delta))$. Substituting this form in (2.16), we obtain

$$\delta\rho^{odd}(\mathbf{q}, E) = \frac{1}{2\pi^2} \int_{\mathbf{k}} \mathrm{Tr}\Big[\tau_3 \int dE' \ \big[\frac{1}{E-E'} \sum_{\mathbf{k}} G''_{\mathbf{k}-}(E)\hat{t}(\mathbf{q},\mathbf{k})G''_{\mathbf{k}+}(E') - [E \leftrightarrow E']\big]\Big].$$

As we introduce the joint density of states,

$$J(\mathbf{q}, E, E') = \tfrac{1}{\pi^2} \textstyle\sum_{\mathbf{k}} Tr[\tau_3 G''_{\mathbf{k}-}(E)\hat{t}(\mathbf{q},\mathbf{k})G''_{\mathbf{k}+}(E')], \tag{2.35}$$

(2.35) becomes

$$\delta\rho^{odd}(\mathbf{q}, \omega) = \frac{1}{2} \int dE' \ \frac{1}{E-E'} [J(\mathbf{q}, E, E') + J(\mathbf{q}, E', E)]. \tag{2.36}$$

The Fourier transformed conductance ratio $Z(\mathbf{q}, E)$ given by (2.30) now becomes (for $\mathbf{q} \neq 0$)

$$Z(\mathbf{q}, E) = \tfrac{1}{\rho_0(E)} \textstyle\int dE' \ \tfrac{1}{E-E'} [J(\mathbf{q}, E, E') + J(\mathbf{q}, E', E)]. \tag{2.37}$$

Substituting the expression for the BCS Green's function (2.19) in (2.35), we obtain

$$\begin{aligned} J(\mathbf{q}, E, E') = \ & \tfrac{1}{4} \textstyle\sum_{\mathbf{k}} \tfrac{1}{E_{\mathbf{k}+}E_{\mathbf{k}-}} Tr[\tau_3(E + \epsilon_{\mathbf{k}-}\tau_3 + \Delta_{\mathbf{k}-}\tau_1)\hat{t}(\mathbf{q},\mathbf{k})(E' + \epsilon_{\mathbf{k}+}\tau_3 + \Delta_{\mathbf{k}+}\tau_1)] \cdot \\ \cdot \ & [\delta(E - E_{\mathbf{k}-}) - \delta(E + E_{\mathbf{k}-})][\delta(E' - E_{\mathbf{k}+}) - \delta(E' + E_{\mathbf{k}+})] \cdot sgnE \cdot sgnE', \end{aligned}$$

where $E_{\mathbf{k}_\pm} \equiv \sqrt{\epsilon^2_{\mathbf{k}_\pm} + \Delta^2_{\mathbf{k}_\pm}}$. Provided both the energies are positive, $E, E' > 0$, we obtain

$$J(\mathbf{q}, E, E') = \textstyle\sum_{\mathbf{k}_1,\mathbf{k}_2} C(\mathbf{k}_1, \mathbf{k}_2)\delta(E - E_{\mathbf{k}_1})\delta(E' - E_{\mathbf{k}_2})\delta^{(2)}(\mathbf{k}_1 - \mathbf{k}_2 - \mathbf{q}), \tag{2.38}$$

where the coherence factor is

$$C(\mathbf{k}_1, \mathbf{k}_2) \equiv \frac{1}{4} \frac{1}{E_{\mathbf{k}_1}E_{\mathbf{k}_2}} Tr[\tau_3(E + \epsilon_{\mathbf{k}_1}\tau_3 + \Delta_{\mathbf{k}_1}\tau_1)\hat{t}(\mathbf{k}_1, \mathbf{k}_2)(E' + \epsilon_{\mathbf{k}_2}\tau_3 + \Delta_{\mathbf{k}_2}\tau_1)]. \tag{2.39}$$

Now the fluctuations in the conductance ratio at wavevector $\mathbf{q}$ are given by:

$$Z(\mathbf{q}, E)|_{\mathbf{q}\neq 0} \propto \int \frac{dE'}{E-E'} \int d\mathbf{k}_1 d\mathbf{k}_2 C(\mathbf{k}_1, \mathbf{k}_2)\delta(E - E_{\mathbf{k}_1})\delta(E' - \beta E_{\mathbf{k}_2})\delta^{(2)}(\mathbf{k}_1 - \mathbf{k}_2 - \mathbf{q}).$$

Thus, the fluctuations in the conductance ratio $Z(\mathbf{q}, E)$ are determined by a Kramers-Kronig transform of the joint density of states with a well-defined coherence factor.

Conventionally, coherence factors appear in dissipative responses, such as (2.38). The appearance of a Kramers-Kronig transform reflects the fact that tunneling conductance is determined by the non-dissipative component of the scattering. The validity of the octet model

depends on the presence of sharp peaks in the joint density of states. We now argue that if the joint density of states contains sharp peaks at well-defined points in momentum space, then these peaks survive through the Kramers-Kronig procedure, so that they still appear in the conductance ratio $Z(\mathbf{q}, E)$ with a non-Lorentzian profile, but precisely the same coherence factors. We can illustrate this point both numerically and analytically. Figure 1 contrasts joint density of states with the Fourier transformed conductance ratio $Z(\mathbf{q}, E)$ for scattering off a weak scalar impurity, showing the appearance of the "octet" scattering wavevectors in both plots. Similar comparisons have been made by earlier authors (96; 98).

Let us now repeat this analysis analytically. Suppose $J(\mathbf{q}, E_1, E_2)$ (2.38) has a sharp peak at an octet $\mathbf{q}$ vector, $\mathbf{q} = \mathbf{q}_i$ $(i = 1 - 7)$, defined by the delta function $J(\mathbf{q}, E_1 = E, E_2 = E) = C_i \delta^{(2)}(\mathbf{q} - \mathbf{q}_i)$, where C_i is the energy-dependent coherence factor for the ith octet scattering process. When we vary the energy E_2 away from E, the position of the characteristic octet vector will drift according to

$$\mathbf{q}_i(E_1, E_2) = \mathbf{q}_i(E) - \nabla_{E_1}\mathbf{q}_i(E_1 - E) + \nabla_{E_2}\mathbf{q}_i(E_2 - E), \tag{2.40}$$

where $\nabla_{E_1}\mathbf{q}_i = \frac{1}{v_\Delta}\hat{\mathbf{n}}_1(i)$ and $\nabla_{E_2}\mathbf{q}_i = \frac{1}{v_\Delta}\hat{\mathbf{n}}_2(i)$ are directed along the initial and final quasiparticle velocities, and v_Δ is the quasiparticle group velocity. Carrying out the integral over E' in (2.40) we now obtain

$$\begin{aligned} Z(\mathbf{q}, E) &\propto \int dE' \, \frac{C_i}{E - E'}\Big[\delta(\mathbf{q} - \mathbf{q}_i(E) - \frac{\hat{n_2}}{v_\Delta}(E' - E)) + \delta(\mathbf{q} - \mathbf{q}_i(E) + \frac{\hat{n_1}}{v_\Delta}(E' - E))\Big] \\ &= C_i\Big[\frac{1}{(\mathbf{q} - \mathbf{q}_i)_{\parallel 1}}\delta\big((\mathbf{q} - \mathbf{q}_i)_{\perp 1}\big) - \frac{1}{(\mathbf{q} - \mathbf{q}_i)_{\parallel 2}}\delta\big((\mathbf{q} - \mathbf{q}_i)_{\perp 2}\big)\Big], \end{aligned} \tag{2.41}$$

where

$$(\mathbf{q} - \mathbf{q}_i)_{\parallel 1,2} = (\mathbf{q} - \mathbf{q}_i) \cdot \hat{\mathbf{n}}_{1,2}(i)$$

denotes the component of $(\mathbf{q} - \mathbf{q}_i)$ parallel to the initial/final quasiparticle velocity and

$$(\mathbf{q} - \mathbf{q}_i)_{\perp 1,2} = (\mathbf{q} - \mathbf{q}_i) \cdot [\hat{\mathbf{z}} \times \hat{\mathbf{n}}_{1,2}(i)]$$

denotes the component of $(\mathbf{q} - \mathbf{q}_i)$ *perpendicular* to the initial/final quasiparticle velocity, where $\hat{\mathbf{z}}$ is the normal to the plane. Thus, a single sharp peak in the joint density of states produces an enhanced dipolar distribution in the conductance ratio $Z(\mathbf{q}, E)$, with the axes of the dipoles aligned along the directions of the initial and final quasiparticle velocities. The above analysis can be further refined by considering the Lorentzian distribution of the quasiparticle interference peaks, with the same qualitative conclusions.

To summarize, the conductance ratio $Z(\mathbf{q}, E)$ is a spectral probe for fluctuations in the quasiparticle charge density in response to disorder. $Z(\mathbf{q}, E)$ is characterized by the joint

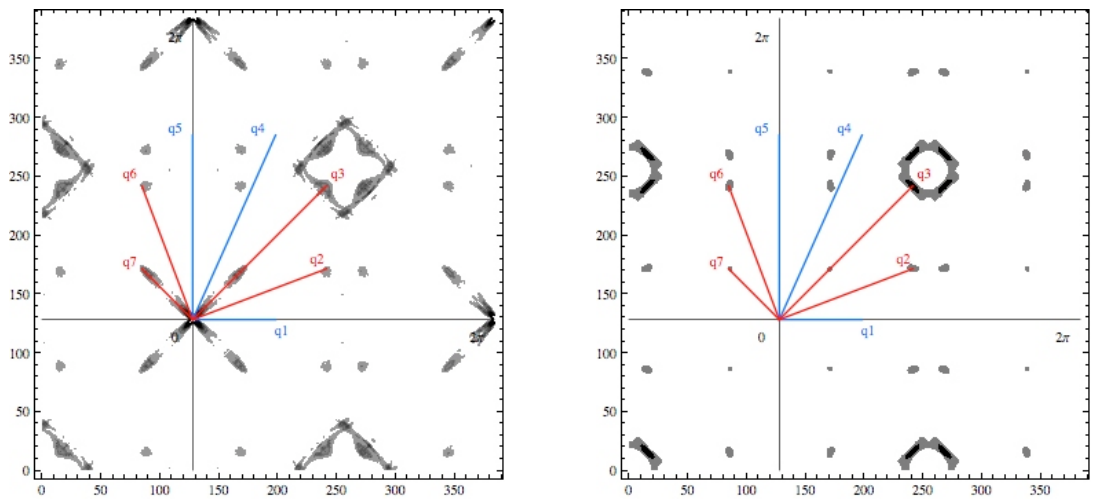

Figure 2.4: (Color online) Observation of coherence factor effects in the squared joint density of states $|J(\mathbf{q}, V, V)|^2$ and in the squared Fourier transformed conductance ratio $|Z(\mathbf{q}, V)|^2$. Figure (a) shows the squared joint density of states $|J(\mathbf{q}, V, V)|^2$ at the bias voltage $V = \Delta_0/2$, Figure (b) shows the squared Fourier transformed conductance ratio $|Z(\mathbf{q}, V)|^2$ produced by a weak scalar scattering potential $\hat{t}(\mathbf{q}) = \hat{\tau}_3$. Red lines label the positions of the sign-reversing q-vectors $q = q_{2,3,6,7}$, where weak scalar scattering is peaked. Blue lines label the positions of the sign-preserving q-vectors $q = q_{1,4,5}$, where weak scalar scattering is minimal.

coherence factors of charge (τ_3) and the scattering potential. Provided the original joint density of states is sharply peaked at the octet vectors $\mathbf{q}_i,\ i = 1 - 7$, the conductance ratio $Z(\mathbf{q}, E)$ is also peaked at the octet vectors $\mathbf{q}_i,\ i = 1 - 7$.

Chapter 3

Observation of coherence factor effects in a high-Tc cuprate using STM

In this chapter, we offer a qualitative interpretation of the recent scanning tunneling experiments by Hanaguri et al. (60) performed on an underdoped cuprate superconductor, calcium sodium oxychloride, $Ca_{2-x}Na_xCuO_2Cl_2$ (Na-CCOC), which have successfully observed coherence factor effects with Fourier Transform Scanning Tunneling Spectroscopy (FT-STS) in a magnetic field.

3.1 Introduction

3.1.1 Superconductors in a magnetic field

In compliance with the Meissner effect, illustrated in Figure 1.1(b), a weak magnetic field only penetrates a superconductor within a short distance, called the penetration depth λ (77). A rather strong external magnetic field can, however, destroy the superconductivity by driving a phase transition into the normal state. Next we discuss how this phase transition takes place.

Macroscopic properties of superconductors were explained by a phenomenological Ginzburg-Landau theory (7), in 1950. Ginzburg-Landau theory suggested that the transition from the normal to the superconducting state involves a second order phase transition, and is associated with a formation of an order parameter Δ. Ginzburg-Landau theory introduces two characteristic length scales: the superconducting coherence length ξ, and a penetration depth λ.

Abrikosov (8), building on the Ginzburg-Landau theory, predicted the existence of two types of superconductors: type I and type II, classified according to their behavior in an external magnetic field. At low magnetic fields, both types exhibit the Meissner effect, expelling magnetic flux from the sample. As the magnetic field grows, type I superconductors lose superconductivity abruptly in a first order phase transition at a critical field H_c, while type II superconductors start to accomodate magnetic field, which enters the sample in the form of flux lines when the magnetic field exceeds the first critical field $H > H_{c1}$, as shown in Figure 3.1(a). Once

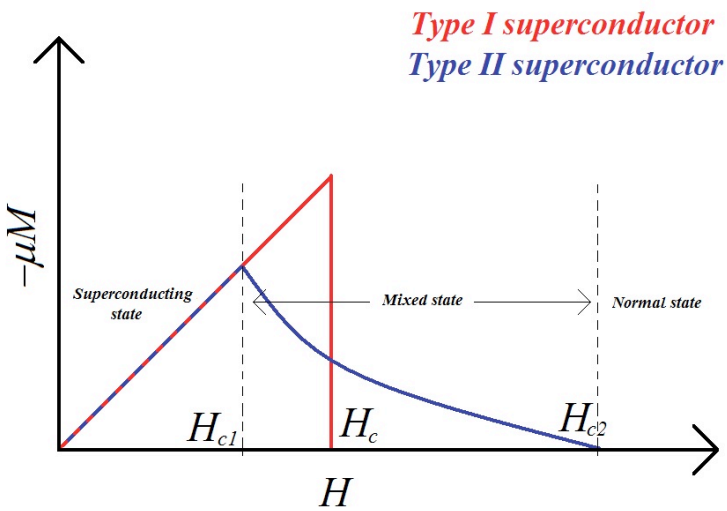

(a)

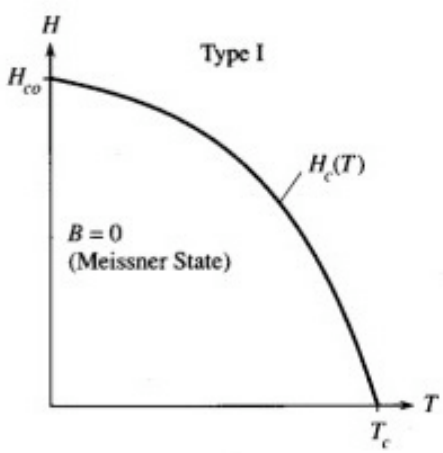

(b)

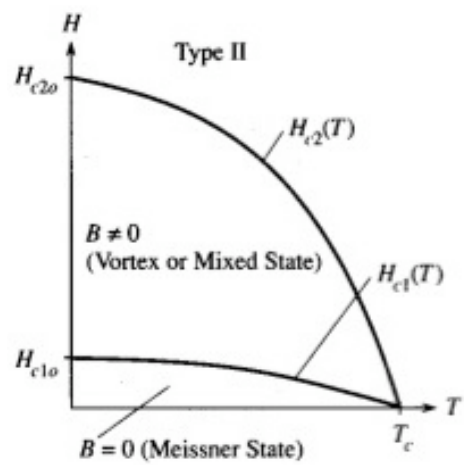

(c)

Figure 3.1: Two types of superconductors, classified by their behavior in a strong external magnetic field. Figure (a) displays the magnetization of type I and type II superconductors as a function of an external magnetic field H. Figure (b) displays the phase diagram of a type I superconductor, which transforms into a normal metal via a first-order phase transition in an external magnetic field. Figure (c) displays the phase diagram of a type II superconductor, which gets gradually penetrated by a magnetic field exceeding H_{c1}, and transforms into a normal metal via a second-order phase transition once the magnetic field reaches H_{c2}. Source: wikipedia.

the magnetic field reaches the second critical field $H_{c2} \gg H_{c1}$, it completely destroys the superconductivity in type II superconductors via a second order phase transition. The resulting phase diagrams are displayed in Figures 3.1(b), 3.1(c).

In terms of Ginzburg-Landau parameter $\kappa = \frac{\lambda}{\xi}$, type I superconductors have a large coherence length, exceeding the penetration depth, $\kappa < 1/\sqrt{2}$, whereas type II superconductors have $\kappa > 1/\sqrt{2}$. Elemental metals, such as aluminum and tin, are type I superconductors, with large coherence length of order 100-1000 nm, $\xi \sim 100 - 1000$ nm. Copper oxide superconductors, by contrast, are extreme type II superconductors with a short coherence length of order 1-10 nm, $\xi \sim 1 - 10$ nm.

At intermediate magnetic fields, for $H_{c1} < B < H_{c2}$, a type II superconductor contains flux lines, known as vortices. The radius of a vortex is given by the coherence length $\xi = v_F/\Delta$. Because inside a vortex, an s-wave BCS superconductor is in the normal state, the entire material is said to be in the mixed state.

3.1.2 Coherence factors in a high-Tc cuprate probed by quasiparticle scattering off vortices

Coherence factors are a hallmark of superconductivity as a pair-condensation phenomenon. When electrons pair, quasiparticles develop an acute sensitivity to different types of scattering potential, described by the appearance of coherence factors in the scattering amplitudes. While the effects of coherence factors are well established in isotropic superconductors, they are much harder to detect in their anisotropic counterparts, such as high-Tc cuprates. A new approach by Hanaguri et al. (60) highlights the momentum-dependent coherence factors in $Ca_{2-x}Na_xCuO_2Cl_2$. Using Fourier-transform scanning tunnelling spectroscopy to detect quasiparticle interference effects, the experiments reveal a magnetic field dependence in quasiparticle scattering with a sensitivity to the sign of the anisotropic gap. This result can be understood in terms of d-wave coherence factors and it exposes the role of vortices as quasiparticle-scattering centers. A magnetic field gives rise to an enlarged gapless region around the gap nodes.

Superconductivity is characterized by macroscopic phase coherence, as exemplified by the development of a complex order parameter. In this respect, superconductors are similar to bosonic superfluids, such as He-4 and many phenomenological features are common to both, such as vortex quantization and the Josephson effect (78). However, superconductors are microscopically distinct from bosonic superfluids, for whereas bosons individually condense, electrons condense as Cooper pairs. The internal structure of the condensed pairs strongly influences the

properties of quasiparticle excitations, enforcing coherence between two quasiparticle scattering processes, $\mathbf{k}_i \rightarrow \mathbf{k}_f$ and $-\mathbf{k}_f \rightarrow -\mathbf{k}_i$. ($\mathbf{k}_i$ and $\mathbf{k}_f$ denote initial and final state momenta, respectively.) This manifests itself as a coherence factor $C(\mathbf{k}_i, \mathbf{k}_f)$ in the scattering matrix element, which reflects the anisotropy of the superconducting gap and the time-reversal symmetry of the scattering potential (79). Studies of coherence factors should therefore provide insight into the nature of electron pairing and quasiparticle scattering processes in unconventional superconductors.

In s-wave superconductors, the effect of coherence factors is manifested in the temperature dependence of various measurable quantities associated with quasiparticle scattering. For example, the nuclear-spin relaxation rate exhibits an enhancement just below the superconducting transition temperature T_c, called the Hebel-Slichter peak (13), which is a consequence of coherence factors. In unconventional superconductors, however, the effect of coherence factors is suppressed by the strong momentum k dependence of the anisotropic gap (80).

Hanaguri et al. (60) have proposed a new technique to highlight the k-dependent coherence factors in anisotropic superconductors by introducing vortices as controllable scatterers. The vortices induced by magnetic field B will generate extra quasiparticle scatterings around them in which coherence factor effects can be detected. Quasiparticle scattering can be examined through the Fourier analysis of quasiparticle interference (QPI) patterns imaged by spectroscopic-imaging scanning tunneling microscopy (SI-STM) (61; 70; 71). Hanaguri et al. have performed a B-dependent QPI study in a high-Tc cuprate $Ca_{2-x}Na_xCuO_2Cl_2$. The B-dependence and spatial variation of QPI intensities can be naturally understood as a manifestation of the d-wave coherence factor and establishes vortices as scattering centers with a particular momentum selectivity. A B-induced change in the superconducting gap dispersion, which results an enlarged gapless region near the superconducting gap node, is also revealed by the measurements.

3.2 Quasiparticle interference in high-Tc cuprates

First we review the QPI effect. In general, QPI is produced by elastic scattering which mixes the quasiparticle states along the contour of constant energy in momentum k space. This gives rise to standing waves of particular scattering wavevectors $\mathbf{q} = \mathbf{k}_f - \mathbf{k}_i$. To image these standing waves Hanaguri et al. have used SI-STM to map the tunneling conductance $g(\mathbf{r}, E) = dI/dV(\mathbf{r}, E)$, where I and V are the tunneling current and bias voltage, respectively. $g(\mathbf{r}, E)$ is a measure of the local density of states (DOS) at location $\mathbf{r}$ and energy E. The amplitude and $\mathbf{q}$ of the

standing wave can be accurately determined from the Fourier transform of $g(\mathbf{r}, E)$, $g(\mathbf{q}, E)$. $g(\mathbf{q}, E)$ is proportional to the scattering probability (63), given by Fermi's "golden rule",

$$g(\mathbf{q}, E) \propto \int\int V(\mathbf{k}_i, \mathbf{k}_f)^2 J(\mathbf{k}_i, \mathbf{k}_f)\delta(\mathbf{q} - (\mathbf{k}_f - \mathbf{k}_i))\delta(E(\mathbf{q}) - E(\mathbf{k}_i))\delta(E(\mathbf{q}) - E(\mathbf{k}_f))\ d\mathbf{k}_i\ d\mathbf{k}_f,$$

where $V(\mathbf{k}_i, \mathbf{k}_f)$ is a k-dependent scattering matrix element and $J(\mathbf{k}_i, \mathbf{k}_f, E)$ denotes a joint DOS. The dispersion of quasiparticles in k space, E(k), can be experimentally determined from the E dependence of $\mathbf{q}$. Indeed, in conventional metals and semiconductors, QPI has been widely used to determine the surface band structures (81; 82; 83).

QPI patterns in the high-Tc cuprates are dominated by a small set of q's given by the "octet" model (71). The low-energy excitations in the superconducting states are Bogoliubov quasiparticles with a dispersion $E(\mathbf{k}) = \sqrt{\varepsilon(\mathbf{k})^2 + \Delta(\mathbf{k})^2}$, where $\varepsilon(\mathbf{k})$ and $\Delta(\mathbf{k})$ are dispersion relations of normal-state band and superconducting gap, respectively (78; 79). In high-Tc cuprates, the superconducting gap has $d_{x^2-y^2}$-wave symmetry (84) and vanishes along the $(\pm\pi, \pm\pi)$ directions (diagonals of the unit cell). The dispersion $E(\mathbf{k})$ gives rise to four "banana-shaped" contours of constant energy, as shown in Figure 3.2(a). The amplitudes of the standing waves become large if the momentum transfer $\mathbf{q}$ connects the ends of the "bananas", where the joint DOS is the largest. This determines the locations of seven distinct scattering vectors ($\mathbf{q}_i$ $(i = 1 - 7)$ in Figure 3.2(a)) in q space. The quasiparticle states located at the ends of the bananas lie on the normal state Fermi surface (red curves in Figure 3.2(a)), where $\varepsilon(\mathbf{k}) = 0$, and the energy $E(\mathbf{k}) = |\Delta(\mathbf{k})|$ at these points corresponds to the magnitude of superconducting gap.

3.3 Coherence factor effects in quasiparticle interference

In the superconducting state, the coherence of quasiparticle scattering induced by pair formation causes the scattering probability to acquire an additional k dependence determined by the coherence factor $C(\mathbf{k}_i, \mathbf{k}_f)$ (79). $C(\mathbf{k}_i, \mathbf{k}_f)$ is given by a combination of Bogoliubov coefficients $u_\mathbf{k} = sgn(\Delta(\mathbf{k}))\sqrt{(1 + \varepsilon(\mathbf{k})/E(\mathbf{k}))/2}$ and $v_\mathbf{k} = \sqrt{1 - u_\mathbf{k}^2}$. The detailed form of $C(\mathbf{k}_i, \mathbf{k}_f)$ depends on the nature of the scatterer as summarized in Table 2.1 (69; 73; 79; 99; 100; 101). For a scalar potential, which is even under time reversal $C(\mathbf{k}_i, \mathbf{k}_f) = (u_{\mathbf{k}_i} u_{\mathbf{k}_f} - v_{\mathbf{k}_i} v_{\mathbf{k}_f})^2$, for a magnetic scattering potential, which is odd under time reversal $C(\mathbf{k}_i, \mathbf{k}_f) = (u_{\mathbf{k}_i} u_{\mathbf{k}_f} + v_{\mathbf{k}_i} v_{\mathbf{k}_f})^2$. Scattering off inhomogeneities in the superconducting gap amplitude, which is a kind of inhomogeneous Andreev reflection process that converts electrons into holes as they are scattered, gives rise to the coherence factor $C(\mathbf{k}_i, \mathbf{k}_f) = (u_{\mathbf{k}_i} v_{\mathbf{k}_f} + v_{\mathbf{k}_i} u_{\mathbf{k}_f})(u_{\mathbf{k}_i} u_{\mathbf{k}_f} + v_{\mathbf{k}_i} v_{\mathbf{k}_f}) \propto \Delta(\mathbf{k}_i) + \Delta(\mathbf{k}_f)$. As shown in Figures 3.2(b) and 3.2(c), $u_\mathbf{k}$ changes its sign in the same way as $\Delta(\mathbf{k})$ while

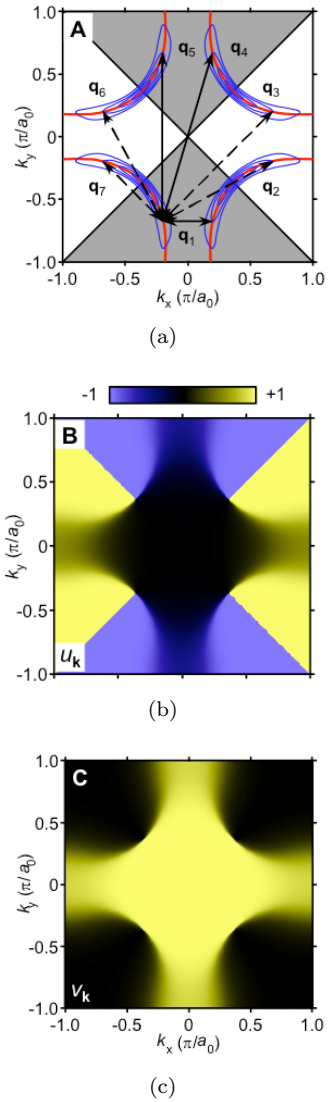

Figure 3.2: Schematic representation of k-space electronic states in a high-Tc cuprate. (a): Normal-state Fermi surface (red curves) and contours of constant energy for Bogoliubov quasiparticles (blue curves) in the 1st Brillouin zone. White and shaded areas represent k-space regions with opposite signs of d-wave superconducting gap. Arrows denote scattering q vectors responsible for QPI patterns. They are classified into sign-preserving and sign-reversing vectors indicated by solid and broken arrows, respectively, according to the relative signs of superconducting gap between initial and final states. These two kinds of vectors are associated with different coherence factors as summarized in Table 2.1. (b) and (c): Bogoliubov coefficients $u_{\mathbf{k}}$ (b) and $v_{\mathbf{k}}$ (c) are mapped in k space. Note that $u_{\mathbf{k}}$ changes its sign according to that of superconducting gap, while $v_{\mathbf{k}}$ is always positive.

$v_{\mathbf{k}}$ is always positive. This leads to a systematic "extinction rule" for $\mathbf{q}_i$'s which depends on the nature of the scatterer. In the case of weak scalar potential scattering, $C(\mathbf{k}_i, \mathbf{k}_f) \sim 0$ for those $\mathbf{q}_i$ which preserve the sign of superconducting gap $\Delta(\mathbf{k})$, namely $\mathbf{q}_1$, $\mathbf{q}_4$ and $\mathbf{q}_5$. By contrast, for scattering off magnetic impurities or gap inhomogeneities, $C(\mathbf{k}_i, \mathbf{k}_f) \sim 0$ for those $\mathbf{q}_i$ which reverse the sign of $\Delta(\mathbf{k})$. Thus, depending on the type of disorder, sign-reversing, or sign-preserving scatterings will dominate (69; 99; 100; 101; 73). In this way, QPI patterns can shed light onto the underlying nature of the quasiparticle scattering processes. However, in experiments carried out to date (61; 70; 71), each of the $\mathbf{q}_i$'s has featured with comparable intensity, which indicates that more than one kind of scatterers is present in the samples, hiding the underlying effects of $C(\mathbf{k}_i, \mathbf{k}_f)$.

Introduction of vortices by applying a magnetic field B provides system with scatterers with definite $\mathbf{q}$ selectivity. The phase of the superconducting gap precesses by 2π about each vortex, where the amplitude of the gap vanishes at its core. Both the phase gradient, proportional to the superfluid velocity, and the inhomogeneity in the superconducting gap amplitude, induced by the vortex core, can scatter quasiparticles. The inhomogeneous superflow about a vortex produces Doppler-shift scattering (85) which is odd under time reversal with $C(\mathbf{k}_i, \mathbf{k}_f) = (u_i u_f + v_i v_f)^2$ like magnetic impurities. The spatial inhomogeneity in the superconducting gap amplitude causes inhomogeneous Andreev scattering with $C(\mathbf{k}_i, \mathbf{k}_f) = (u_i v_f + v_i u_f)(u_i u_f + v_i v_f)$. It should be noted that both of these scatterers selectively activate the sign-preserving q points. Therefore, the effect of $C(\mathbf{k}_i, \mathbf{k}_f)$ and the nature of quasiparticle scattering off vortices can be revealed through the $\mathbf{q}$-dependence of the B-induced change of QPI.

3.4 Phase-sensitivity of quasiparticle interference in a magnetic field

Hanaguri et al. performed SI-STM measurements in a magnetic field on nearly optimally-doped $Ca_{2-x}Na_xCuO_2Cl_2$ ($x \sim 0.14$, $T_c \sim 28$ K) single crystals (61; 63) using a low-temperature ultrahigh-vacuum scanning tunneling microscope (86; 87). Samples were cleaved in situ at 77 K and transferred to the microscope maintained at a temperature below 10 K. In order to make the vortex distribution inside the sample uniform, magnetic field up to 11 T was applied along the c axis at 5 K, where magnetization measurements confirmed that vortex pinning was negligibly small. Then, the samples were field-cooled down to 1.6 K where all the data were collected. At 1.6 K, pinned vortices can be observed as shown in Figures 3.3(a), 3.3(b), and 3.3(c). All the spectroscopic data were taken in the same field of view simultaneously with atomic-resolution topographic images.

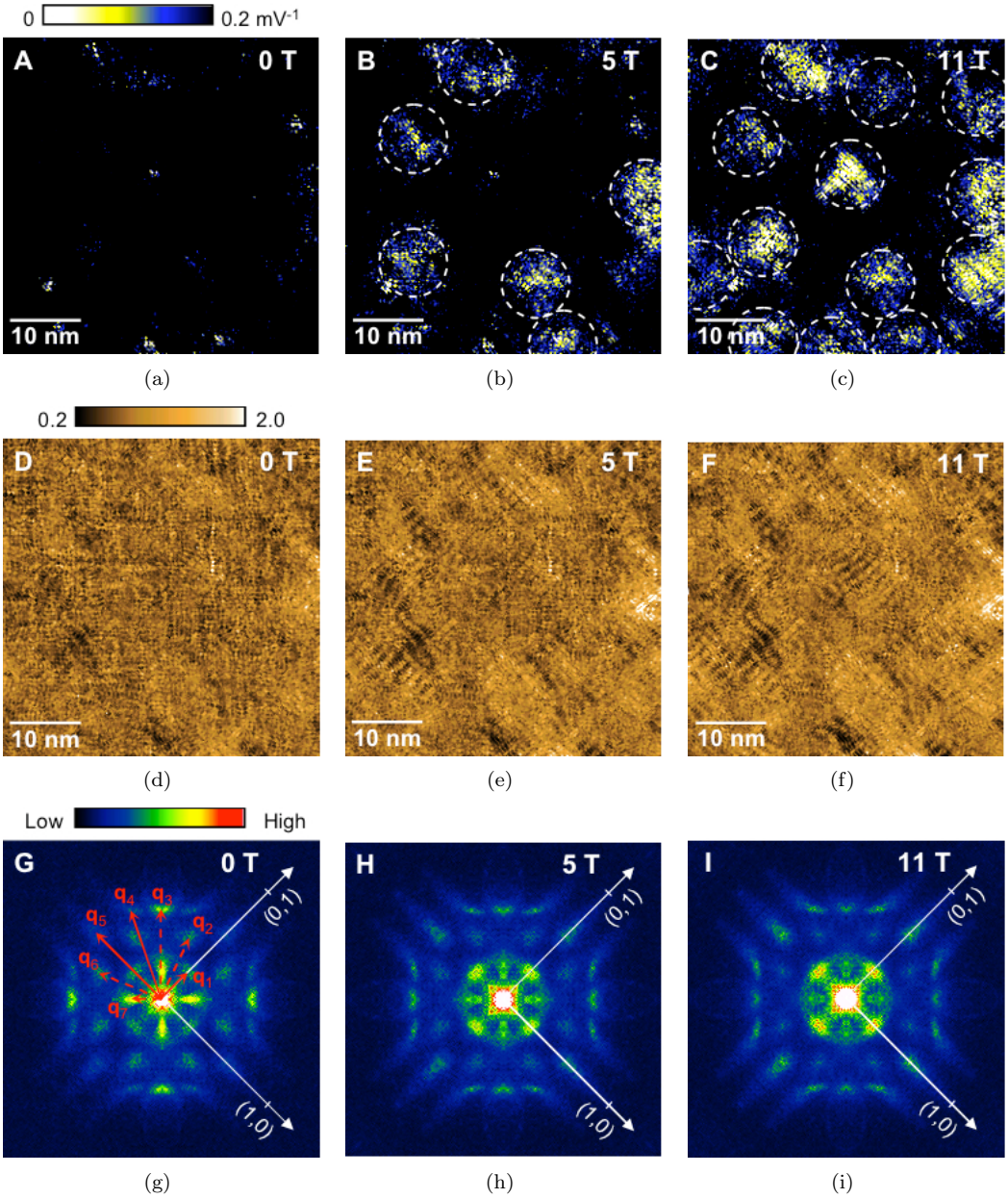

Figure 3.3: Imaging vortices and QPI patterns in $Ca_{2-x}Na_xCuO_2Cl_2$ ($x \sim 0.14$, T_c 28 K) at different magnetic fields. All the data were collected with a set-up condition of sample bias voltage $V_s = -100$ mV and tunneling current $I_t = 100$ pA. (a)-(c): Vortices imaged by mapping a function at $E = 4.4$ meV. If there is a gap in the spectrum $g(\mathbf{r}, E)$, the function $s(\mathbf{r}, E)$ below the gap energy takes larger value as gap structure becomes deeper, while it is almost zero if $g(\mathbf{r}, E)$ is structureless. Vortices are imaged as shallower-gap regions (smaller $s(\mathbf{r}, E)$) shown in brighter color. Broken circles are guides to the eye. (d)-(f): Real-space QPI patterns at $E = 4.4$ meV imaged by mapping the conductance-ratio $Z(\mathbf{r}, E)$. (g)-(i) $|Z(\mathbf{q}, E)|$ obtained by Fourier transforming $Z(\mathbf{r}, E)$ shown in (d)-(f). To enhance the signal-to-noise ratio, each $|Z(\mathbf{q}, E)|$ map is averaged by folding it so as to superpose all the crystallographically equivalent q positions. Arrows in (g) correspond to those in Figure 3.2(a).

In $Ca_{2-x}Na_xCuO_2Cl_2$, the raw $g(\mathbf{r}, E)$ data are dominated by "checkerboard" modulations (87) which mask the underlying QPI signal. As reported earlier (61), the QPI signal is enhanced by taking the ratio $Z(\mathbf{r}, E)$, $Z(\mathbf{r}, E) \equiv g(\mathbf{r}, E)/g(\mathbf{r}, -E)$. This procedure almost completely suppresses the checkerboard signal. It has an additional advantage of eliminating extrinsic effects associated with the scanning feedback loop and thus $Z(\mathbf{r}, E)$ faithfully represents the local-DOS ratio (61; 62). Figures 3.3(d) and 3.3(g) show the zero-field $Z(\mathbf{r}, E = 4.4\ meV)$ and its Fourier transform $—Z(\mathbf{q}, E = 4.4\ meV)|$, displaying the full set of discrete **q**-points expected in the octet model. These discrete q-points disperse with E in a fashion consistent with a d-wave superconducting gap up to $E \sim 15$ meV, which marks an upper limit for the detection of well-defined Bogoliubov quasiparticles (61) (see Figure 3.6).

When Hanaguri et al. repeated the measurements at B = 5 T and 11 T, they observed a remarkable B dependence in the intensities of the QPI patterns. The B dependence of $Z(\mathbf{r}, E)$ is shown in Figures 3.3(d), 3.3(e) and 3.3(f). The corresponding Fourier transformed data, displayed in Figures 3.3(g), 3.3(h) and 3.3(i), show that magnetic field does not induce additional **q** vectors and the positions of the peaks in $|Z(q, E)|$ are only weakly B dependent. By contrast, there is a significant B dependence in the intensities of the peaks. Depending on $\mathbf{q}_i$, intensity of peak is either enhanced or suppressed.

To explore the details of the B-induced intensity variations, Hanaguri et al. subtracted the zero-field data $|Z(\mathbf{q}, E, B = 0)|$ from $|Z(\mathbf{q}, E, B)|$. The corresponding difference maps are shown in Figure 3.4(a) for $B = 11$ T. It is clear that we can classify the q-points into two groups: for $\mathbf{q}_1$, $\mathbf{q}_4$, and $\mathbf{q}_5$ the intensity is field-enhanced, while for $\mathbf{q}_2$, $\mathbf{q}_3$, $\mathbf{q}_6$, and $\mathbf{q}_7$ the intensity is depressed. These two groups are nothing but the sign-preserving and sign-reversing **q**-points discussed earlier, and their selective enhancement and suppression imply the activation of coherence factors $C(\mathbf{k}_i, \mathbf{k}_f)$ induced by vortices.

The spatial resolution of SI-STM allows to spatially resolve the location of the momentum-selective enhancement and suppression of the QPI signal to examine its relationship with the location of the vortices. For this purpose, Hanaguri et al. restricted the field of view to the vicinity of vortices (as indicated by the "vortex region" inside the blue lines in Figure 3.4(b)) or to regions far from vortices (as indicated by the "matrix region" inside the red lines in Figure 3.4(b)), and performed Fourier analyses separately for each region (see Figure 3.7). As shown in Figure 3.4(c) and 3.4(d), the enhanced sign-preserving QPI signals are concentrated in the "vortex region", indicating that this signal is associated with coherent scattering effects induced by vortices. By contrast, the suppressed sign-reversing QPI signals is distributed throughout the "matrix region" far from the vortices, and must be associated with the superflow surrounding

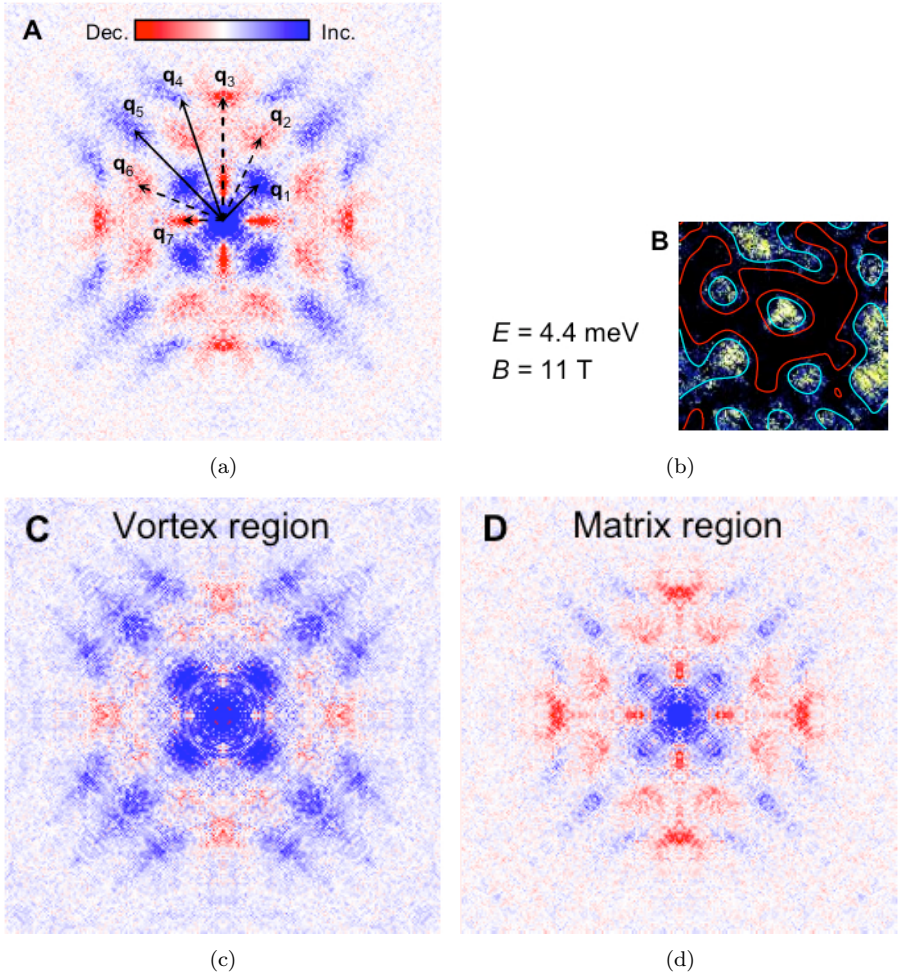

(a) (b)

(c) (d)

Figure 3.4: Magnetic-field-induced weight transfer in $|Z(\mathbf{q}, E)|$ at E = 4.4 meV. (a): The difference maps $|Z(\mathbf{q}, E, B)| - |Z(\mathbf{q}, E, B = 0)|$ for B = 11 T, namely, the difference between Figure 3.3(i) and Figure 3.3(g). Intensities of sign-preserving $\mathbf{q}$-points are field-enhanced while those of sign-reversing ones are field-suppressed. (b): Vortex image reproduced from Figure 3.3(c) showing the restricted field of views. Blue and Red lines surround vortex and matrix regions, respectively (see Figure 3.7). Magnetic-field-induced weight transfers are deduced separately for vortex and matrix regions as shown in (c) and (d), respectively. Intensities are normalized according to the area. Enhancement of sign-preserving scatterings at $\mathbf{q}_1$, $\mathbf{q}_4$, and $\mathbf{q}_5$ is remarkable near the vortices while it is weak in the matrix region.

the vortices.

We note as an aside that the enhanced sign-preserving $\mathbf{q}$ points q_1 and q_5 are very close to those wavevectors which characterize the "checkerboard" electronic modulation observed in the vicinity of vortices in $Bi_2Sr_2CaCu_2O_y$ (88; 89). Various charge and spin density wave scenarios have been advanced to account for the vortex "checkerboard" modulation (88; 89). In such scenarios, the characteristic wavevector of the scattering is not expected to disperse with energy. However, in our data the field-enhanced QPI intensities at these $\mathbf{q}$-points do disperse with energy (see Figure 3.6), so the electronic-order scenario does not appear to apply, at least in its simplest form. Further studies of the relation between QPI and the vortex "checkerboard" are needed to elucidate the electronic structure of vortices in high-Tc cuprates.

The reduction of the scattering at the sign-reversing vectors $\mathbf{q}_2$, $\mathbf{q}_3$, $\mathbf{q}_6$, and $\mathbf{q}_7$ in the matrix region can be accounted for in terms of the Doppler shift of quasiparticle energies induced by the superflow around vortices (85). The Doppler shift in the quasiparticle energies deforms the banana-shaped contours of constant energy by an amount proportional to the superfluid velocity. This has the effect of smearing the quasiparticle interference signals in momentum space, reducing their peak amplitude. The coherence factors of the Doppler shift suppression are those of the underlying scattering centers. Thus the reduction of sign-reversing scattering intensity can be accounted for in terms of a smearing of scattering off a dominant background of scalar scattering centers.

Finally, one can examine the B dependence of Fermi surface topology and superconducting gap dispersion $\Delta(\mathbf{k})$ by analyzing the E dependence of $|Z(\mathbf{q}, E, B)|$. As shown in Figure 3.5(a), the Fermi surface displays no measurable B dependence up to 11 T as expected, since the corresponding Zeeman energy to B is negligibly small (< 1 meV), compared with the hopping amplitude (~ 0.1 eV). On the other hand, $\Delta(\mathbf{k})$ shows a small but distinct field dependence as shown in Figure 3.5(b). At $B = 0$ T, a linear extrapolation of $\Delta(\mathbf{k})$ from high E does not intercept the node at $\theta_{\mathbf{k}} = 45\,^{\circ}$, where $\theta_{\mathbf{k}}$ is a Fermi surface angle around (π, π), and there is an apparent "gapless" region around the node. This may mean that $\Delta(\mathbf{k})$ includes a higher order harmonic such as $cos(6\theta_{\mathbf{k}})$ (91) or alternatively, that $\Delta(\mathbf{k})$ actually vanishes in a finite region around the node due to inelastic scattering (92). This "gapless" region expands in B, indicating that zero-energy quasiparticles are generated by introducing vortices. In accord with this, the DOS at the Fermi energy E_F, given by the average value of $g(\mathbf{r}, E = 0)$ increases as shown in Figure 3.5(c). The averaged $g(\mathbf{r}, E_F)$ well follow the $B\ log\ B$ behavior (90) expected in a dirty d-wave superconductor (Figure 3.5(d)). These results provide a spectroscopic basis for the field-induced DOS observed by specific heat (93) and nuclear magnetic resonance (94) measurements

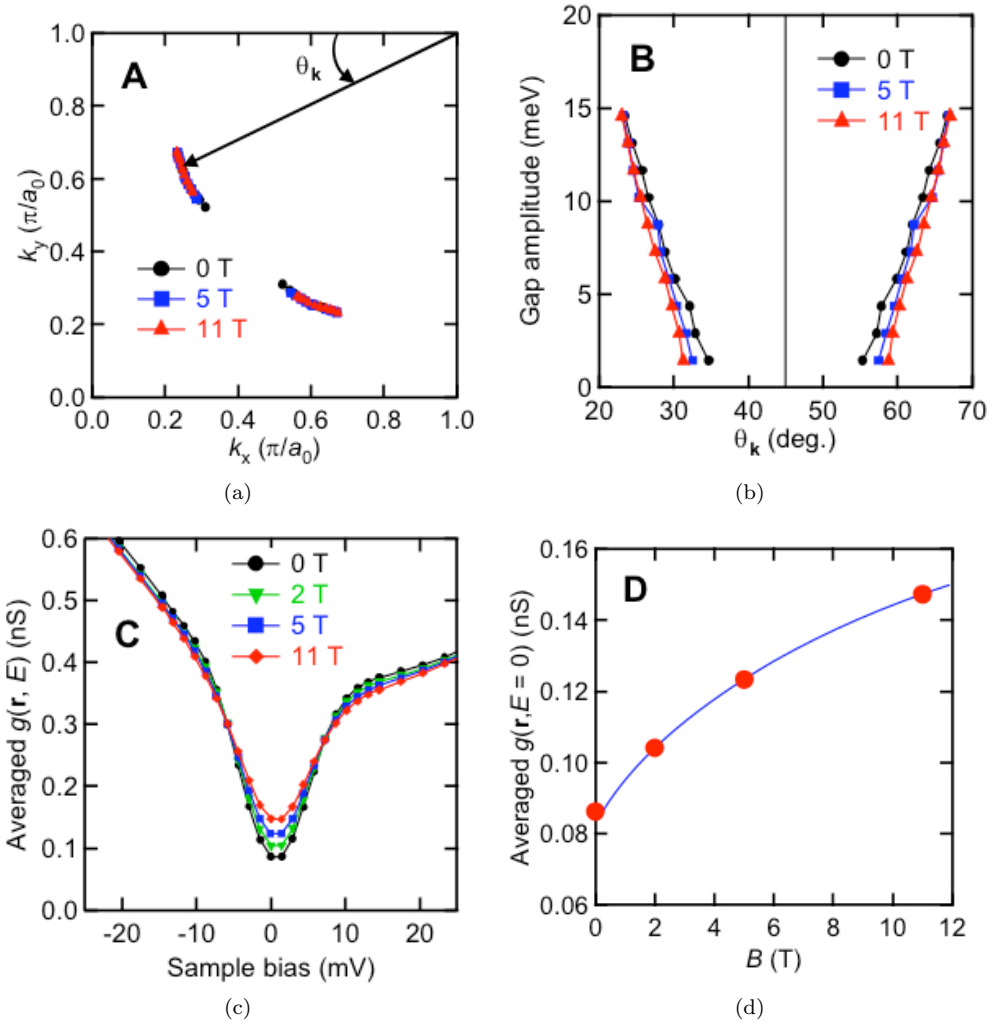

Figure 3.5: Magnetic field B effects on the electronic states of in $Ca_{2-x}Na_xCuO_2Cl_2$ ($x \sim 0.14$, $T_c \sim 28$ K). (a): Loci of octet ends of contour of constant energy at different B representing the underlying Fermi surface. Four independent $q_4(E) = (\pm 2k_x(E), 2k_y(E)), (2k_y(E), \pm 2k_x(E))$ were used for analysis. No measurable field-induced change is found in th e Fermi surface. (b): B-induced renormalization of the d-wave superconducting gap dispersion. B enlarges the apparent gapless region around the gap node, while dispersion at higher energy is relatively insensitive to B. (c): Tunneling spectra averaged over the field of view. Gap-like feature below about 10 meV gets shallower and DOS at E_F increases with increasing B. Spectrum at 2 T was averaged in the slightly different field of view for other fields. (d): The B dependence of spatially averaged $g(\mathbf{r}, E_F)$. Thin blue line denotes $B\ log\ B$ behavior expected in a dirty d-wave superconductor.

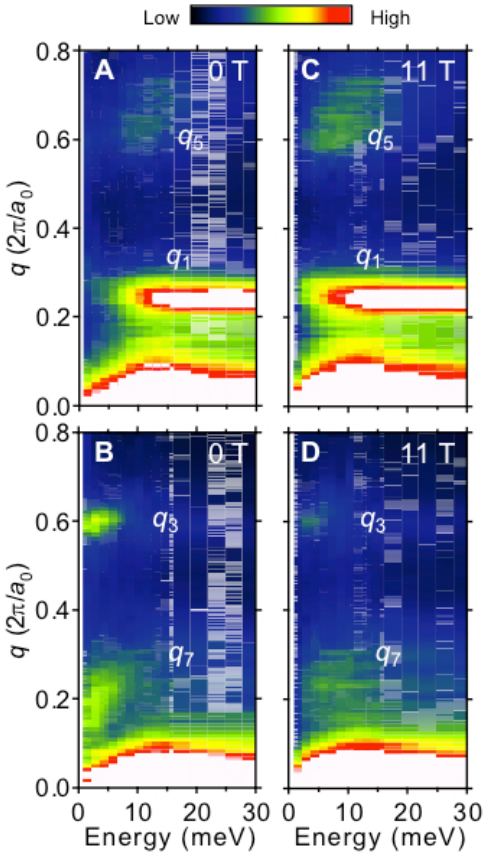

Figure 3.6: Energy dependence of QPI intensities obtained by taking linecuts from from $|Z(\mathbf{q}, E)|$ at various E along specific q directions. Color scale is set to the same range for Figures 3.3(g)-3.3(i). (a) and (b): Linecuts along $(0,0)-(0,2\pi/a_0)$ and $(0,0)-(2\pi/a_0, 2\pi/a_0)$, respectively, at $B = 0$ T. Dispersing q-vectors are seen below about 15 meV. Although intense $\mathbf{q}_1$ peak still exists above this energy, the peak stops dispersing. Other q peaks diminish. (c) and (d): Same linecuts at $B = 11$ T. It is clear that intensities of $\mathbf{q}_1$ and $\mathbf{q}_5$ peaks are enhanced while those of $\mathbf{q}_3$ and $\mathbf{q}_7$ peaks are suppressed. Note that B-enhanced signals show clear energy dispersion.

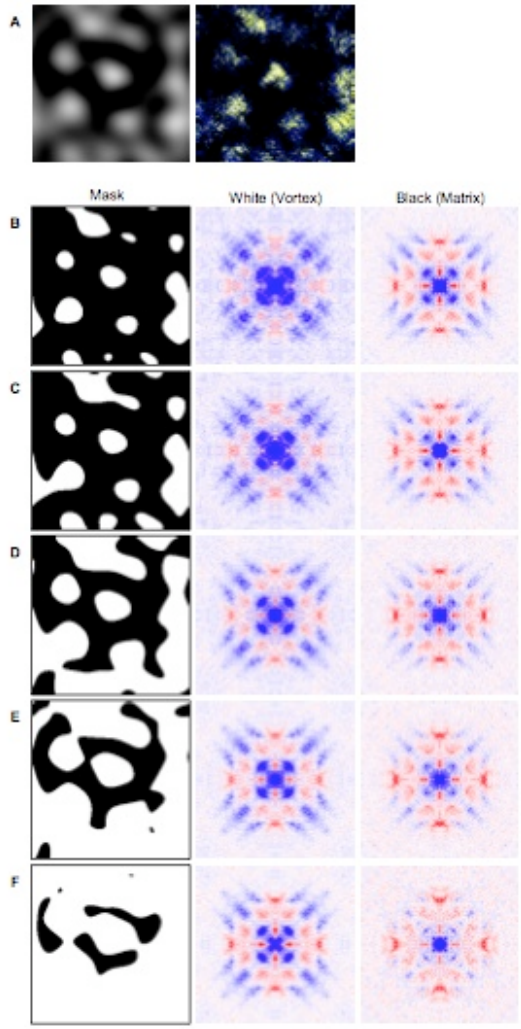

Figure 3.7: Procedure of the restricted-field-of-view $|Z(\mathbf{q}, E)|$ analysis at $B = 11$ T. In order to separate vortex and matrix regions, original vortex image (right panel of (a), reproduced from Figure 3.3(c)) is Fourier filtered as shown in the left panel of (a). A circular region around the origin in q space with a diameter of $0.008 \times 2\pi/a_0$ was used for filtering. Taking contours from the filtered image, a series of masks shown in the left panels of (b) to (f) can be generated. White and black regions denote vortex and matrix regions according to different criteria. In these regions, $|Z(\mathbf{q}, E, B)| - |Z(\mathbf{q}, E, B = 0)|$ are calculated as shown in central and right panels. Intensities are normalized according to the areas of the masks. As indicated in the central column, enhancement of sign-preserving scatterings at $\mathbf{q}_1$, $\mathbf{q}_4$, and $\mathbf{q}_5$ gradually grow as the field of view is restricted to the vortex centers. When the field of view is restricted in the region away from vortices (right panel of (f)), enhancement of sign-preserving scatterings almost disappears. Figures 3.4(c) and 3.4(d) correspond to the central panel of (c) and right panel of (e), respectively.

and are consistent with the Volovik effect (85) which predicts field-induced gapless excitations around the superconducting gap nodes in k space and outside the vortex core in real space.

3.5 Discussion

To summarize, Hanaguri et al. have clearly detected the d-wave coherence factor of a high-Tc cuprate using vortices as controllable quasiparticle scattering centers. Their results establish that vortices selectively activate the quasiparticle scattering channels that preserve the sign of the superconducting gap in k space. Future measurements using this technique may offer the opportunity to probe the nature of the anomalous electronic matter inside the vortex core using quasiparticle vortex scattering, and the method may also be applied to superconductors with other forms of anisotropic gap, such as p-wave and extended s-wave superconductors. Another variant on this method is to examine the coherence factors for scattering off conventional impurities at temperatures above T_c (97): this approach may provide a viable way to probe the nature of the order that develops in the pseudogap normal state (32). Finally, we note that Fourier-transform SI-STM is currently the only method to study the evolution of k-dependent electronic states as a function of magnetic field and in this respect, offers a useful tool for the study of a wide range of field-induced quantum phenomena (95).

Chapter 4

Model for nodal quasiparticle scattering in a disordered vortex lattice

As we discussed in the previous Chapter, recent scanning tunneling experiments on a high-temperature copper oxide superconductor $Ca_{2-x}Na_xCuO_2Cl_2$ by Hanaguri et al. (60) observe field-dependent quasiparticle interference effects which are sensitive to the sign of the d-wave order parameter. The analysis of spatial fluctuations in the local density of states shows that there is a selective enhancement of quasiparticle scattering events that preserve the gap sign, and a selective depression of the quasiparticle scattering events that reverse the gap sign.

In this Chapter, we introduce a model which accounts for this phenomenon as a consequence of vortex pinning to impurities. Each pinned vortex embeds several impurities in its core. The observations of recent experiments can be accounted for by assuming that the scattering potentials of the impurities inside the vortex cores acquire an additional resonant or Andreev scattering component, both of which induce gap sign preserving scattering events.

Let us first summarize the main observations:

- **A selective enhancement of sign-preserving; depression of sign-reversing scattering events**. In a field, Hanaguri et al. (60) observe a selective enhancement of the scattering events between parts of the Brillouin zone with the same gap sign, and a selective depression of the scattering events between parts of the Brillouin zone with opposite gap signs, so that the sign-preserving q-vectors $\mathbf{q}_{1,4,5}$ are enhanced, and the sign-reversing q-vectors $\mathbf{q}_{2,3,6,7}$ are depressed.

- **Large vortex cores** with a core size $\xi \sim 10a$ of order ten lattice constants. Experimentally, vortex cores are imaged as regions of shallow gap (60). The figure $\xi \sim 10a$ is consistent with magnetization and angular resolved photoemission (ARPES) measurements (106).

- **High momentum transfer scattering** involving momentum transfer over a large fraction of the Brillouin zone size at $q_{4,5} \sim k_F$. A paradoxical feature of the observations is the enhancement of high momentum transfer $q \sim \pi/a$ scattering by objects that are of

order ten lattice spacings in diameter. The enhanced high momentum scattering clearly reflects sub-structure on length scales much smaller than the vortex cores.

- **Core-sensitivity**. Fourier mask analysis reveals that the scattering outside the vortex core regions differs qualitatively from scattering inside the vortex core regions. In particular, the enhancement of the sign-preserving scattering events is associated with the signal inside the "vortex cores", whereas the depression of the sign-reversing scattering events is mainly located outside the vortex regions.

Recently, T. Pereg-Barnea and M. Franz (101) have proposed an initial interpretation of these observations in terms of quasiparticle scattering off vortex cores. Their model explains the enhancement of the sign preserving scattering in the magnetic field in terms of scattering off vortex cores, provided vortex cores are small with $\xi \sim a$, as in high temperature superconductor $Bi_2Sr_2CaCu_2O_{8+\delta}$ (Bi2212). However, the large vortex core size of $Ca_{2-x}Na_xCuO_2Cl_2$ is unable to account for the field-driven enhancement in the high momentum scattering.

Motivated by this observation, we have developed an alternative phenomenological model to interprete the high-momentum scattering. In our model, vortices bind to individual impurities, incorporating them into their cores and modifying their scattering potentials. This process replaces random potential scattering off the original impurities with gap-sign-preserving Andreev reflections off order parameter modulations in the vicinity of the pinned vortices. The high-momentum transfer scattering, involved in the selective enhancement and suppression, originates from the impurities whose scattering potentials are modified by the presence of the vortex lattice. Rather than attempt a detailed microscopic model for the pseudo-gap state inside the vortex cores and impurities bound therein, our approach attempts to characterize the scattering in terms of phenomenological form factors that can be measured and extracted from the data.

4.1 Construction of the model

In the absence of a field, random fluctuations in the tunneling density of states are produced by the original impurities. We assume that scattering off the impurities is mutually independent permitting us to write the change in density of states as a sum of contributions from each impurity

$$\delta\rho(\mathbf{r}, V, B = 0) = \sum_j \delta\rho_i(\mathbf{r} - \mathbf{r}_j, V), \tag{4.1}$$

where $\mathbf{r}_j$ denote the positions of the impurities. If

$$n_i = \text{original concentration of impurities in the absence of magnetic field,}$$

then we obtain

$$R(\mathbf{q}, V, B = 0) = \quad n_i \; \overline{\delta\rho_i(\mathbf{q}, V)\delta\rho_i^*(-\mathbf{q}, V)}. \tag{4.2}$$

Next we consider how the quasiparticle scattering changes in the presence of a magnetic field. Pinned vortices arising in the magnetic field act as new scatterers. In the experiment (60), vortices are pinned to the preexisting disorder, so that in the presence of a magnetic field, there are essentially three types of scatterers:

- bare impurities,
- vortices,
- vortex-decorated impurities.

Vortex-decorated impurities are impurities lying within a coherence length of the center of a vortex core. We assume that these three types of scattering centers act as independent scatterers, so that the random variations in the tunneling density of states are given by the sum of the independent contributions, from each type of scattering center:

$$\delta\rho(\mathbf{r}, V, B) = \sum_j \delta\rho_V(\mathbf{r} - \mathbf{r}_j, V) + \sum_l \delta\rho_{DI}(\mathbf{r} - \mathbf{r}'_l, V) + \sum_m \delta\rho_I(\mathbf{r} - \mathbf{r}''_m, V), \tag{4.3}$$

where $\mathbf{r}_j, \mathbf{r}'_l, \mathbf{r}''_m$ denote the positions of vortices, decorated impurities and bare impurities, respectively. In a magnetic field, the concentration of vortices is given by

$$n_V = \text{concentration of vortices} = \frac{2eB}{h},$$

In each vortex core, there will be $n_{core} = n_i\pi(\xi^2/4)$ impurities, where $\pi(\xi^2)/4$ is the area of a vortex and n_i is the original concentration of bare scattering centers in the absence of a field. The concentration of vortex-decorated impurities is then given by

$$n_{DI} = \text{concentration of vortex-decorated impurities} = n_{core}n_V = \frac{2eB}{h}n_i\pi(\xi/2)^2.$$

Finally, the residual concentration of "bare" scattering centers is given by

$$n_I = n_i - n_{DI} = \text{concentration of residual "bare" impurities.} \tag{4.4}$$

Treating the three types of scatterers as independent, we write

$$\begin{aligned} R(\mathbf{q}, V) = \quad & n_V \; \overline{\delta\rho_V(\mathbf{q}, V)\delta\rho_V^*(-\mathbf{q}, V)} + n_{DI} \; \overline{\delta\rho_{DI}(\mathbf{q}, V)\delta\rho_{DI}^*(-\mathbf{q}, V)} \\ + \quad & (n_i - n_{DI}) \; \overline{\delta\rho_I(\mathbf{q}, V)\delta\rho_I^*(-\mathbf{q}, V)}. \end{aligned} \tag{4.5}$$

The first term in (4.5) accounts for the quasiparticle scattering off the vortices, the second term accounts for the quasiparticle scattering off the vortex-decorated impurities and the third term accounts for the quasiparticle scattering off the residual bare impurities in the presence of the superflow. It follows that

$$|Z(q,V,B)|^2 = \frac{2eB}{h}\,|Z_V(q,V,B)|^2 + \frac{2eB}{h}n_{core}|Z_{DI}(q,V,B)|^2 + (n_i - \frac{2eB}{h}n_{core})\,|Z_I(q,V,B)|^2, \tag{4.6}$$

where $Z(q,V,B)$ is given by (2.30), averaged over the vortex configurations. $Z_V(q,V,B)$, $Z_{DI}(q,V,B)$ and $Z_I(q,V,B)$ are Fourier images of the Friedel oscillations in the tunneling density of states induced by vortices, vortex-decorated impurities and bare impurities in the presence of the superflow. Our goal here is to model the quasiparticle scattering phenomenologically, without a recourse to a specific microscopic model of the scattering in the vortex interior. To achieve this goal, we introduce $Z_{VI}(q,V,B)$, a joint conductance ratio of the vortex-impurity composite, which encompasses the scattering off a vortex core and the impurities decorated by the vortex core,

$$|Z_{VI}|^2 = |Z_V|^2 + n_{core}|Z_{DI}|^2, \tag{4.7}$$

so that we obtain

$$|Z(q,V,B)|^2 = \frac{2eB}{h}\,|Z_{VI}(q,V,B)|^2 + (n_i - \frac{2eB}{h}n_{core})|Z_I(q,V)|^2. \tag{4.8}$$

This expression describes quasiparticle scattering in a clean superconductor in low magnetic fields in a model-agnostic way, namely, it is valid regardless of the choice of the detailed model of quasiparticle scattering in the vortex region. $Z_{VI}(q,V,B)$ here describes the scattering off the vortex-impurity composites, which we now proceed to discuss.

4.2 Impurities inside the vortex core: calculating Z_{VI}

As observed in the conductance ratio $Z(\mathbf{q},V,B)$, the intensity of scattering between parts of the Brillouin zone with the same sign of the gap grows in the magnetic field, which implies that the scattering potential of a vortex-impurity composite has a predominantly sign-preserving coherence factor.

We now turn to a discussion of the scattering mechanisms that can enhance sign-preserving scattering inside the vortex cores. Table 2.1 shows a list of scattering potentials and their corresponding coherence factor effects. Weak potential scattering is immediately excluded. Weak scattering off magnetic impurities can also be excluded, since the change in the density

of states of the up and down electrons cancels. This leaves two remaining contenders: Andreev scattering off a fluctuation in the gap function, and multiple scattering, which generates a t-matrix proportional to the unit matrix.

We can, in fact, envisage both scattering mechanisms being active in the vortex core. Take first the case of a resonant scattering center. In the bulk superconductor, the effects of a resonant scatterer are severely modified by the presence of the superconducting gap (75). When the same scattering center is located inside the vortex core where the superconducting order parameter is depressed, we envisage that the resonant scattering will now be enhanced.

On the other hand, we can not rule out Andreev scattering. A scalar impurity in a d-wave superconductor scatters the gapless quasiparticles, giving rise to Friedel oscillations in the order parameter that act as Andreev scattering centers (100; 98; 101). Without a detailed model for the nature of the vortex scattering region, we can not say whether this type of scattering is enhanced by embedding the impurity inside the vortex. For example, if, as some authors have suggested (108), the competing pseudo-gap phase is a Wigner supersolid, then the presence of an impurity may lead to enhanced oscillations in the superconducting order parameter inside the vortex core.

With these considerations in mind, we consider both sources of scattering as follows

$$\hat{t}(\mathbf{q},\mathbf{k},i\omega_n) = t_A(\mathbf{q},\mathbf{k},i\omega_n) + t_R(\mathbf{q},\mathbf{k},i\omega_n) \tag{4.9}$$

where

$$\hat{t}_A(\mathbf{q},\mathbf{k},i\omega_n) = \frac{1}{2}\Delta_0 f_A(\mathbf{q})(\chi_{\mathbf{k}_+} + \chi_{\mathbf{k}_-})\hat{\boldsymbol{\tau}}_1, \qquad \text{(Andreev scattering)}$$

describes the Andreev scattering. Here $\chi_{\mathbf{k}} = c_x - c_y$ is the d-wave function with $c_{x,y} \equiv \cos k_{x,y}$. The resonant scattering is described by

$$\hat{t}_R(\mathbf{q},\mathbf{k},i\omega_n) = i\Delta_0 \mathrm{sgn}(\omega_n)\ f_R(\mathbf{q})\mathbf{1}. \qquad \text{(Resonant scattering)}$$

Using the T-matrix approximation, we obtain for the even and odd components of Fourier transformed fluctuations in the local density of states due to the scattering off the superconducting order parameter amplitude modulation,

$$\delta\rho_{VI}^{even}(\mathbf{q},\omega) = \tfrac{1}{2\pi}\quad \mathrm{Im}\int_{\mathbf{k}} \mathrm{Tr}\Big[G_{\mathbf{k}_-}(\omega - i\delta)\ \hat{t}(\mathbf{q},\mathbf{k},\omega - i\delta)\ G_{\mathbf{k}_+}(\omega - i\delta)\Big], \tag{4.10}$$

$$\delta\rho_{VI}^{odd}(\mathbf{q},\omega) = \tfrac{1}{2\pi}\quad \mathrm{Im}\int_{\mathbf{k}} \mathrm{Tr}\Big[\tau_3 G_{\mathbf{k}_-}(\omega - i\delta)\ \hat{t}(\mathbf{q},\mathbf{k},\omega - i\delta)\ G_{\mathbf{k}_+}(\omega - i\delta)\Big], \tag{4.11}$$

where $\mathbf{k}_\pm = \mathbf{k} \pm \mathbf{q}/2$, $G_{\mathbf{k}}(\omega) = [\omega - \epsilon_{\mathbf{k}}\tau_3 - \Delta_{\mathbf{k}}\tau_1]^{-1}$ is the Nambu Green's function for an electron with normal state dispersion $\epsilon_{\mathbf{k}}$ and gap function $\Delta_{\mathbf{k}}$. We now obtain

$$\delta\rho_V^{even(odd)}(\mathbf{q},\omega) = f_A(\mathbf{q})\Lambda_A^{even(odd)}(\mathbf{q},\omega) + f_R(\mathbf{q})\Lambda_R^{even(odd)}(\mathbf{q},\omega)$$

with

$$\Lambda_A^{even}(\mathbf{q},\omega) = \frac{\Delta_0}{4\pi}\mathrm{Im}\int_k (\chi_{\mathbf{k}_+}+\chi_{\mathbf{k}_-})\left[\frac{z(\Delta_{\mathbf{k}_+}+\Delta_{\mathbf{k}_-})}{(z^2-E^2_{\mathbf{k}_+})(z^2-E^2_{\mathbf{k}_-})}\right]_{z=\omega-i\delta}, \tag{4.12}$$

$$\Lambda_R^{even}(\mathbf{q},\omega) = \frac{\Delta_0}{2\pi}\mathrm{Im}\int_k \left[\frac{-i(z^2+\epsilon_{\mathbf{k}_+}\epsilon_{\mathbf{k}_-}+\Delta_{\mathbf{k}_+}\Delta_{\mathbf{k}_-})}{(z^2-E^2_{\mathbf{k}_+})(z^2-E^2_{\mathbf{k}_-})}\right]_{z=\omega-i\delta}. \tag{4.13}$$

The substantially smaller odd components are:

$$\Lambda_A^{odd}(\mathbf{q},\omega) = \frac{\Delta_0}{4\pi}\mathrm{Im}\int_k (\chi_{\mathbf{k}_+}+\chi_{\mathbf{k}_-})\left[\frac{\epsilon_{\mathbf{k}_+}\Delta_{\mathbf{k}_-}+\epsilon_{\mathbf{k}_-}\Delta_{\mathbf{k}_+}}{(z^2-E^2_{\mathbf{k}_+})(z^2-E^2_{\mathbf{k}_-})}\right]_{z=\omega-i\delta}, \tag{4.14}$$

$$\Lambda_R^{odd}(\mathbf{q},\omega) = \frac{\Delta_0}{2\pi}\mathrm{Im}\int_k \left[\frac{-i\ z(\epsilon_{\mathbf{k}_+}+\epsilon_{\mathbf{k}_-})}{(z^2-E^2_{\mathbf{k}_+})(z^2-E^2_{\mathbf{k}_-})}\right]_{z=\omega-i\delta}. \tag{4.15}$$

where $E_{\mathbf{k}} = [\epsilon^2_{\mathbf{k}}+\Delta^2_{\mathbf{k}}]^{\frac{1}{2}}$ is the quasiparticle energy. The vortex contribution to the Fourier transformed conductance ratio (4.8) is then

$$Z_{VI}(\mathbf{q},V,B) = n_V(Z_A(\mathbf{q},V,B)+Z_R(\mathbf{q},V,B)), \tag{4.16}$$

where

$$Z_A(\mathbf{q},V,B) = f_A(\mathbf{q})\left[(\frac{1}{\rho_0(V)}-\frac{1}{\rho_0(-V)})\Lambda_A^{even}(\mathbf{q},V)+(\frac{1}{\rho_0(V)}+\frac{1}{\rho_0(-V)})\Lambda_A^{odd}(\mathbf{q},V)\right] \tag{4.17}$$

and

$$Z_R(\mathbf{q},V,B) = f_R(\mathbf{q})\left[(\frac{1}{\rho_0(V)}-\frac{1}{\rho_0(-V)})\Lambda_R^{even}(\mathbf{q},V)+(\frac{1}{\rho_0(V)}+\frac{1}{\rho_0(-V)})\Lambda_R^{odd}(\mathbf{q},V)\right]. \tag{4.18}$$

4.3 Numerical simulation

In this section we compare the results of our phenomenological model with the experimental data by numerically computing $Z_{VI}(\mathbf{q},V,B)$ (4.16) for Andreev (4.17) and resonant (4.18) scattering.

In these calculations we took a BCS superconductor with a d-wave gap $\Delta_{\mathbf{k}} = \Delta_0/2(\cos k_x - \cos k_y)$ with $\Delta_0 = 0.2t$ and a dispersion which has been introduced to fit the Fermi surface of an underdoped $Ca_{2-x}Na_xCuO_2Cl_2$ sample with $x = 0.12$ (105):

$$\epsilon_{\mathbf{k}} = -2t(\cos k_x+\cos k_y)-4t'\cos k_x\cos k_y-2t''(\cos 2k_x+\cos 2k_y)+\mu,$$

where $t = 1$, $t' = -0.227$, $t'' = 0.168$, $\mu = 0.486$.

4.4 Evaluation of Z_{VI}

In the absence of a microscopic model for the interior of the vortex core, we model the Andreev and the resonant scattering in the vortex region by constants $f_A(\mathbf{q},i\omega_n) = f_A$ and $f_R(\mathbf{q},i\omega_n) = f_R$. Figure 4.1 shows the results of calculations using these assumptions.

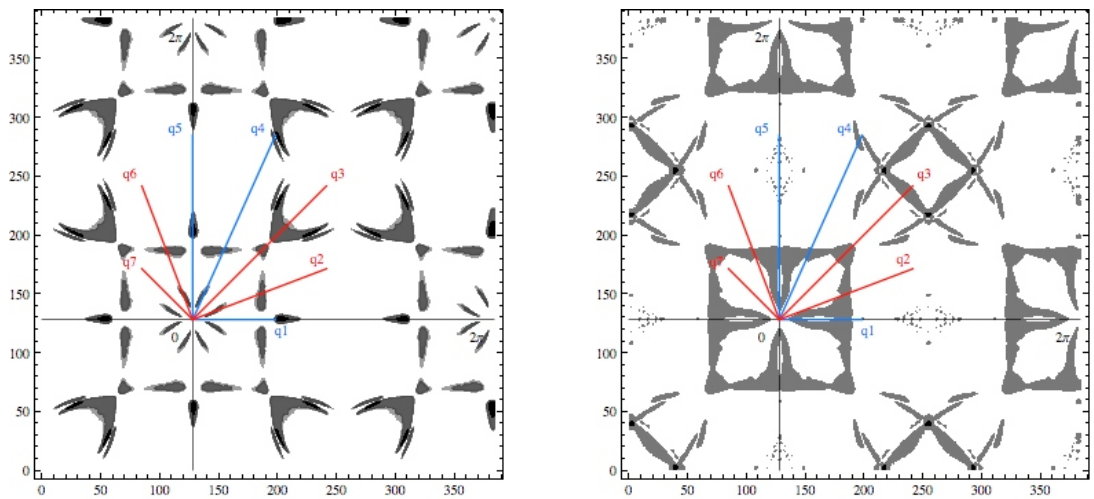

Figure 4.1: Quasiparticle interference produced by the Andreev and the resonant scattering potentials, the primary candidates for producing the experimentally observed enhancement of sign-preserving scattering. Figure (a) displays a density plot of the squared Fourier transformed conductance ratio $|Z_A(\mathbf{q}, V)|^2$ predicted by (4.17) at a bias voltage $V = \Delta_0/2$ produced by pure Andreev scattering ($f_A \neq 0$, $f_R = 0$). Figure (b) displays a density plot of the squared Fourier transformed conductance ratio $|Z_R(\mathbf{q}, V)|^2$ predicted by (4.18) at a bias voltage $V = \Delta_0/2$ produced by resonant scattering ($f_R \neq 0$, $f_A = 0$). Blue lines label the positions of the sign-preserving q-vectors $q = q_{1,4,5}$, where both Andreev and resonant scattering is peaked. Red lines label the positions of the sign-reversing q-vectors $q = q_{2,3,6,7}$, where both Andreev and resonant scattering is minimal.

Our simple model reproduces the enhancement of sign-preserving q-vectors $q_{1,4,5}$ as a result of Andreev and resonant scattering off vortex-impurity composites. Some care is required in interpreting Figure 4.1, because the squared conductance ratio $|Z(\mathbf{q}, V)|^2$ contains weighted contributions from both even and odd fluctuations in the density of states, with the weighting factor favoring *odd* fluctuations, especially near $V = 0$. Both Andreev and resonant scattering contribute predominantly to the even fluctuations of the density of states (see Table 2.1), and give rise to the signals at $q_{1,4,5}$. In the case of resonant scattering, we observe an additional peak at q_3. From Table 2.1, we see that the Andreev and the resonant scattering potentials also produce a signal in the odd channel which experiences no coherence factor effect, contributing to all the octet q-vectors, which, however, enters the conductance ratio $Z(\mathbf{q}, V)$ given by (2.29) with a substantial weighting factor. This is the origin of the peak at q_3 in Figure 4.1(b).

4.5 Comparison with experimental data

The results of the calculation of the full squared conductance ratio $|Z(q, V, B)|^2$ are obtained by combining the scattering off the impurities inside the vortex core Z_{VI} with the contribution

from scattering off impurities outside the vortex core Z_I, according to equation (4.8), reproduced here:

$$|Z(q,V,B)|^2 = \frac{2eB}{h}\ |Z_{VI}(q,V,B)|^2 + (n_i - \frac{2eB}{h} n_{core})\ |Z_I(q,V,B)|^2. \tag{4.19}$$

where $n_{core} = n_i \pi(\xi/2)^2$ is the number of impurities per vortex core. Figure 4.2 displays a histogram of the computed field-induced change in the conductance ratio $|Z(\mathbf{q}_i, V, B)|^2 - |Z(\mathbf{q}_i, V)|^2$ at the octet q-vectors. In these calculations, we took an equal strength of Andreev and resonant scattering $f_R = f_A$, with a weak scalar scattering outside the vortex core of strength $f_I = f_R = f_A$. In all our calculations, we find that Andreev and resonant scattering are equally effective in qualitatively modelling the observations. The main effect governing the depression of sign-preserving wavevectors $q_{1,4,5}$ derives from the change in the impurity scattering potential that results from embedding the impurity inside the vortex core.

We estimated the percentage of the impurities decorated by the vortices from the fraction of sample area covered by the vortices. The concentration of vortices is $n_V(B) = 2eB/h = B/\Phi_0$, where $\Phi_0 = h/(2e) = 2.07 \times 10^{-15}$ weber is the superconducting magnetic flux quantum. The area of a vortex region is estimated as $A_V = \pi(\xi_0/2)^2$ with the superconducting coherence length $\xi_0 = 44$ Å(102), so that the percentage of the original impurities that are decorated by vortices in the presence of the magnetic field is $\alpha(B) = n_V(B)\ A_V$. Using these values, we obtain for the magnetic field of $B = 5$ T $\alpha(B = 5\ T) \approx 3.7\%$, and for $B = 11$ T $\alpha(B = 11\ T) \approx 8.1\%$. For simplicity, we assume that a vortex core is pinned to a single impurity, $n_{core} = n_i \pi(\xi/2)^2 = 1$, so that the ratio of the concentrations of the impurities and vortices is $n_i/n_V(B) \ = n_{core}/A_V/(2eB/h)$, which becomes for $B = 5$ T $n_i/\ n_V(B = 5T) \approx 27$, and for $B = 11$ T $n_i/n_V(B = 11T) \approx 12$.

In Figure 4.2 we have modelled the scattering provided the origin of the selective enhancement is the Andreev (Figure (a)) or the resonant (Figure (b)) scattering in the vortex core region. Both the Andreev and the resonant scattering are equally effective in qualitatively modelling the observations. Thus our model has qualitatively reproduced the experimentally observed enhancement of the sign-preserving scattering and the depression of the sign-reversing scattering.

4.6 Discussion

In this work, we have shown how scanning tunneling spectroscopy can serve as a phase-sensitive probe of the superconducting order parameter. In particular, we find that the even and odd

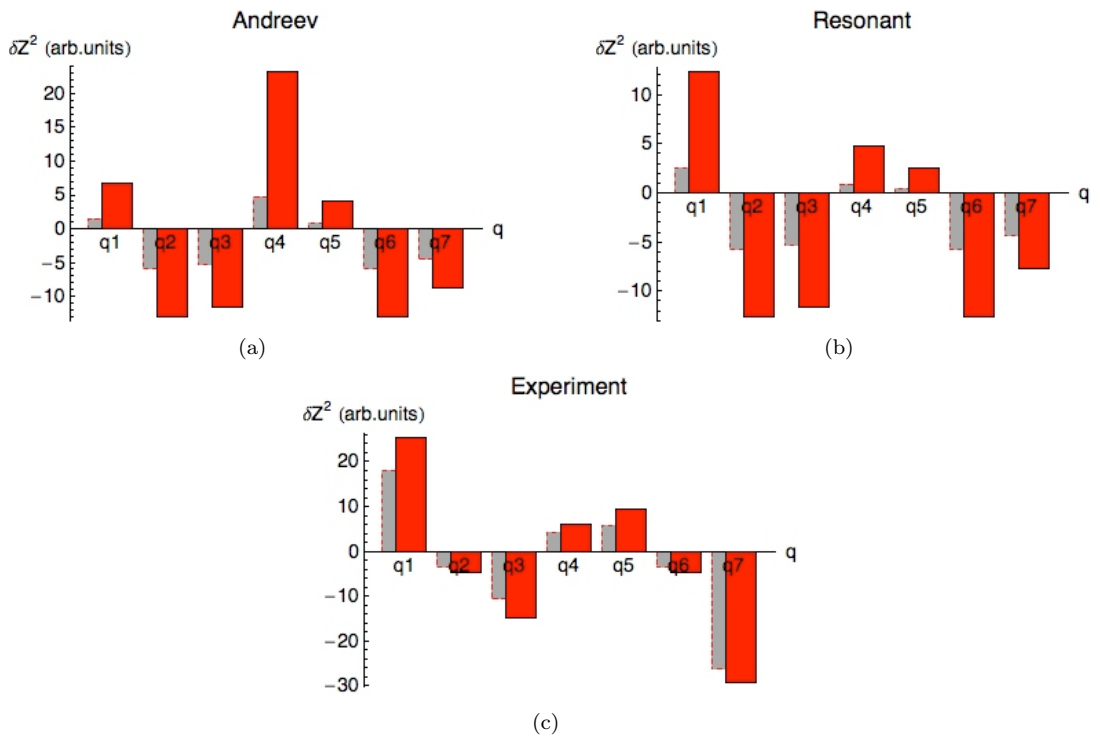

Figure 4.2: Comparison between the results of the model calculations and the experimental data. Figs. (a)-(b) show the change in the squared Fourier transformed conductance ratio $\delta Z^2 \equiv |Z(\mathbf{q}, V, B)|^2 - |Z(\mathbf{q}, V, B = 0)|^2$ at $\mathbf{q} = q_{1-7}$, computed for a magnetic field of B =5 T (grey bars) and 11 T (red bars) at a bias voltage $V = \Delta_0/2$, provided the origin of the selective enhancement is the Andreev (Figure (a)) or the resonant (Figure (b)) scattering in the vortex core region. Here a vortex, pinned to a scalar impurity, transforms its original scattering potential with enhanced scattering at $q = q_{2,3,6,7}$ into an Andreev (Figure (a)) or into a resonant (Figure (b)) scattering potential with enhanced scattering at $q = q_{1,4,5}$ (see Table 2.1). Figure (c) shows the experimentally observed change in the squared Fourier transformed conductance ratio $\delta Z^2 \equiv |Z(\mathbf{q}, V, B)|^2 - |Z(\mathbf{q}, V, B = 0)|^2$ at $\mathbf{q} = q_{1-7}$, in a magnetic field of B =5 T (grey bars) and 11 T (red bars) at a bias voltage $V = 4.4$ meV.

components of the density of states fluctuations can be associated with a well-defined coherence factor. The measured Fourier transformed conductance ratio $Z(\mathbf{q}, V) = \frac{dI/dV(\mathbf{q},+V)}{dI/dV(\mathbf{q},-V)}$ is a weighted combination of these two terms, and in the limit of particle-hole symmetry it is dominated by the odd component of the density of states. Observation of coherence factor effects with scanning tunneling spectroscopy requires the presence of controllable scatterers. In the study by Hanaguri et al. (60) these controllable scatterers are vortices.

Our phenomenological model of quasiparticle scattering in the presence of vortices is able to qualitatively reproduce the observed coherence factor effects under the assumption that impurity scattering centers inside the vortex cores acquire an additional Andreev or resonant scattering component.

This study raises several questions for future work. In particular, can a detailed model of a d-wave vortex core provide a microscopic justification for the modification of the impurity scattering potential? One of the issues that can not be resolved from the current analysis, is whether the enhanced Andreev scattering originates in the core of the pure vortex, ($|Z_V|^2$), or from the decoration of impurities that are swallowed by the vortex core ($n_{core}|Z_{DI}|^2$). This is an issue that may require a combination of more detailed experimental analysis and detailed modelling of vortex-impurity composites using the Bogoliubov de Gennes equations. Another open question concerns whether it is possible to discriminate between the Andreev and resonant scattering that appear to be equally effective in accounting for the coherence factor effects.

There are several aspects to the experimental observations that lie beyond our current work. For example, experimentally, it is possible to spatially mask the Fourier transform data, spatially resolving the origin of the scattering. These masked data provide a wealth of new information. In particular, most of the enhancement of the sign preserving scattering is restricted to the vortex core region, as we might expect from our theory. However, to extend our phenomenology to encompass the masked data, requires that we compute the fluctuations of the density of states as a function of distance from the vortex core,

$$R(\mathbf{r}, \mathbf{r}'; \mathbf{r}_V, V) = \langle \delta\rho(\mathbf{r} - \mathbf{r}_V, V)\delta\rho(\mathbf{r}' - \mathbf{r}_V, V)\rangle, \tag{4.20}$$

a task which requires a microscopic model of the vortex core.

In our theory we have used the bulk quasiparticle Green's functions to compute the scattering off the vortex-decorated impurities. Experiment does indeed show that the quasiparticle scattering off impurities inside the vortex cores is governed by the quasiparticle dispersion of the bulk: can this be given a more microscopic understanding? The penetration of superconducting

quasiparticles into the vortex core is a feature that does not occur in conventional s-wave superconductors. It is not clear at present to what extent this phenomenon can be accounted for in terms of a conservative d-wave superconductor model, or whether it requires a more radical interpretation. One possibility here, is that the quasiparticle fluid in both the pseudo-gap phase and inside the vortex cores is described in terms of a "nodal liquid" (107).

Beyond the cuprates, scanning tunneling spectroscopy in a magnetic field appears to provide a promising phase-sensitive probe of the symmetry of the order parameter in unconventional superconductors. One opportunity that this raises, is the possibility of using STM in a field to probe the gap phase of the newly discovered iron-based high-temperature superconductors. According to one point of view (110), the iron-based pnictide superconductors possess an $s_{\pm}$ order parameter symmetry in which the order parameter has opposite signs on the hole pockets around Γ and the electron pockets around M. If this is, indeed, the case, then in a magnetic field quasiparticle scattering between parts of Fermi surface with same gap signs should exhibit an enhancement, while scattering between parts of Fermi surface with opposite gap signs will be suppressed. This is a point awaiting future theoretical and experimental investigation.

Chapter 5
Theory of tunneling into a Kondo lattice

In this Chapter, motivated by recent experimental interest in tunneling into heavy electron materials, we present a theory for electron tunneling into a Kondo lattice. By incorporating the effect of a tunneling tip on the Kondo spin-exchange processes, we show that the tunneling Hamiltonian develops an additional co-tunneling component, in which the passage of an electron into the Kondo lattice is accompanied by a simultaneous spin flip of the localized moments. Using a large-N approximation, we develop a simple phenomenological description of these tunneling processes in the heavy Fermi liquid state of a Kondo lattice, showing that the conventional Fano line-shape of single-impurity tunneling develops an additional double-peaked structure with a hybridization gap.

5.1 Introduction

Major developments in scanning tunneling spectroscopy (STM) over the last decade, particularly as a probe of cuprate superconductors (70; 113; 114), suggest that this tool will find increasing utility as an atomic-scale probe of many-body phenomena in many new classes of materials. One area of particular promise lies in the application of STM to heavy fermion materials.

Heavy fermion materials contain a dense lattice of localized magnetic moments interacting with a sea of conduction electrons to form a "Kondo lattice" (115; 116). These materials present dramatic manifestations of collective many-body electronic phenomena, such as anisotropic superconductivity, non-Fermi liquid behavior, and quantum criticality. Motivated by recent tunneling experiments on f-electron materials (117; 118; 119), in this Chapter we develop a theory for the tunneling response of a coherent heavy-fermion material.

The physics of tunneling into a metal containing a dilute concentration of local moments has a long history dating back more than forty years (120; 121; 122). Since direct tunneling into a localized magnetic orbital is blocked by Coulomb interactions, the naive expectation is that the effects of local moments on tunneling only manifest themselves through their indirect influence on the surrounding conduction sea. Yet this is not the case: in 1960s Anderson and Appelbaum

(121; 122) recognized that magnetic ions actively participate in the tunneling process via a "co-tunneling" mechanism (123; 124) in which the passage of an electron into the conduction sea occurs co-operatively with a spin-flip of localized moments. In this Chapter we examine the effect of these processes on tunneling into a coherent band of excitations of a Kondo lattice. We show that these co-tunneling processes open up a direct tunneling channel between the tip and the composite quasiparticle states of the Kondo lattice. Once coherence develops, co-tunneling and direct tunneling processes interfere with each other, giving rise to a distinctive three-peak structure in the tunneling spectra.

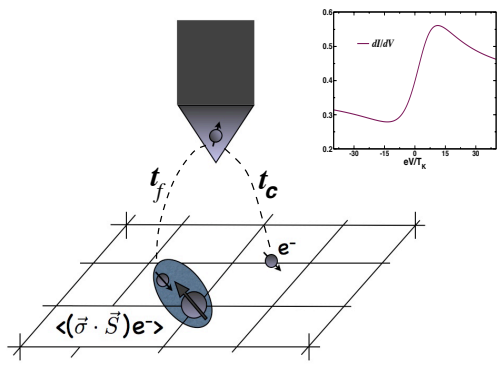

Figure 5.1: Tunneling of an electron from a tip into a heavy-fermion material involves two types of processes. The first one corresponds to the tunneling with an amplitude t_c into conduction sites. The second one consists of tunneling with an amplitude t_f into the composite states between the conduction electrons and local magnetic f-moments. These composite states represent the fabric of the coherent heavy-fermion state of the Kondo lattice formed below coherence temperature T_K. The inset shows the typical differential conductance curve as a function of voltage at temperatures well below T_K.

5.2 Tunneling Hamiltonian

We begin by writing down the Kondo lattice Hamiltonian in the presence of a tunneling probe, which takes the form $\hat{H} = \hat{H}_{KL} + \hat{H}_{tip} + \hat{H}_T$, where

$$\hat{H}_{KL} = \sum_{\mathbf{k},\sigma} \epsilon_{\mathbf{k}} c^\dagger_{\mathbf{k}\sigma} c_{\mathbf{k}\sigma} + J \sum_j \vec{S}_f(j) \cdot (c^\dagger_{j\alpha} \vec{\sigma}_{\alpha\beta} c_{j\beta}) \tag{5.1}$$

is the unperturbed Kondo lattice Hamiltonian, $c^\dagger_{j\sigma} = \frac{1}{\sqrt{V}} \sum_{\mathbf{k}} c^\dagger_{\mathbf{k}\sigma} e^{i\mathbf{k}\cdot\mathbf{R}_j}$ creates a conduction electron and $\vec{S}_f(j)$ is the spin operator of a localized f-electron at site j, respectively. The term $\hat{H}_{tip} = \sum_{\mathbf{k}\sigma} \epsilon_{\mathbf{k}} \hat{p}^\dagger_{\mathbf{k}\sigma} \hat{p}_{\mathbf{k}\sigma}$ describes the electrons in the tip. When the tunneling tip is in the vicinity of site 0, the tunneling Hamiltonian is

$$\hat{H}_T \quad = \quad \hat{p}^\dagger_{0\alpha} \psi_{0\alpha} + \text{H.c.},$$

$$\psi_{0\alpha} \quad = \quad t_c \hat{c}_{0\alpha} + \tilde{t}_f \left(\vec{\sigma}_{\alpha\beta} \cdot \vec{S}_f(0) \right) \hat{c}_{0\beta}. \tag{5.2}$$

It contains a direct tunneling term of amplitude t_c and a "co-tunneling" term of amplitude $\tilde{t}_f$, in which the passage of an electron from the lattice into the tip is accompanied by a spin-flip of the local moment. This Hamiltonian is a simple generalization of the Anderson-Appelbaum tunneling Hamiltonian (121; 122), introduced to explain zero-bias anomalies associated with tunneling between two metallic leads via a single localized moment. Similar models have subsequently been used to describe tunneling through a quantum dot (124).

The co-tunneling component of H_T can be understood as a result of the hybridization of the states of the tunneling tip with the localized orbitals of the Kondo lattice. This modifies the Wannier states that hybridize with the localized moments. A derivation of the co-tunneling terms can be made by carrying out a Schrieffer-Wolff transformation on an Anderson model describing the lattice and tip (122; 124; 135). In an Anderson model, the localized f-electrons hybridize with the conduction electrons. When a tunneling probe is located at site 0 of the lattice, tunneling between the f-state and the probe electrons modifies the hybridization at site 0 according to

$$H_h \to (V c^\dagger_{0\sigma} + t_f p^\dagger_{0\sigma}) f_{0\sigma} + \text{H.c},$$

where t_f is the amplitude to tunnel directly from an f-state to the probe. From this consideration, we see that the effect of the tip at site is to modify the orbital hybridizing with the f-state:

$$c_{0\sigma} \to c_{0\sigma} + \frac{t_f}{V} p_{0\sigma}$$

at site 0. After a Schrieffer-Wolff transformation is made, reducing the Anderson model to a Kondo model, this same replacement must be made to the Kondo interaction at site 0 in the unperturbed Kondo lattice model. To the leading linear order in t_f/V, the result of this procedure is the quoted result in Equation (5.2), where $\tilde{t}_f = J t_f / V$.

To compute the tunneling current for tunneling into a Kondo lattice, we use linear response theory (125). We consider the tunneling as a small perturbation applied adiabatically, and use the Kubo formula to find

$$I(eV) = \frac{2\pi e}{\hbar} \int d\varepsilon \; \rho_{tip}(\varepsilon + eV) \rho_\psi(\varepsilon) (f(\varepsilon) - f(\varepsilon + eV)), \tag{5.3}$$

where $f(\varepsilon)$ is the Fermi function, $\rho_{tip}(\varepsilon)$ is the local density of states of the tip, $\rho_\psi(\varepsilon)$ is the local density of states of the sample given by

$$\rho_\psi(\varepsilon) \quad \equiv \quad \frac{1}{\pi} \text{ Im } G_\psi(\varepsilon - i\delta), \tag{5.4}$$

where

$$G_\psi(\varepsilon) \quad = \quad \frac{1}{2}\sum_\alpha \int_{-\infty}^{\infty} dt \left\langle \psi_{0\alpha}(t), \psi^\dagger_{0\alpha}(0) \right\rangle e^{i\varepsilon t}. \tag{5.5}$$

To illustrate the tunneling into the Kondo lattice, we now solve for the tunneling behavior in the large-N limit (126; 127) of the Kondo lattice, where $N = 2j+1$ is the spin degeneracy of the localized f-state. In this approach, the spin operator is represented as a bilinear of fermions (128), $\vec{S}_f(j) = \hat{f}_{j\alpha}\vec{S}_{\alpha\beta}\hat{f}_{j\beta}$, where $\vec{S}_{\alpha\beta}$ are the generators of the $SU(N)$ symmetry group. The mean-field theory provides a representation of the composite fermion $\left(\vec{\sigma}_{\alpha\beta}\cdot\vec{S}_f(j)\right)\hat{c}_{j\beta}$ in (5.2) in terms of a product of a single pseudo-fermion $\hat{f}_{j\alpha}$ and the average $-\langle \hat{f}^\dagger_{j\beta}\hat{c}_{j\beta}\rangle = \frac{\mathcal{V}}{NJ}$, so that

$$\sum_\beta \left(\vec{\sigma}_{\alpha\beta}\cdot\vec{S}_f(j)\right)\hat{c}_{j\beta} \to \frac{\mathcal{V}}{J}\hat{f}_{j\alpha}. \tag{5.6}$$

In this way, the large-N mean field theory captures the formation of a composite heavy f-electron.

In terms of pseudo-fermions, we can write Equation (5.2) as

$$\hat{\psi}_{j\alpha} = t_c\hat{c}_{j\alpha} + \tilde{t}_f\hat{f}_{j\beta}, \tag{5.7}$$

where the complex amplitude for tunneling into the composite fermion state is $\tilde{t}_f = \frac{\mathcal{V}}{J}t_f$.

The requirement that the number of pseudo-fermions at any given site should be equal to $N/2$ introduces a constraint λ, to be determined self-consistently together with the hybridization amplitude $\mathcal{V}$. The resulting mean-field Hamiltonian can be then diagonalized by means of the Bogoliubov transformation $\hat{c}_{\mathbf{k}\sigma} = v_{\mathbf{k}}\hat{a}_{\mathbf{k}\sigma} + u_{\mathbf{k}}\hat{b}_{\mathbf{k}\sigma}$, and $\hat{f}_{\mathbf{k}\sigma} = u_{\mathbf{k}}\hat{a}_{\mathbf{k}\sigma} - v_{\mathbf{k}}\hat{b}_{\mathbf{k}\sigma}$, where $u_{\mathbf{k}}$ and $v_{\mathbf{k}}$ are the Kondo lattice coherence factors given by $u^2_{\mathbf{k}} = [R_{\mathbf{k}} + (\varepsilon_{\mathbf{k}} - \lambda)]/2R_{\mathbf{k}}$, $v^2_{\mathbf{k}} = 1 - u^2_{\mathbf{k}}$ with $R_{\mathbf{k}} = \sqrt{(\varepsilon_{\mathbf{k}} - \lambda)^2 + 4\mathcal{V}^2}$. The Hamiltonian (5.1) in the mean-field approximation then becomes $H^{(mf)}_{KL} = \sum_{\mathbf{k}\alpha}(\omega_{-\mathbf{k}}\hat{a}^\dagger_{\mathbf{k}\alpha}\hat{a}_{\mathbf{k}\alpha} + \omega_{+\mathbf{k}}\hat{b}^\dagger_{\mathbf{k}\alpha}\hat{b}_{\mathbf{k}\alpha})$, where $\omega_{\pm\mathbf{k}} = (\varepsilon_{\mathbf{k}} + \lambda \pm R_{\mathbf{k}})/2$ is the quasiparticle dispersion in the newly developed heavy Fermi liquid. The tunneling Hamiltonian acquires a particularly simple form

$$\hat{H}^{(mf)}_T = \frac{1}{N}\sum_{j\alpha}\hat{p}^\dagger_{j\alpha}\left[t_c\hat{c}_{j\alpha} + t_f\hat{f}_{j\alpha}\right] + h.c. \tag{5.8}$$

where we have absorbed $\mathcal{V}$ into the tunneling amplitude t_f for brevity, $t_f \to \frac{\mathcal{V}}{J}t_f$. Although our mean-field Hamiltonian has the form of the Anderson lattice model with $U = 0$, the states on which it operates have a different physical meaning. These states are composite states formed with local spins hybridized with conduction electrons. Thus our Hamiltonian Equation (5.8) describes tunneling into the conduction band together with the co-tunneling processes involving local moments.

5.3 Tunneling conductance

For our subsequent discussion, it is instructive to compare our results for the tunneling conductance in a Kondo lattice with those obtained in the case of a single Kondo impurity. In both cases, we employ the same large-N mean-field theory.

Using the tunneling Hamiltonian Equation (5.8), we compute $G_\psi(\omega)$ Equation (5.5). In the case of a single Kondo impurity, we obtain

$$G_\psi^{imp}(\omega) = \frac{(t_c i\pi\rho\mathcal{V} + t_f)^2}{\omega - \lambda - i\Delta} + t_c^2 i\pi\rho, \tag{5.9}$$

where ρ is the density of states of the conduction electrons, $\Delta = \pi\rho\mathcal{V}^2 \simeq T_K$ is the width of the Kondo resonance. The differential tunneling conductance $\frac{dI}{dV}(eV) \equiv g(eV)$ is

$$g_{imp}(eV) = \frac{2\pi e^2}{\hbar} t_c^2 \ \rho_{tip} \ \rho_F(\epsilon') \ \frac{|q + \epsilon'|^2}{1 + \epsilon'^2}. \tag{5.10}$$

Here $q = A/B$ is the ratio of complex tunneling amplitudes, $A(eV) = t_f + t_c\mathcal{V}P(\frac{1}{eV - \epsilon_{\mathbf{k}}})$ describes the coupling of the STM tip to the atomic orbital, the first term in A describes direct coupling of the STM tip to the atomic orbital, whereas the second term in A describes indirect coupling of the STM tip to the atomic orbital via virtual transitions involving band electrons, $B = t_c\mathcal{V}\pi\rho$ describes coupling of the tip to the local density of states of the metal (129). $\epsilon' = (eV - \lambda)/\Delta$, ρ_{tip} is the density of states at the Fermi level of electrons in the tip, and ρ_F is the density of states of the sample. The half-width of the resonance is controlled by $\Delta \sim T_K$.

Now we turn to the case of the Kondo lattice. Within the large-N mean-field theory, we obtain

$$G_\psi^{KL}(\omega) = \sum_{\mathbf{k}} \frac{(t_c + t_f \frac{\mathcal{V}}{\omega - \lambda})^2}{\omega - \epsilon_{\mathbf{k}} - \frac{\mathcal{V}^2}{\omega - \lambda}}, \tag{5.11}$$

where $\epsilon_{\mathbf{k}}$ is the dispersion of the conduction band. We obtain the following expression for the differential tunneling conductance,

$$g_{KL}(eV) = \frac{2\pi e^2}{\hbar} t_c^2 \ \rho_{tip} \sum_{s=\pm,\mathbf{k}} \frac{|q + E_{s\mathbf{k}}|^2}{1 + E_{s\mathbf{k}}^2} \delta(eV - \omega_{s\mathbf{k}}), \tag{5.12}$$

where $E_{s\mathbf{k}} = (\omega_{s\mathbf{k}} - \lambda)/\Delta$. The prefactor of the delta-function has a characteristic Fano functional form (130). This form introduces an asymmetry in the resulting voltage dependence of the tunneling conductance $g_{KL}(eV)$. The momentum summation in $G_\psi^{KL}(\omega)$ (5.11) and $g_{KL}(eV)$ (5.12) can be carried out analytically assuming parabolic dispersion of the conduction electrons, $\varepsilon_{\mathbf{k}} = \mathbf{k}^2/2m - \mu$, where μ is the chemical potential, the conduction band involves energies in the range of $[-D, D]$. We obtain

$$G_\psi^{KL}(\omega) = \left(t_c + t_f \frac{\mathcal{V}}{\omega - \lambda}\right)^2 \log\Big[\frac{\omega + \mu - \frac{\mathcal{V}^2}{\omega - \lambda}}{\omega - D - \frac{\mathcal{V}^2}{\omega - \lambda}}\Big] + t_f^2 \frac{\mu + D}{\omega - \lambda}. \tag{5.13}$$

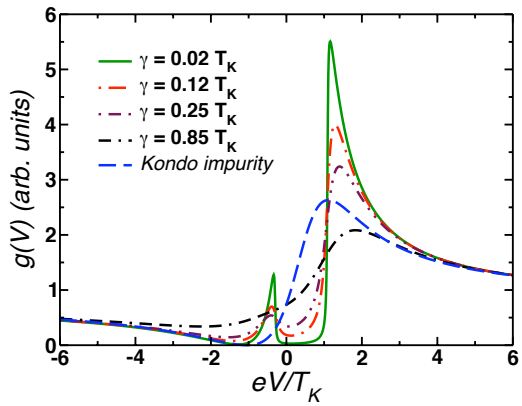

Figure 5.2: Differential tunneling conductance $g(V)$ for a single Kondo impurity case (double dash-dotted line) given by (5.10), a Kondo lattice (dash-dotted line) given by (5.14). A typical Fano shape in the single Kondo impurity case gets replaced with a double-peaked resonance line in the Kondo lattice case. The solid curve and dotted lines illustrate the effect of disorder, which removes the coherence, closes the gap in DOS, and smoothes the $dI/dV(eV)$ curve. Here $t_f/t_c = .2$, $q = t_f/t_c\mathcal{V}\pi\rho = 4.9$, $\lambda = .3$, $\mu = 75$, $D = 100$, $\mathcal{V} = 7.74$, $\Delta = \pi\rho\mathcal{V}^2 = 1$.

Now the tunneling conductance is given by

$$g_{KL}(eV) = \frac{2\pi e^2}{\hbar}\rho_{tip}\ \rho_{KL}(eV)\ |t_c|^2\frac{|q+\epsilon'|^2}{1+\epsilon'^2}, \tag{5.14}$$

where $\rho_{KL}(eV)$ is the density of states of the Kondo lattice. Within our mean-field theory, it is given by $\rho_{KL}(eV) = \rho(1+\epsilon'^{-2})\log\left[\frac{(eV+\mu)\pi\rho\epsilon'-1}{(eV-D)\pi\rho\epsilon'-1}\right] + \rho(\mu+D)\frac{q^2(1+\epsilon'^2)}{\epsilon'(q+\epsilon')^2}$ with ρ being the density of states of the conduction electrons. We assumed that $\mu+\lambda, D-\lambda \gg \mathcal{V}$. From Equation (5.14) we observe that the differential tunneling conductance has two well-pronounced peaks at $eV \sim \lambda$ separated by a narrow gap of order $\mathcal{V}^2((\mu+\lambda)^{-1}+(D-\lambda)^{-1})$. The appearance of the gap in the tunneling conductance is not surprising. Indeed, the onset of the coherence in the Kondo lattice can be viewed as the band structure reconstruction leading to the opening of the hybridization gap $\Delta_g \sim 2\mathcal{V}^2/D$ in the single particle spectrum. This feature is reflected in the tunneling conductance (5.14).

While a detailed treatment of the effects of disorder in the Kondo lattice is beyond the current treatment (131), a phenomenological quasiparticle elastic relaxation rate Γ may be simply introduced into the theory by replacing $\omega \to \omega + i\Gamma$ in Equation (5.11). The results of this procedure are shown in Figure 2. As we see, strong disorder removes the coherence that had provided the peaks in the tunneling conductance $g_{KL}(V)$ (5.14). The resulting lineshape of the tunneling conductance $dI/dV(eV)$ is an asymmetric smooth curve.

5.4 Discussion

Our results provide a simple framework for the interpretation of scanning tunneling measurements on a Kondo lattice. The current work can be extended in a number of interesting directions. One important aspect, is to examine the effects of co-tunneling on the fluctuations in the density of states probed in Fourier transform STM experiments. In one-band systems, the Fourier transform of these fluctuations is phase sensitive to quasiparticle scattering and is expected to be an important probe of both quasiparticle dispersion and the phase of the co-tunneling matrix elements. The interplay of co-tunneling with these processes is expected to play an important role in the interpretation of Fourier transformed STM.

Another fascinating aspect of the co-tunneling warranting investigation, is its interplay with various forms of heavy fermion order, such as heavy fermion superconductivity. A recent work has proposed that heavy electron superconductivity may involve composite pairing between local moments and electron pairs (132). In such models, the co-tunneling Hamiltonian between the tip and f-electron may develop pairing components that result in Andreev reflection, even in the limit of weak tunneling. The detailed analysis of the differential conductance line shape in this case is a subject of our ongoing research.

In conclusion, we have studied tunneling into a Kondo lattice at temperatures well below the coherence temperature. The nontrivial contribution to the differential tunneling conductance originates from the composite states of the heavy Fermi liquid. These composite states are described by the nonzero average of the product of the conduction electron spin and local f-moments within the large-N mean field theory. In a clean system the differential tunneling conductance will display two peaks separated by the hybridization gap. Addition of disorder leads to the smearing of the gap and produces a Fano-like smooth asymmetric lineshape in the tunneling conductance.

Bibliography

[1] H.K. Onnes, Nobel Lecture (1913).

[2] W. Meissner and R. Oschenfeld, Naturwiss. **21**, 787 (1933).

[3] F. and H. London, Proc. Roy. Soc. (London) **A149**, 71 (1935).

[4] F. London, Proc. Roy. Soc. (London) **152A**, 24 (1935).

[5] A.B. Pippard, Proc. Roy. Soc. (London) **A216**, 547 (1953).

[6] T.E. Faber, A.B. Pippard, Proc. Roy. Soc. (London) **A231**, 336 (1955).

[7] V. L. Ginzburg, and L.D. Landau, Zh. Eksp. Teor. Fiz. **20**, 1064 (1950).

[8] A. A. Abrikosov, Sov. Phys. JETP **5**, 1174 (1957).

[9] J. Bardeen, Encycl. of Physics, S. Flugge, ed. Berlin, Springer Verlag, **XV**, 274 (1956).

[10] J. Bardeen, Nobel Lecture (1972).

[11] L. N. Cooper, Phys. Rev. **104**, 1189 (1956). J. Bardeen, L. N. Cooper, and J. R. Schrieffer, Phys. Rev. **106**, 162 - 164 (1957). J. Bardeen, L. N. Cooper, and J. R. Schrieffer, Phys. Rev. **108**, 1175 (1957).

[12] M. A. Biondi, A. T. Forrester, M. P. Garfunkel, and C. B. Satterthwaite, Rev. Mod. Phys. **30**, 1109 - 1136 (1958).

[13] L. C. Hebel and C. P. Slichter, Phys. Rev. **113**, 1504 (1959).

[14] R. W. Morse and H. V. Bohm, Phys. Rev. **108**, 1094 (1957).

[15] R. E. Glover and M. Tinkham, Phys. Rev. **104**, 844 (1956).

[16] L. Esaki, Nobel Lecture (1973).

[17] I. Giaever, Nobel Lecture (1973).

[18] B. Josephson, Nobel Lecture (1973).

[19] J. Bardeen, Phys. Rev. Lett. **6 (2)**, 57 - 59 (1961); J. Bardeen, Phys. Rev. Lett. **9**, 147 - 149 (1962).

[20] M. H. Cohen, L. M. Falicov, and J. C. Phillips, Phys. Rev. Lett. **8**, 316 - 318 (1962).

[21] G. Binnig, H. Rohrer, Ch. Gerber, and E. Weibel, Phys. Rev. Lett. **50**, 120 - 123 (1983); G. Binnig, H. Rohrer, Ch. Gerber, and E. Weibel, Phys. Rev. Lett. **49**, 57 - 61 (1982); G. Binnig, H. Rohrer, Ch. Gerber, and E. Weibel, Appl. Phys. Lett. **40**, issue 2, 178-180 (1982).

[22] J. Tersoff and D. R. Hamann, Phys. Rev. Lett. **50 (25)**, 1998 - 2001 (1983). J. Tersoff and D. R. Hamann, Phys. Rev. B **31**, 805 - 813 (1985).

[23] C. E. Gough, M. S. Colclough, E. M. Forgan, R. G. Jordan, M. Keene, C. M. Muir- head, A. I. M. Rae, N. Thomas, J. S. Abell, and S. Sutton, Nature **326**, 855 (1987).

[24] C. C. Tsuei, J. R. Kirtley, C. C. Chi, L. S. Yu-Jahnes, A. Gupta, T. Shaw, J. Z. Sun, and M. B. Ketchen, Phys. Rev. Lett. **73**, 593-596 (1994).

[25] M. Sigrist and T.M. Rice, Jour. of Phys. Soc. of Jap. **61**, 4283-4286 (1992).

[26] C. Renner, and Ø. Fischer, Phys. Rev. B **51**, 9208 (1995);

[27] Ch. Renner, B. Revaz1 J.-Y. Genoud, K. Kadowaki, and Ø. Fischer, Phys. Rev. Lett. **80**, 149 - 152 (1998).

[28] Pan, S. H., E. W. Hudson, and J. C. Davis, Appl. Phys. Lett. **73**, 2992 (1998).

[29] M. A. Ruderman and C. Kittel, Phys. Rev. **78**, 275 (1950); T. Kasuya, Phys. Rev. **16**, 45 (1956); K. Yosida, Phys. Rev. **106**, 896 (1957).

[30] S. Doniach, *Valence Instabilities and Narrow Band Phenomena*, (edited by R. Parks, 34, Plenum, 1977); S. Doniach, Physica B **91**, 231 (1977).

[31] Nicolas Doiron-Leyraud, Cyril Proust, David LeBoeuf, Julien Levallois, Jean-Baptiste Bonnemaison, Ruixing Liang, D. A. Bonn, W. N. Hardy and Louis Taillefer, Nature **447**, 565-568 (2007).

[32] T. Timusk and B. W. Statt, Rep. Prog. Phys. **62**, 61 (1999).

[33] W. W. Warren, Jr., R. E. Walstedt, G. F. Brennert, R. J. Cava, R. Tycko, R. F. Bell, and G. Dabbagh, Phys. Rev. Lett. **62**, 1193 (1989); M. Takigawa, A. P. Reyes, P. C. Hammel, J. D. Thompson, R. H. Heffner, Z. Fisk, and K. C. Ott, Phys. Rev. B **43**, 247 (1991).

[34] M. R. Norman, D. Pines, and C. Kallin, Adv. Phys. **54**, 715 (2005).

[35] V.J. Emery, and S.A. Kivelson, Nature (London) **374**, 434 (1995).

[36] M. Randeria, cond-mat/9710223v1 (1997).

[37] Xiao-Gang Wen and Patrick A. Lee, Phys. Rev. Lett. **76**, 503 - 506 (1996).

[38] S.C. Zhang, Science **275**, 1089 (1997).

[39] S. Chakravarty, R.B. Laughlin, D.K. Morr, and C. Nayak, Phys. Rev. B **63**, 0094503 (2001).

[40] C.M. Varma, Phys. Rev. Lett. **83**, 3538 (1999).

[41] M. Vojta, Y. Zhang, and S. Sachdev, Phys. Rev. B **62**, 6721 (2000).

[42] K. K. Gomes, A. N. Pasupathy, A. Pushp, S. Ono, Y. Ando, A. Yazdani, Nature **447**, 569 (2007).

[43] Y. Wang, L. Li, N. P. Ong, Phys. Rev. B **73**, 024510 (2006); Lu Li, J. G. Checkelsky, Seiki Komiya, Yoichi Ando, and N. P. Ong, Nature Phys. **3**, 311 (2007).

[44] A. Kanigel, U. Chatterjee, M. Randeria, M. R. Norman, S. Souma, M. Shi, Z. Z. Li, H. Raffy, and J. C. Campuzano, Phys. Rev. Lett. **99**, 157001 (2007).

[45] M. C. Boyer, W. D. Wise, Kamalesh Chatterjee, Ming Yi, Takeshi Kondo, T. Takeuchi, H. Ikuta, E. W. Hudson, Nature Physics **3 (11)**, 802-806 (2007).

[46] Y. Kohsaka, C. Taylor, K. Fujita, A. Schmidt, C. Lupien, T. Hanaguri, M. Azuma, M. Takano, H. Eisaki, H. Takagi, S. Uchida, J. C. Davis, Science **315**, 1380 (2007).

[47] J. Kondo, Prog. Theo. Phys. **32**, 37 (1964).

[48] C. J. Van den Berg, *Progress in Low Temperature Physics* **IV**, C. J. Gorter, editor, (North Holland, Amsterdam, p. 194, 1964).

[49] M. Sarachick, E. Corenzwit, and L. D. Longinotti, Phys. Rev. A **135**, 1041 (1964).

[50] A.C. Hewson, *The Kondo Problem to Heavy Fermions*, (Cambridge University Press, 1993). .

[51] Z. Fisk, H. R. Ott, T. M. Rice, and J. L. Smith, Nature **320**, 124 (1986).

[52] P. Coleman, cond-mat/0206003 (2002).

[53] Y. Onuki and T. Komatsubara, Journal of Magnetism and Magnetic Materials **63-64**, 281 (1987).

[54] P. H. P. Reinders, M. Springford et al, Phys. Rev. Lett. **57**, 1631 (1986). L. Taillefer and G. G. Lonzarich, Phys. Rev. Lett. **60**, 1570 (1988).

[55] V. Madhavan, W. Chen, T. Jamneala, M. F. Crommie, and N. S. Wingreen, Science **280**, 567 (1998).

[56] J. Li, W.-D. Schneider, R. Berndt, and B. Delley, Phys. Rev. Lett. **80**, 2893 (1998).

[57] D. Goldhaber-Gordon, D. H. Shtrikman, D. Mahalu, D. Abusch-Magder, U. Meirav, and M. A. Kastneret, Nature **391**, 156 (1998).

[58] J. G. Sereni, C. Geibel, M. G. -Berisso, P. Hellmann, O. Trovarelli and F. Steglich, Physica B **230-232**, 580-582 (1997).

[59] O. Trovarelli, C.Geibel, S. Mederle, C. Langhammer, F.M. Grosche, P. Gegenwart, M. Lang, G. Sparn and F. Steglich, Phys. Rev. Lett. **85**, 626 (2000).

[60] T. Hanaguri, Y. Kohsaka, M. Ono, M. Maltseva, P. Coleman, I. Yamada, M. Azuma, M. Takano, K. Ohishi, H. Takagi, Science **323**, 923-926 (2009).

[61] T. Hanaguri, Y. Kohsaka, J. C. Davis, C. Lupien, I. Yamada, M. Azuma, M. Takano, K. Ohishi, M. Ono, H. Takagi, Nature Physics **3**, 865-871 (2007).

[62] Strictly speaking, $g(\mathbf{q}, E)$ contains an additional q component associated with the set-point condition of the STM feedback loop, as well as the local-DOS modulation. In the following discussion, we analyze the conductance ratio in which this set-point effect is safely eliminated. Detailed discussion on the set-point effect is given in (46).

[63] Y. Kohsaka, C. Taylor, P. Wahl, A. Schmidt, Jhinhwan Lee, K. Fujita, J. W. Alldredge, K. McElroy, Jinho Lee, H. Eisaki, S. Uchida, D.-H. Lee, and J. C. Davis, Nature **454**, 1072 (2008).

[64] B.G. Levi, Phys. Today **60**, 17 V21 (2007).

[65] S. Huefner, M.A. Hossain, A. Damascelli, and G.A. Sawatzky, Rep. Prog. Phys. **71**, 062501 (2007).

[66] Ø. Fischer, M. Kugler, I. Maggio-Aprile, and Ch. Berthod, Rev. Mod. Phys. **79**, 353 (2007).

[67] M. C. M. M. van der Wielen, A. J. A. van Roij, and H. van Kempen, Phys. Rev. Lett. **76**, 1075-1078 (1996).

[68] C. Howald, P. Fournier, A. Kapitulnik, Phys. Rev. B **64**, 100504(R) (2001).

[69] J.E. Hoffman, Thesis, U. California, Berkeley (2003).

[70] J.E. Hoffman, K. McElroy, D.-H. Lee, K.M. Lang, H. Eisaki, S. Uchida, J.C. Davis, Science **297**, 1148-1151 (2002).

[71] K. McElroy, R.W. Simmonds, J.E. Hoffman, D.-H. Lee, J. Orenstein, H. Eisaki, S. Uchida, J.C. Davis, Nature **422**, 592 (2003).

[72] K. McElroy, D.-H. Lee, J. E. Hoffman, K. M. Lang, J. Lee, E. W. Hudson, H. Eisaki, S. Uchida, and J. C. Davis, Phys. Rev. Lett. **94**, 197005 (2005).

[73] Qiang-Hua Wang and Dung-Hai Lee, Phys. Rev. B **67**, 020511(R) (2003).

[74] R. Balian and N. R. Werthammer, Phys. Rev. **131**, 1553 (1963).

[75] A.V. Balatsky, I. Vekhter, J.-X. Zhu, Rev. Mod. Phys. **78**, 373 (2007).

[76] P.J. Hirschfeld, D. Vollhardt, and P. Woelfe, Solid State Commun. **59**, 111 (1986).

[77] M. Tinkham, *Introduction to Superconductivity*, (Second Edition, Dover Publications Inc., 2004).

[78] D. R. Tilley, J. Tilley, *Superfluidity and Superconductivity*, (IOP Publishing, Bristol, ed. 3, 1990).

[79] J. R. Schrieffer, *Theory of Superconductivity*, (Perseus Books, Reading, 1999).

[80] N. Bulut, D. J. Scalapino, Phys. Rev. B **45**, 2371 (1992).

[81] Y. Hasegawa, Ph. Avouris, Phys. Rev. Lett. **71**, 1071 (1993).

[82] M. F. Crommie, C. P. Lutz, D. M. Eigler, Nature **363**, 524 (1993).

[83] P. T. Sprunger, L. Petersen, E. W. Plummer, E. Lgsgaard, F. Besenbacher, Science **275**, 1764 (1997).

[84] C. C. Tsuei, J. R. Kirtley, Rev. Mod. Phys. **72**, 969 (2000).

[85] G. E. Volovik, JETP Lett. **58**, 469 (1993).

[86] T. Hanaguri, J. Phys. Conf. Ser. **51**, 514 (2006).

[87] T. Hanaguri, C. Lupien, Y. Kohsaka, D. -H. Lee, M. Azuma, M. Takano, H. Takagi, J. C. Davis, Nature **430**, 1001-1005 (2004).

[88] J. E. Hoffman, E. W. Hudson, K. M. Lang, V. Madhavan, H. Eisaki, S. Uchida, J. C. Davis, Science **295**, 466 (2002).

[89] K. Matsuba, Sh. Yoshizawa, Y. Mochizuki, T. Mochiku, K. Hirata1, and N. Nishida, J. Phys. Soc. Jpn. **76**, 063704 (2007).

[90] C. Kuebert, P.J. Hirschfeld, Solid State Commun. **105**, 459 (1998).

[91] J. Mesot, M. R. Norman, H. Ding, M. Randeria, J. C. Campuzano, A. Paramekanti, H. M. Fretwell, A. Kaminski, T. Takeuchi, T. Yokoya, T. Sato, T. Takahashi, T. Mochiku, and K. Kadowaki, Phys. Rev. Lett. **83**, 840-843 (1999).

[92] A. V. Chubukov, M. R. Norman, A. J. Millis, E. Abrahams, Phys. Rev. B **76**, 180501(R) (2007).

[93] K. A. Moler, D. J. Baar, J. S. Urbach, Ruixing Liang, W. N. Hardy, and A. Kapitulnik, Phys. Rev. Lett. **73**, 2744-2747 (1994).

[94] G.-q. Zheng, H. Ozaki, Y. Kitaoka, P. Kuhns, A. P. Reyes, and W. G. Moulton, Phys. Rev. Lett. **88**, 077003 (2002).

[95] K. Iwaya, S. Satow, T. Hanaguri, N. Shannon, Y. Yoshida, S. I. Ikeda, J. P. He, Y. Kaneko, Y. Tokura, T. Yamada, and H. Takagi, Phys. Rev. Lett. **99**, 057208 (2007).

[96] L. Capriotti, D.J. Scalapino, R.D. Sedgewick, Phys. Rev. B **68**, 014508 (2003).

[97] T. Pereg-Barnea and M. Franz, Phys. Rev. B **68**, 180506(R) (2003).

[98] T. Pereg-Barnea and M. Franz, Intnl. J. Mod. Phys. B **19**, 731 (2005).

[99] R. S. Markiewicz, Phys. Rev. B **69**, 214517 (2004).

[100] T.S. Nunner, Wei Chen, B.M. Andersen, A. Melikyan, and P.J. Hirschfeld, Phys. Rev. B **73**, 104511 (2006).

[101] T. Pereg-Barnea and M. Franz, Phys. Rev. B **78**, 020509(R) (2008).

[102] Kyung-Hee Kim, Heon-Jung Kim, Jung-Dae Kim, H.-G. Lee, and Sung-Ik Lee, Phys. Rev. B **72**, 224510 (2005).

[103] X. J. Zhou, T. Yoshida, A. Lanzara, P. V. Bogdanov, S. A. Kellar, K. M. Shen, W. L. Yang, F. Ronning, T. Sasagawa, T. Kakeshita, T. Noda, H. Eisaki, S. Uchida, C. T. Lin, F. Zhou, J. W. Xiong, W. X. Ti, Z. X. Zhao, A. Fujimori, Z. Hussain, and Z.-X. Shen, Nature **423**, 398 (2003).

[104] K.M. Shen, F. Ronning, D.H. Lu, F. Baumberger, N.J.C. Ingle, W.S. Lee, W. Meevasana, Y. Kohsaka, M. Azuma, M. Takano, H. Takagi, Z.-X. Shen, Science **307**, 901 (2005).

[105] K.M. Shen, Thesis, Stanford U. (2005).

[106] Magnetization, ARPES and STM measurements consistently suggest the value of the superconducting coherence length of about 10 times larger than the lattice constant $\xi \sim$ 10 a, far exceeding the coherence length in Bi2212 $\xi \sim 2$ a. In particular, magnetization studies of optimally doped $Ca_{2-x}Na_xCuO_2Cl_2$ (102) suggest the value of upper critical field $H_{c2} = 16.9$ T which corresponds to the value of superconducting coherence length ξ_0 =44 Å. From the average gap magnitude $\Delta_0 \sim 10$ meV observed in the STM spectra (60; 61) and the nodal velocity of $\hbar v_F = 1.8$ eV·Å (104; 103) one obtains $\xi \sim 57$ Å, while the diameter of the vortex cores seen in STM (60) is also of order 50 Å$\sim$ 10 a.

[107] L. Balents, M.P.A. Fisher and C. Nayak, Intnl. J. Mod. Phys. B **12**, 1033 (1998).

[108] P.W. Anderson, cond-mat/0406038 (2004).

[109] A. Kanigel, M. R. Norman, M. Randeria, U. Chatterjee, S. Suoma, A. Kaminski, H. M. Fretwell, S. Rosenkranz, M. Shi, T. Sato, T. Takahashi, Z. Z. Li, D. Hinks, H. Raffy, K. Kadowaki, and J.C. Campuzano, Nature **2**, 447 (2006).

[110] I.I. Mazin, D.J. Singh, M.D. Johannes, and M.H. Du, Phys. Rev. Lett. **101**, 057003 (2008).

[111] R.N. Hall, J.H. Racette, and H. Ehrenreich, Phys. Rev. Lett. **4**, 456 (1960).

[112] A.G. Wyatt, Phys. Rev. Lett. **13**, 401 (1964).

[113] D. Eigler, P. S. Weiss, E. K. Schweizer and N. D. Lang, Phys. Rev. Lett. **66**, 1189 - 1192 (1991).

[114] C. Howald, H. Eisaki, N. Kaneko, and A. Kapitulnik, Proc. Nat. Ac. Sci. **100**, 9705-9709 (2003).

[115] see e.g. J. L. Sarrao and Joe D. Thompson, Jour. of Phys. Soc. of Jap. **76**, 051013 (2007).

[116] P. Coleman, *Handbook of Magnetism and Advanced Magnetic Materials*, ed. H. Kronmuller and S. Parkin, (John Wiley and Sons, Vol 1, pp. 95-148, 2007).

[117] A. Schmidt, M. Hamidian, P. Wahl, F. Meier, G. Luke, and J.C. Davis, Bull. Am. Phys. Soc. **54**, abstr. BAPS:2009, MAR.V29.3 (2009).

[118] W. K. Park, J. L. Sarrao, J. D. Thompson and L. H. Greene, Phys. Rev. Lett **100**, 177001 (2008).

[119] Abhay Pasupathy and A. Yazdani, private communication (2009).

[120] A. F. G. Wyatt, Phys. Rev. Lett. **13**, 401 (1964); R. A. Logan and J. M. Rowell, Phys. Rev. Lett. **13**, 404 (1964).

[121] J. Appelbaum, Phys. Rev. Lett. **17**, 91 (1966).

[122] P. W. Anderson, Phys. Rev. Lett **17**, 95 (1966).

[123] D.V. Averin, and Yu.V. Nazarov, Phys. Rev. Lett. **65**, 2446 (1990).

[124] M. Pustlinik and L. I. Glazman, Phys. Rev. Lett. **87**, 216801 (2001).

[125] G. Mahan, *Many-particle physics*, (Plenum Press, New York, 1990).

[126] N. Read, D. M. Newns, and S. Doniach, Phys. Rev. B **30**, 384 (1984); P. Coleman, Ph. D. Thesis, Princeton University (1984).

[127] D. M. Newns and N. Read, Adv. in Physics **36**, 799 (1987).

[128] A. A. Abrikosov, Physics (Long Island City, NY) **2**, 5 (1965).

[129] V. Madhavan, W. Chen, T. Jamneala, M.F.Crommie, and N.S. Wingreen, Science **280**, 567 (1998).

[130] U. Fano, Phys. Rev. **124**, 1866 (1961).

[131] Zlatko Tesanovic, Phys. Rev. B **34**, 5212 (1986).

[132] Rebecca Flint, M. Dzero and P. Coleman, Nature Physics **4**, 643 (2008).

[133] A. J. Millis and P. A. Lee, Phys. Rev. B **35**, 3394 (1987).

[134] P.W. Anderson, Phys. Rev. **124**, 41 (1961).

[135] J. R. Schrieffer and P. A. Wolff, Phys. Rev. **149**, 491 (1966).

[136] M. Plihal, J. W. Gadzuk, Phys. Rev. B **63**, 085404 (2001).

Vita

Marianna I. Maltseva

2000-2003 Undergraduate Studies in Physics, B.S. Program, Moscow Institute of Physics and Technology, Russia.

2003-2009 Graduate Studies in Physics, Ph.D. Program, Rutgers University, NJ.

2005-2009 Graduate Research Assistanship, Rutgers University, NJ.

2003-2005 Graduate Teaching Assistanship, Rutgers University, NJ.

Publications

1. Marianna Maltseva, P. Coleman, "Failure of geometrical frustration to preserve a quasi-two-dimensional spin fluid", Phys. Rev. B **72**, 174415-9 (2005).

2. T. Hanaguri, Y. Kohsaka, M. Ono, M. Maltseva, P. Coleman, I. Yamada, M. Azuma, M. Takano, K. Ohishi, H. Takagi, "Coherence factors in a high-Tc cuprate probed by quasi-particle scattering off vortices", Science **323**, 923-926 (2009).

3. Marianna Maltseva, P. Coleman, "Model for nodal quasiparticle scattering in a disordered vortex lattice", arXiv: 0903.2752, accepted to Phys. Rev. B.

4. Marianna Maltseva, M. Dzero, P. Coleman, "Theory of tunneling into a Kondo lattice", in preparation.